CENTRO DE INVESTIGACIÓN Y DE ESTUDIOS AVANZADOS DEL INSTITUTO POLITÉCNICO NACIONAL

Unidad Mérida

DEPARTAMENTO DE FÍSICA APLICADA

"Celdas solares de perovskita híbrida de haluro de plomo: Procesos a baja temperatura y estudios de estabilidad"

TESIS

Que presenta

M. en C. Alejandra María Castro Chong

Para obtener el grado de

Doctora en Ciencias

en la especialidad de

Física Aplicada

Directores de Tesis:

Dr. Gerko Oskam

Dra. Mildred Quintana Ruiz

Mérida, Yucatán, México Julio, 2020

CENTRO DE INVESTIGACIÓN Y DE ESTUDIOS AVANZADOS DEL INSTITUTO POLITÉCNICO NACIONAL

Unidad Mérida

DEPARTMENT OF APPLIED PHYSICS

"Hybrid Lead Halide Perovskite Solar Cells: Low-Temperature Processes and Stability Studies"

THESIS

Presented by

M. Sc. Alejandra María Castro Chong

To obtain de degree of

Doctor of Science

in

Applied Physics

Thesis Directors:

Dr. Gerko Oskam

Dra. Mildred Quintana Ruiz

Mérida, Yucatán, México July, 2020

La tecnología es el producto de la actividad humana hacia el progreso de nuestra civilización, su origen yace en la curiosidad y toma forma de acuerdo con la motivación del hombre.

Technology is the product of human activity towards the advancement of our civilization, its origin lies in human curiosity and is shaped by his motivation.

Agradecimientos

Quiero agradecer a mis padres, Carlos y Amparo, quienes me han brindado apoyo incondicional no solo en este proyecto sino a lo largo de mi vida. Sin ustedes esto no habría sucedido. A mi hijo, Damián, quien ha sido compañero durante este trayecto a veces incluso desde la distancia. Cada pequeño paso lo di pensando en ti y hoy te dedico el fin de la meta. A mi hermana Karla, quien me ha brindó balance siempre que las cosas se tornaban complicadas.

A mi director de tesis, Dr. Gerko Oskam, quien me brindó siempre una visión más amplia para manejar todos los aspectos que discutimos. Soy muy afortunada de haberme encontrado con usted en mi búsqueda de un director de tesis. A mi directora de tesis, Dra. Mildred Quintana, quien amablemente me abrió las puertas de su laboratorio y me dio la oportunidad de aprender en él.

A CONACYT por las becas brindadas durante mis estudios de maestría y doctorado: 38748 y 311758, así como al Centro Mexicano de Innovación en Energía Solar (CeMIE-Sol) por el financiamiento del proyecto P18 y a la Agencia Mexicana de Cooperación Internacional para el Desarrollo (AMEXCID) por el financiamiento del proyecto SRE 2016-1- 278320.

A mis compañeros del laboratorio de Nanomateriales que me ayudaron a disfrutar y aprender. A los técnicos e ingenieros del CINVESTAV, Mérida porque siempre me brindaron su apoyo de la mejor manera.

A los doctores Isaac Zarazúa, David Meneses, Juan José Alvarado y Juan Anta por su dedicación a la revisión del trabajo presentado.

Resumen

Este trabajo consistió en la fabricación y caracterización de celdas solares de perovskita (CSP) mesoscópicas basadas en TiO_2 con el objeto de ampliar sus aplicaciones y mejorar su estabilidad. Se desarrolló un método de baja temperatura (BT), $T \leq 120$ ^oC, para fabricar CSP mesoscópicas basadas en TiO_2 mediante la incorporación nanopartículas de TiO_2 a partir de una dispersión en base a alcohol. Las CSP mesoscópicas de BT muestran alto desempeño, destacando una celda mesoscópica con eficiencia de conversión del 16.2 %. Reportes previos han indicado que el espesor óptimo de la capa mesoporosa (mp) es de alrededor de 150 nm, sin embardo en este trabajo se fabricaron celdas de alto rendimiento con capa mp de hasta 480 nm de espesor.

La influencia de la arquitectura y las propiedades electrónicas del material conductor de electrones (MCE) en la estabilidad de este tipo de dispositivos se hizo evidente. Las CSP mesoscópicas mostraron mayor estabilidad, con un tiempo de vida media (T_{50}) de casi el doble que el de las celdas planares. Se encontró que la eficiencia de extracción del MCE juega un rol importante en la preservación del desempeño a pesar de la descomposición parcial del material de perovskita.

Para obtener más información de los mecanismos de degradación de las CSP se llevó a cabo espectroscopía de impedancia. Dos mecanismos de recombinación dominantes cada uno a distintos valores de irradiancia fueron observados: recombinación tipo Shockley-Read-Hall para (< 10 mW cm^{-2}) y banda a banda para (> 10 mW cm^{-2}). La acumulación de carga se observó más acentuada en las celdas planares y, se relacionó con la migración iónica y degradación de los electrodos por especies iónicas reactivas en este tipo de celdas. Posteriormente, se propuso un modelo para la degradación retardada en CSP mesoscópicas

basado en las propiedades electrónicas de la capa nanoestructurada de TiO_2 y las diferencias del ambiente electrostático en la interfaz mp-TiO_2/perovskita.

Se desarrolló un proceso de optimización para la fabricación de CSP en atmósfera controlada. La fabricación de capas delgadas de perovskita se caracteriza por un proceso de nucleación que es muy sensible a las condiciones de la atmósfera, lo cual conlleva poco control de la cristalización. Se identificaron tres pasos de la fabricación como fuente de modificación de la composición de la atmósfera durante la formación de la perovskita: i) las condiciones de spin-coating, ii) el tratamiento térmico y iii) el tratamiento anti solvente. Se alcanzó un incremento en la eficiencia de conversión del 5% al 12%, demostrando que el proceso de optimización fue exitoso.

La incorporación de materiales nanoestructurados de carbono en las CSP es atractiva debido a las propiedades eléctricas de estos materiales. Se incorporaron fuleritas, una mezcla de grafeno y fulereno, en la capa activa de perovskita, con la finalidad de pasivar trampas en las fronteras de grano y prevenir el transporte iónico. A pesar de que en experimentos iniciales la eficiencia de conversión de las celdas solares no mejoró, debido principalmente a una aparente generación de derivaciones eléctricas, la estrategia ofrece oportunidades para mejorar el desempeño. Además, óxido de grafeno (GO) funcionalizado con guanidina fue depositado con éxito sobre la capa de perovskita en CSP mesoscópicas con la finalidad de mejorar la extracción de carga y prevenir el transporte iónico a través de la interfaz perovskita/Spiro. La inserción de una inter-capa de GO con buen recubrimiento fue lograda usando la técnica de pirólisis por pulverización de dispersiones en base a alcohol bajo condiciones ambientales. Los depósitos resultaron en capas con buena uniformidad sin causar degradación de la perovskita.

Abstract

This work consisted on the fabrication and characterization of TiO_2-based mesoscopic perovskite solar cells (PSCs) with the main goal to expand its applications and improve its stability. A low-temperature (LT) processing ($\leq 120\ ^oC$) method to fabricate high-efficiency mesoscopic TiO_2-based PSCs was developed by incorporating a spin-coated mesoporous (mp) TiO_2 film into a planar PSC architecture. Low-temperature mesoscopic PSCs show comparable performance, highlighted by a champion LT mesoscopic solar cell with 16.2% efficiency. Although earlier reports indicate that there is an optimal thickness of the mp layer of about 150 nm, this work shows that high-performance cells can be fabricated with an mp layer thickness up to 480 nm by carefully tuning the precursor solution chemistry.

The influence of the architecture and electronic properties of the electron transport layer (ETL) on the stability of this type of devices was evidenced. Mesoscopic PSCs were found to show better stability with a half-life time (T_{50}) value more than twice than that for planar devices. The extraction efficiency of the ETL was found to play an important role in the preservation of the performance, even after partial compositional degradation as evidenced by X-ray diffraction analysis.

To gain insight into the degradation mechanism of PSCs, impedance spectroscopy at the open-circuit potential was performed on partially degraded planar and mesoscopic PSCs. Two recombination mechanisms were observed to dominate depending on the irradiance value: the Shockley-Read-Hall recombination at illumination < 10 mW cm^{-2} and the band-to-band at illumination < 10 mW cm^{-2}. An electronic transport mechanism related to charge accumulation at the interfaces was found to dominate under high illumination intensities. The accumulation of charge was found larger in planar devices, and was related

to ionic migration and ion-induced degradation of the electrodes observed in planar PSCs. A model accounting for the slower degradation in mesoscopic PSCs is proposed based on the better electronic properties of the nanostructured TiO_2 scaffold and the different electrostatic environment at the mpTiO_2/perovskite interface.

An optimization process for the fabrication of PSCs under controlled atmosphere is presented. Solution processing of perovskite thin films is characterized by a nucleation process that is very sensitive to the precise atmosphere conditions, which leads to poor crystallization control. Three steps were identified as a source of changes in the atmosphere composition during perovskite formation: i) the spin coating conditions, ii) the annealing process and iii) the anti-solvent treatment. An increment in the average PCE from 5% to 12% was achieved, demonstrating the successful optimization of the fabrication process.

The incorporation of carbon nanostructures into PSCs is attractive for a variety of reasons, due to the electrical properties of this materials. Fullerites, consisting of a mixture of graphene and fullerene were incorporated in the perovskite active layer, in order to passivate grain boundary traps, and prevent ionic transport. Although the PCE of the solar cells in initial experiments did not improve, mainly due to apparent creation of shunts, the strategy still offers opportunities to improve performance. Further, graphene oxide (GO) functionalized with guanidine was successfully deposited on top of the perovskite layer on mesoscopic PSCs with as main goal to improve charge extraction efficiency, and to prevent ionic transport across the interface. The insertion of an interlayer of GO with good coverage was achieved through spray pyrolysis of alcohol-based dispersions under ambient conditions. The deposits resulted in good conformality films and did not cause any degradation of the perovskite material.

Contents

CHAPTER 1

Introduction

1.1 Energy from the Sun

The production, distribution and usage of energy is fundamental for human society. The escalation of energy requirement began with the industrial revolution in the 18th century. At present, our industrial civilization runs at a power requirement of around twenty terawatts (20 TW) of continuous power consumption, which is half of the power needed to drive the tectonic plates of about 40 TW (Morton, 2007). Since industrialization, fossil fuels have been the primary source for energy generation. Unfortunately, apart from being a finite resource, greenhouse gases are emitted into the atmosphere as a waste product of burning fossil fuels. Consequently, the earth is now absorbing more energy than it is emitting, which causes a rise in the average global temperature thus unbalancing the ecosystems. Hence, the need to find alternative methods for producing energy from clean, renewable sources is clear.

Astonishingly, the sun illuminates the earth at a continuous rate of 170,000 TW. Therefore, it is an attractive source for energy extraction. With a few exceptions, all forms of energy that we think of as renewable are solar. Wind power is solar, because the sun's heat transfer drives air currents. Hydroelectric power is solar, because it is the sun that drives the hydrological cycle. Biomass is solar, because it is generated by photosynthesis. Photovoltaics

(PV) is solar, and is the most straight forward approach, because it is harvesting solar radiation and directly converting it into electricity. Figure 1.1 shows the energy generation potential of the different renewable sources. Clearly, solar power has the potential to cover most of the global energy consumption. However, there are still several issues that must be addressed such as energy storage and time and location dependent insolation levels. Likewise, an important challenge is to find choices of solar cell technologies with high solar-to-electrical energy conversion efficiency and the versatility to power from a city to a mobile phone.

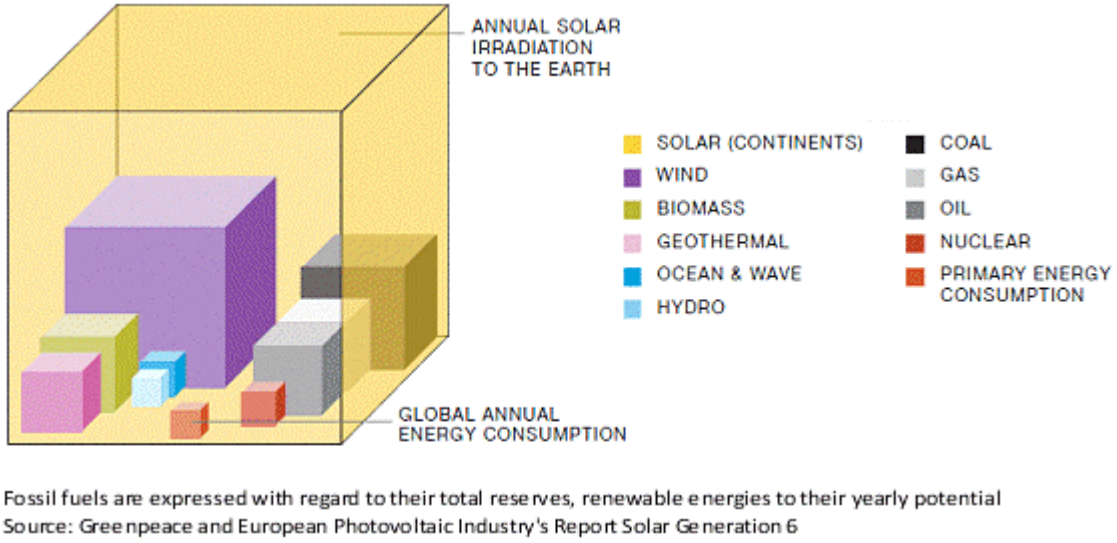

Figure 1.1. Energy generation potential of renewable sources; figure adapted from European Photovoltaic Industry Association Solar Generation (EPIA), 2011 (*European Photovoltaic Industry Association Solar Generation*, 2011).

1.2 Photovoltaic Technologies

The first device that converted sunlight into electrical power was fabricated in the 1950s at Bell laboratories in the U.S. For the following years until very recently, the PV

research focus has been on silicon technologies. Silicon is one of the most abundant elements of the earth's crust (Suess & Urey, 1956), and has demonstrated to be a robust material for solar energy conversion. Intensive research for more than four decades in the field of silicon-based solar cells has brought great advances in efficiency, material savings, passivation strategies and up-scaling. The record efficiencies for laboratory cell and average commercial module are 26.7% and 21%, respectively. According to the Fraunhofer Institute for Solar Energy Systems, silicon dominates the PV energy market with more than a 90% share (Philipps & Warmuth, 2019). Remarkably, due to the introduction of multi-crystalline silicon, a lower-purity silicon, the price of modules has decreased from around $1.30 to $0.30 per watt, from 2010 to 2018 (Liu et al., 2020). The low cost of production of multi-crystalline silicon has resulted in a highly competitive market making it difficult for other technologies to compete.

Silicon presents two major drawbacks: i) a large amount of material is required and ii) a high energetic production cost. Due to its indirect band gap silicon has a low absorption coefficient; thus, in order to absorb sufficient light, thick layers on the order of ~100 μm are required. In addition, due to high-energy purification processes, silicon solar cells hold the largest energy pay-back time of about 2 to 3 years (Philipps & Warmuth, 2019). A second-generation of solar cells, which are made of direct band gap semiconductors including cadmium telluride (CdTe) and copper indium gallium selenide (CIGS), gained strength in the late 1980s. Also known as thin film solar cells, this new generation of PV devices takes advantage of materials with good optoelectronic properties to utilize films with a thickness on the order of ~ 1 μm thus saving materials' costs.

Cadmium telluride-based solar cells represent the largest segment of commercial thin-film technology, currently representing around 5% of the world market (Philipps & Warmuth, 2019). The record efficiency for laboratory CdTe solar cells is 21 % and for its average commercial module the efficiency is 18% (Philipps & Warmuth, 2019). One of the biggest advantages of thin-film solar cells over silicon technology is the shorter energy pay-back time of around 1 year for PV systems installed in Germany, Figure 1.2. The reduced pay-back time relies on the inexpensive manufacture of thin film PV technologies.

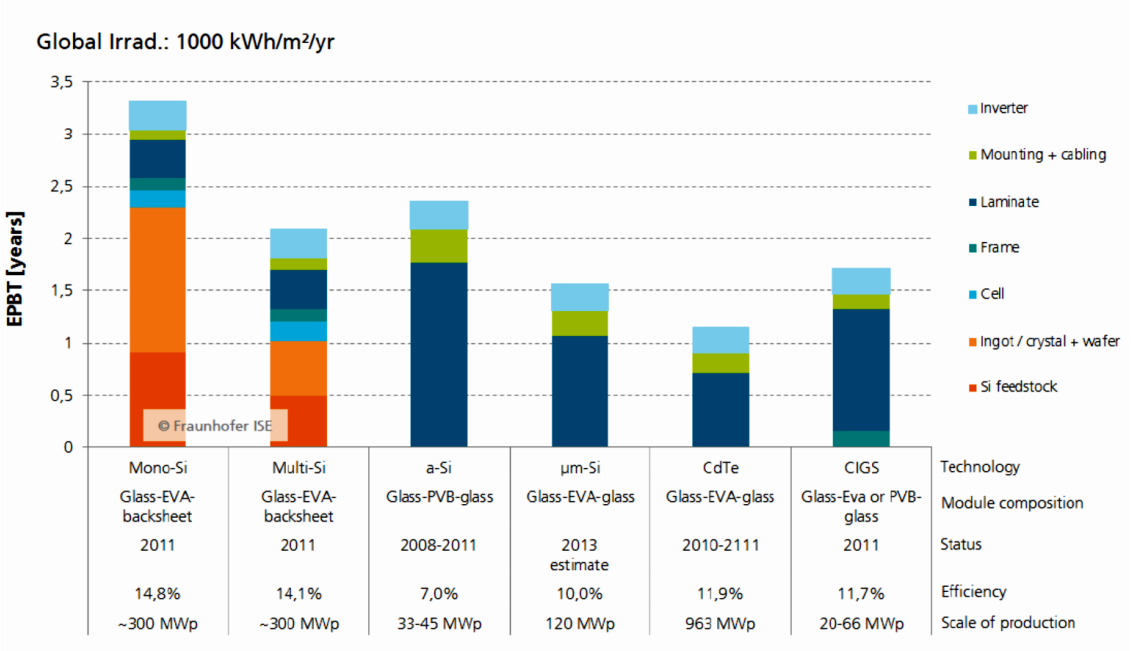

Figure 1.2. Energy Pay-Back time of rooftop PV systems located in Germany; figure adapted from ©Fraunhofer ISE: Photovoltaics Report (Philipps & Warmuth, 2019).

1.3 The Emergence of Perovskite Solar Cells

During the second half of the 20th century, a boom in technology-driven materials science was observed. In 1959 Richard P. Feynman gave a talk entitled “There’s Plenty of Room at the Bottom”, introducing the enormous potential of controlling things on a small

scale: nanotechnology. In the early 21st century, the scientific revolution achieved in synthesis and processing of semiconductor nanomaterials led into a third generation of solar cells. 'Third generation' solar cells include dye-sensitized, organic, perovskite, quantum dot, tandem, and new concept solar cells (Green, 2002). As foreseen by Feynman, novel complex phenomena are exploited in this type of solar cells, such as: multiple electron-hole pair generation, incorporation of an intermediate band, "hot" charge carriers, and quantum confinement (Almosni et al., 2018). These devices moreover can be processed from very abundant elements by a great variety of methodologies at relatively low energetic cost.

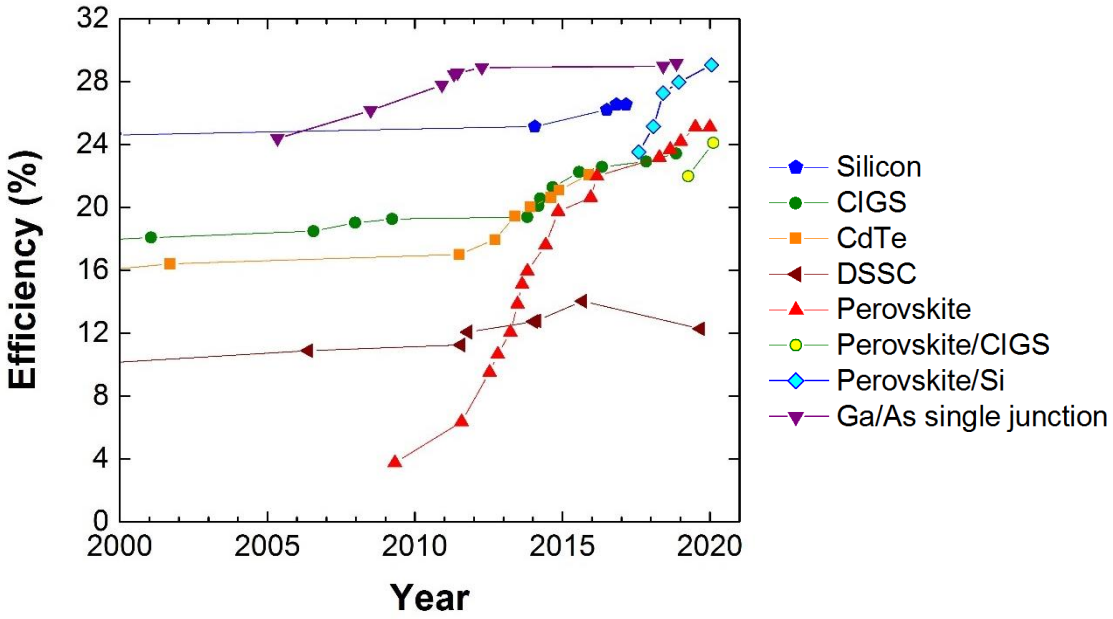

Figure 1.3. Solar cell efficiency progress showing, the accelerated improvement of perovskite containing solar cells is evident. Data taken from NREL efficiency chart, 2020 (NREL, 2020).

Hybrid perovskites are a class of solution-processed, low-cost semiconducting materials with excellent optoelectronic properties, i.e. strong absorption and high carrier diffusion lengths. Perovskite solar cells (PSCs) emerged from the dye-sensitized solar cells

(DSSCs). In 2009 the perovskite material, methylammonium lead iodide ($MAPbI_3$) was first used as the sensitizing material in a DSSC (Kojima, Teshima, Shirai, & Miyasaka, 2009), and rapidly surpassed the efficiencies of conventional solid state dye cells (J.-H. Im, Lee, Lee, Park, & Park, 2011). PSCs have shown astonishingly rapid progress in efficiency matching the performance of silicon technology in less than one decade, Figure 1.3. Efficiencies are now greater than 25% for PSCs and 29% for perovskite/Si tandem solar cells, making them competitive with single-junction GaAs solar cells, a III-V semiconductor third generation solar cell, with 29% of efficiency (NREL, 2020). This achievement is principally thanks to advancements in the chemical engineering of its components and to optimization of the fabrication processes. Furthermore, the implementation of perovskite materials in tandem solar cells such as the recently reported flexible perovskite/CIGS system, with an efficiency of 24.6%, has shown potential in applications due to the variety of substrates that can be used (Jošt et al., 2019).

The competitiveness of PSCs relies on its materials usage, energy usage, low cost and high-speed production methods. Nonetheless, to become commercially available important advances must be achieved regarding the lifetime of the devices. PSC performance is notably limited by deterioration that appears to be induced by mobile ions and vacancies of perovskite materials, in the presence of light and moisture.

Initially, PSCs acquired the structure of the DSSCs, with the perovskite material used as sensitizer. Later on, a thick film of the material was deposited on a mesoporous (mp) scaffold (*mesoscopic* PSC), which resulted in a boost of the solar cell efficiency (Ito et al., 2008). In 2012 it was demonstrated that the separation and transport of charges occur inside the perovskite absorbing layer without the need of an mp layer in the so-called

mesosuperstructured PSC (M. M. Lee, Teuscher, Miyasaka, Murakami, & Snaith, 2012). The latter resulted in the introduction of the *planar* architecture in which the mp layer is not included, Figure 1.4.

Interestingly, the mp-TiO_2 film does not seem to be essential, as both planar and mesoscopic architectures have reached similar efficiencies. However, reports show that the presence of the mp-TiO_2 layer often leads to considerable enhancement in reproducibility and stability, and suppresses the hysteretic effect in the device (H.-S. Kim et al., 2015; Leijtens, Lauber, Eperon, Stranks, & Snaith, 2014; Salim et al., 2015; Zhou et al., 2015). Accordingly, the inclusion of an mp layer is advantageous from the functioning point of view. Nonetheless, the energetic cost of the conventional fabrication methods for the mp-TiO_2 film is high: the standard procedure to fabricate a mp-TiO_2 layer includes a sintering step at about 500 °C. Thus, low-temperature (LT) fabrication methods are required.

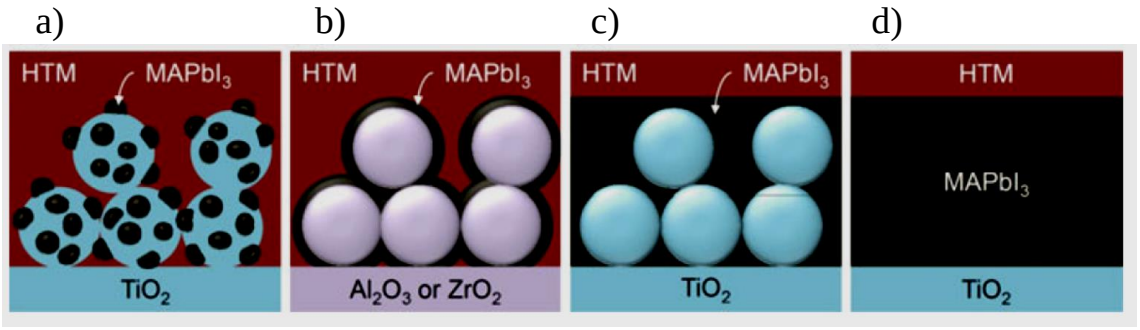

Figure 2.4. Evolution of perovskite solar cell configuration. a) sensitization concept, b) *mesosuperstructured* PSC, c) *mesoporous* PSC and d) *planar* heterojunction PSC; figure adapted from N.-G. Park *et al.* (Park, Grätzel, & Miyasaka, 2016).

1.4 Low Temperature Perovskite Solar Cells

Low-temperature (LT) fabrication processes of PSCs have lower energetic cost and are compatible with tandem and flexible solar cells, which find many applications. LT PSCs have been achieved mainly in the planar configuration by replacing TiO_2 with another electron transport layer (ETL) material, such as SnO_2, ZnO and PCBM (Azmi, Lee, Jung, & Jang, 2018; J.-Y. Chen, Chueh, Zhu, Chen, & Jen, 2017; Mahmud et al., 2017; Song, Zheng, Wang, Tian, & Miyasaka, 2016; You et al., 2014). Whilst the most efficient PSCs contain a mp-TiO_2 scaffold combined with a compact TiO_2 blocking layer, little effort has been spent on alternative low-temperature routes (< 150 °C).

From the experience in DSSCs it was assumed that an LT mesoscopic device would present an increased charge transport resistance, due to low interparticle connectivity at low-temperature sintering (Holliman et al., 2019). In 2014, high efficiency LT PSC devices were obtained with the addition of a binder to reduce the gaps between the nanoparticles (NPs) (Wojciechowski, Saliba, Leijtens, Abate, & Snaith, 2014); nonetheless, the effect of the remaining organic residues on the stability of the PSCs was not investigated. More recently, a UV curing treatment for the mp-TiO_2 scaffold was used to decompose the organic binders from the TiO_2 paste (Schulze et al., 2017), which resulted in PSCs with high performance.

In general, very similar photovoltaic parameters have been found for low and high temperature devices with a slightly lower photocurrent density for the LT case. However, research on the stability of LT processed mesoscopic TiO_2-based PSCs is limited.

1.5 Motivation and Objectives

The necessity to use renewable sources to cover our power consumption is increasingly evident. The solar power has the potential to cover most of the global energy consumption; thus, the advances in these technologies will have a positive impact on the planet and on our quality of life. The fabrication of stable, all-low-temperature solar cells would allow for a vast number of applications of the photovoltaic technology, which would contribute to the production of clean energy.

In this work, low temperature fabrication and device degradation mechanisms in PSCs have been studied. The structure of this thesis is the following:

In Chapter 4, a route to obtain LT *mesoscopic*-TiO_2 based PSCs is presented. The devices were prepared with three different values for the mesoporous TiO_2 (mp-TiO_2) layer thickness: 120, 300 and 480 nm, and their PV performance was compared to that of LT *planar* PSCs.

In Chapter 5, the evolution of the PV parameters of planar and mesoscopic LT PSCs upon exposure to light and moisture are discussed in detail. The electrical properties of the ETL have been correlated to the preservation of performance despite chemical decomposition of the perovskite material.

In Chapter 6, the degradation dynamics observed in Chapter 5 are studied further using impedance spectroscopy (IS). The characteristics of charge recombination and accumulation were found different in mesoscopic and planar PSCs. A model involving based on the IS analysis and the observations from the stability study is proposed to account for the retarded degradation dynamics in mesoscopic PSCs.

In Chapter 7 the main optimization processes for the fabrication of PSCs depending on the atmospheric conditions are presented along with a methodology to insert carbon-allotropes into the devices. The fabrication of high-efficiency devices under specific atmospheric conditions is demonstrated.

Finally, Chapter 8 presents the conclusions of this work.

CHAPTER 2

State of the Art of Perovskite Solar Cells

CHAPTER 2

State of the Art of Perovskite Solar Cells

2.1 Solar Cells

2.1.1 The Solar Spectrum

The energy flux from the sun has a distribution in energy approximately equal to the emission of a black body radiation at a temperature T_S of ~ 5800 K. Solar radiation is partially absorbed during its passage through the atmosphere: narrow spectral bands are filtered out by gases in the atmosphere, such as ozone, oxygen, water vapor (H_2O) and carbon dioxide (CO_2). The solar spectrum resulting from the absorption of a layer of air is called AM *X*, where *X* denotes the distance the light has traveled through the atmosphere in multiples of its thickness. A typical spectrum used for solar cell characterization is AM1.5G, which corresponds to and angle of incidence of solar radiation of 48° relative to the surface normal, Figure 2.1. The integral over this spectrum, the energy current density onto a surface normal to the sun, also known as irradiance, for a cloudless sky is $j_{E\ AM1.5}$ = 1.0 kW m^{-2}, while the average value in one year over the entire earth is 230 W m^{-2}, according to P. Würfel (Würfel, 2005).

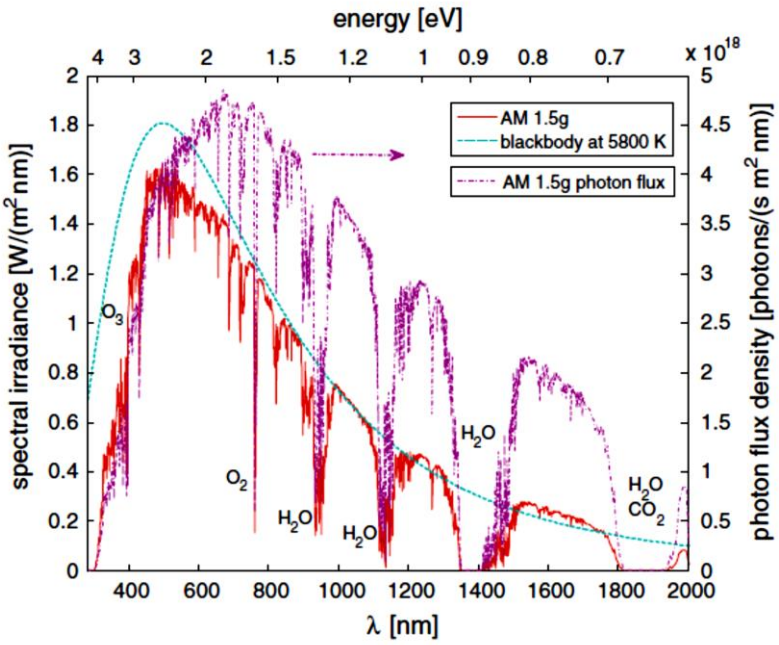

Figure 2.1. The AM1.5G spectral irradiance compared with a black body at a temperature of 5800 K. The photon flux density of the AM1.5G spectrum is shown; adapted from N. -G. Park *et al.* (Park et al., 2016).

2.1.2 Semiconductor-Based Photovoltaics

Solar photovoltaic energy conversion is a one-step process which generates electrical energy from light energy. In semiconductors, the energy band of valence electrons is separated from a band of empty states, the conduction band, by a forbidden zone without energy levels known as band gap. If a photon of energy $\hbar\omega$ larger than the band gap energy E_g is absorbed, a free electron is generated in the conduction band, while a free mobile hole remains in the valence band, thus generating a potential difference that drives current extraction to an external circuit.

The entire spectrum of sunlight, from infrared to ultraviolet, covers a range of energy $\hbar\omega$ between 0.5 eV and 5.0 eV. Nonetheless, photons with $\hbar\omega < E_g$ cannot excite electrons;

they are either transmitted or reflected by the semiconductor. To harvest as many solar photons as possible, the bandgap E_g of the semiconductor should be minimized, which allows for the highest electron-hole generation rate. The generated photocurrent is given by

$$J_{ph} = e \int_{E_g}^{\infty} \Phi_{AM1.5G}(E) dE, \tag{2.1}$$

where $\Phi_{AM1.5G}$ describes the sun's spectral photon flux.

However, a large photocurrent is not enough: the relevant parameter is the electrical power transferred to an external circuit. This electrical power is the product of the current and the potential energy of the extracted electron-hole pair, which is proportional to the voltage measurable externally. The potential energy of the electron-hole pair scales with the semiconductor band gap, even for absorbed photons with much higher energy, i.e. $\hbar\omega > E_g$. The photogenerated carriers with excess energy rapidly (10^{-12} s) tend to lose it through thermalization due to interaction with the lattice vibrations (Park et al., 2016), lowering their potential energy. Therefore, when tuning the bandgap to reach high electrical power, there is a compromise between harvesting as many photons as possible and maximizing the energy of the extracted charges.

To determine the optimum bandgap, it is needed to find an expression for the electrical energy of an extracted electron-hole pair. After long derivation (Würfel, 2005) it is found that the electrochemical potential $\eta_{e,h}$ of an electron (hole) in the conduction (valence) band, is:

$$\eta_e = E_C - k_B T \, ln \frac{N_C}{n}, \tag{2.2}$$

$$-\eta_h = E_V - k_B T \, ln \frac{N_V}{p}, \tag{2.3}$$

where n (p) is the electron (hole) density and N_C (N_V) is the effective density of states available.

In steady state, one electron is extracted together with one hole to conserve charge and obey the continuity equation. The total energy is then the sum of the electrochemical potentials,

$$eV = \eta_e + \eta_h = E_C - E_V - k_B T \ln\frac{N_C N_V}{np} = E_g - k_B T \ln\frac{N_C N_V}{np}. \quad (2.4)$$

Here, the externally measurable voltage V is introduced, which is expressed as the energy of one extractable electron-hole pair divided by the elementary charge e.

In addition, the electrochemical energy of the extracted electron hole-pair is not solely determined by the bandgap, but also contains a term that depends on electron and hole concentrations. The concentration of charges depends upon photon absorption (the so-called charge carrier generation G), it is determined by the condition $\hbar\omega > E_g$ and limited by recombination R. The rate of band-to-band recombination of an electron with a hole can be expressed as,

$$R = \beta np, \quad (2.5)$$

where β is the radiative recombination constant. In steady state at open circuit under a given light intensity all charges recombine and therefore the open-circuit voltage, which is the maximum electrical potential attainable in a solar cell under illumination, is:

$$eV_{OC} = E_g - k_B T \ln\frac{N_C N_V \beta}{np}. \quad (2.6)$$

The largest electrical power of a solar cell is at the maximum of the product between J and V, so-called maximum power point (MPP). Figure 2.2 shows the ideal power

conversion efficiency (PCE) as a function of the band gap calculated using equations 2.1 and 2.4 (Park et al., 2016). The maximum theoretical efficiency (Schockley-Queisser, SQ limit) for a single junction device, is obtained for semiconductors with E_g between 1.1 and 1.4 eV allowing a PCE ~ 33%. For small E_g values the low electrical potential of the electron-hole pairs limits the efficiency, while the decrease in efficiency for larger E_g is due to low photon harvesting, i.e., low J_{ph} according to Eq. 2.6.

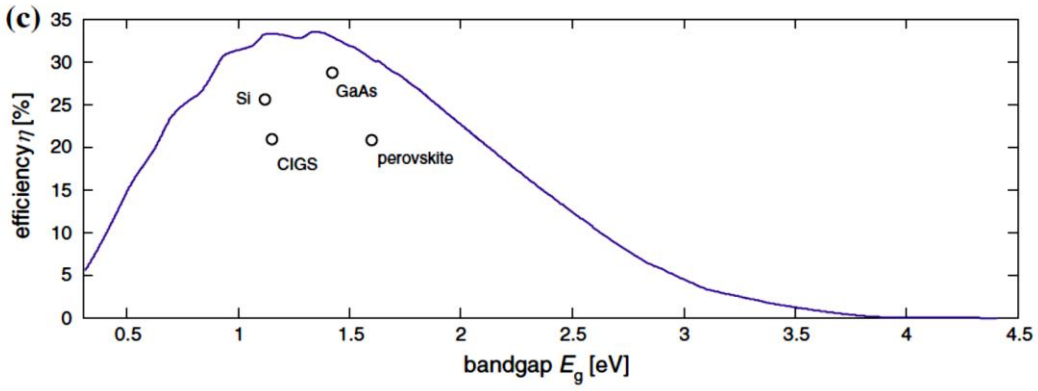

Figure 2.2. Maximum power conversion efficiency as a function of bandgap and record values experimentally achieved so far; adapted from N. -G. Park *et al.* (Park et al., 2016).

2.2 Working principles of Perovskite Solar Cells

The absorption onset of MAPI perovskite in comparison with other solar cell materials is shown in Fig. 2.3a (Park et al., 2016). Remarkably, MAPI has an optimum direct band gap E_g ~1.6 eV (Kojima et al., 2009; M. M. Lee et al., 2012; W. S. Yang et al., 2015). The estimated theoretical PCE (Shockley-Queisser limit) for a 500 nm-thick MAPbI-based single junction solar cell has been calculated to be around 30% with J_{SC} = 25 mA cm^{-2}, V_{OC} =1.32 V and 90.5% of fill factor (*FF*) (Park et al., 2016), Fig. 2.3b.

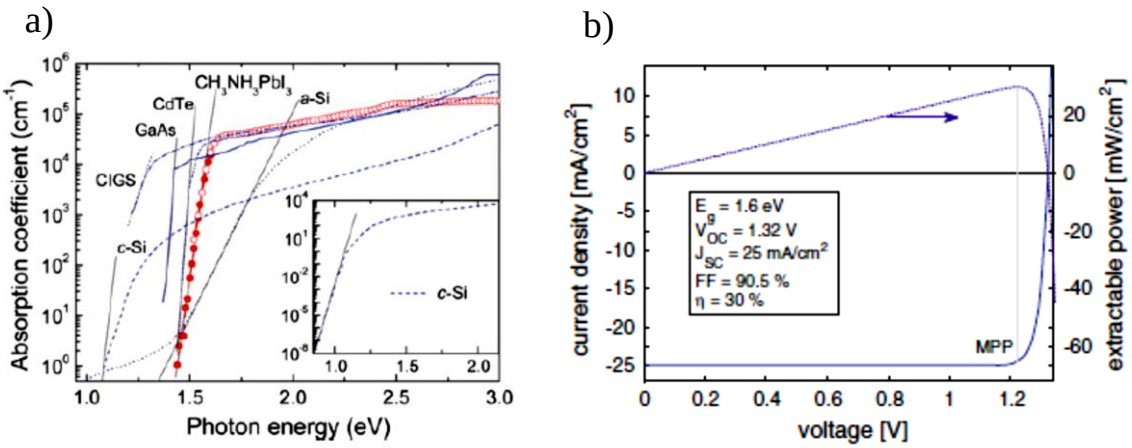

Figure 2.3. a) Absorption coefficient of different solar cell materials (De Wolf et al., 2014). b) Theoretical *J-V* curve and power output of an ideal semiconductor with E_g = 1.6 eV (Park et al., 2016).

Perovskite solar cells (PSCs) are basically structured as an absorber layer of perovskite material sandwiched between the electron and hole selective layers. The most successful and extensively studied configuration is a regular p-i-n heterojunction shown in where the TiO_2 layer is grown on top of the transparent conducting oxide (TCO)/glass substrate, as a mesoporous scaffold on top of a compact layer; then the methylammonium lead iodide $CH_3NH_3PbI_3$ (MAPI) perovskite and subsequently the spiro-OMeTAD (2,2'(7,7')–tetrakis-(N,N–di–p–methoxyphenyl-amine)9,9'-spirobifluorene). Metallic electrodes are often made of gold in order to achieve a good ohmic contact for charge extraction. The light crosses through the glass and the TCO, then through the electron transporting layer (ETL) to be absorbed by the perovskite, leaving the hole transporting layer (HTL) at the end of the light path.

In order to separate and collect the electrons from one side and holes from the other, it is necessary to create an asymmetry in the transport properties of the structure. A way to do this is to use the p-i-n heterojunction: under illumination these structures present a gradient in the electrochemical potential of electrons and holes that drive the drift of electrons and holes to the n and p region, respectively. Carriers are finally extracted trough a metallic contact at energies corresponding to the difference in the electrochemical potentials or quasi Fermi levels, Fig. 2.4.

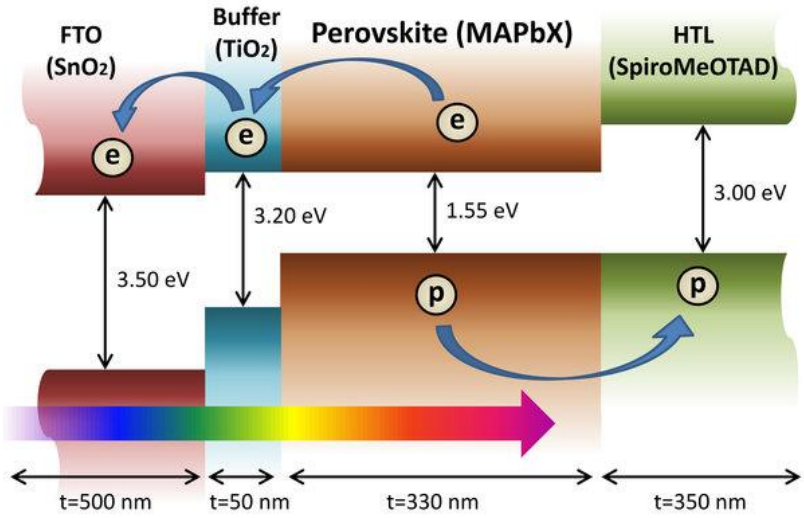

Figure 2.4. Energy band diagram for the regular p-i-n heterojunction used in PSCs. Drift of electrons and holes to the n and p regions is shown; adapted from Olyaeefar *et al.* (Olyaeefar, Ahmadi-Kandjani, & Asgari, 2017).

2.3 Crystal Structure of Perovskite Materials

Perovskite refers to the mineral form of $CaTiO_3$. Its crystal structure consists of corner-sharing TiO_6 octahedra in three dimensions, with Ca occupying the cuboctahedral cavity in each unit cell. The same crystal structure is also found for a wide range of materials with ABX_3 stoichiometry, Fig. 2.5. For halide perovskites, the oxidation states of the two cations must sum to three to achieve charge balancing ($q^A + q^B + 3q^X = 0$). In hybrid organic-inorganic lead halide perovskites such as MAPI, a divalent inorganic cation and a monovalent organic cation are present, i.e. lead (Pb^{2+}) and methylammonium (MA^+) respectively (Park et al., 2016).

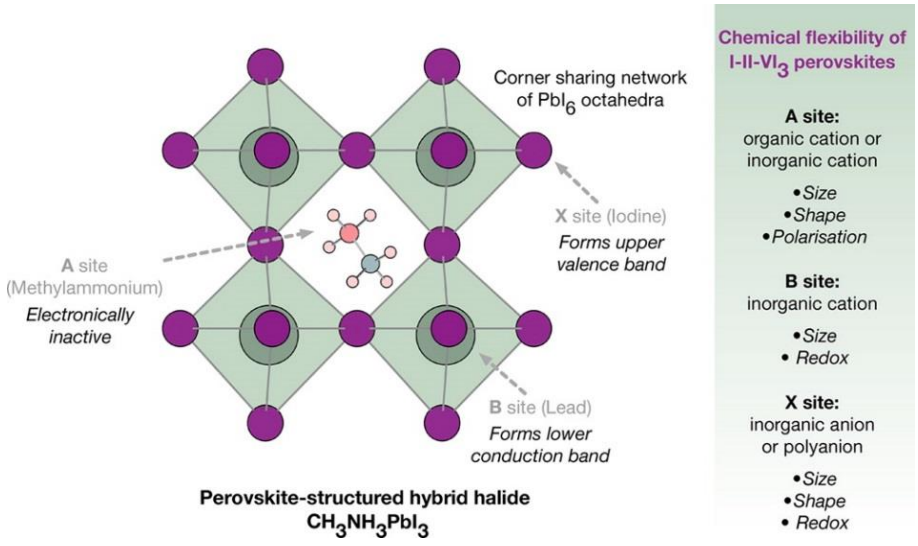

Figure 2.5 Schematic of the perovskite crystal structure with respect to the *A*, *B* and *X* lattice sites (Walsh, 2015).

The redox chemistry of the ABX_3 perovskite components can be used to influence the bandgap and the crystal structure of the material. The conduction band minimum of the perovskite material mainly originates from the metal cation (B), while the valence band

maximum mainly originates from the halide anion (X) (Yin, Yang, Kang, Yan, & Wei, 2015). As a result, substitution of the halide anion results in significant change in the optical bandgap. Reports show that incorporation of the smaller radius ion Br^- results in perovskites with larger bandgap compared to MAPI: the bandgap for $CH_3NH_3PbBr_3$ has been measured to be around 2.2 eV as compared to 1.5 eV corresponding to MAPI (Davies et al., 2014a; Jesper Jacobsson et al., 2016; Noh, Im, Heo, Mandal, & Seok, 2013). On the other hand, the cation (A) has an effect on the stability of the crystal structure. Higher stability of the lattice has been observed when substituting the generally used methylammonium (MA) with formamidinium (FA) and Cs cations (Arora et al., 2016; Saliba et al., 2016).

In the present work we used a mixed cation, mixed halide perovskite material with final estimated composition $FA_{0.71}MA_{0.29}PbI_{2.9}Br_{0.1}$, following the optimal composition for higher photovoltaic efficiency reported by Jacobsson *et al.* (Jesper Jacobsson et al., 2016). It is expected to be more stable than conventional MAPI because of its content of FA. The bandgap of this perovskite is between 1.55 and 1.59 eV (Jesper Jacobsson et al., 2016; Ramirez-Rincon et al., 2020).

2.4 Fabrication Method: The Intramolecular Exchange Process

Hybrid organic-inorganic lead halide perovskites popularity relies largely on its simple fabrication methods. Currently, there is a vast variety of deposition methods that includes wet chemical synthesis, vapor-assisted solution processes and vapor deposition techniques. However, spin coating the precursor solutions remains among the most used deposition techniques (Fedeli et al., 2015). The chemical conversion occurs due to the redox

chemistry of the ionic components in solution and the accelerated evaporation of the solvents due to the spinning and drying treatment.

Conversion to perovskite can be obtained in a one or two-step spin coating process, which implies a difference in the precursor solution chemistry, Fig 2.6. For one-step MAPI conversion, MAI and PbI_2 are mixed in a polar aprotic solvent such as *N*,*N*-dimethylformamide (DMF) or *N*,*N* dimethylacetamide (DMA) (J. H. Im, Kim, & Park, 2014). On the other hand, in the two-step spin coating process, a PbI_2 precursor solution in DMF is first spin coated to form a thin film, followed by immersion in (Burschka et al., 2013) or spin coating (sequential two-step deposition method) (J. W. Lee & Park, 2015) of, a 2-propanol (IPA) solution of MAI. In both processes, complete conversion is obtained by subsequent drying at a temperature at around 100 °C. Mixed perovskites like the one reported in this work have been obtained with the two-step sequential (STS) spin coating method described above (Castro-Chong et al., 2020; Davies et al., 2014b; Qiu et al., 2017). The STS deposition method has shown improved reproducibility and performance, due to better coverage and infiltration of the perovskite material into the scaffold (Jeon et al., 2014). The latter is suggested to arise from a suppressed formation of chemical species, i.e. iodoplumbates, that may give rise to recombination centers (Stewart, Grieco, Larsen, Doucette, & Asbury, 2016).

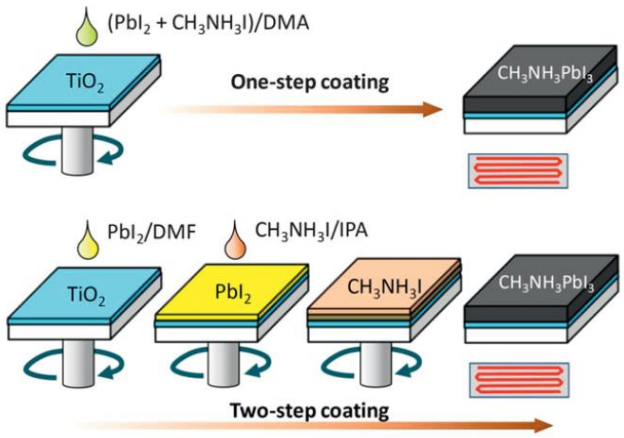

Figure 2.6. One-step and two-step coating procedures to deposit MAPI perovskite films; adapted from Im *et al.* (J. H. Im et al., 2014).

A breakthrough for the synthesis of hybrid halide perovskite materials was the introduction of dimethyl sulfoxide (DMSO) as a solvent in the PbI_2 solution (Jeon et al., 2014). Yang *et al.* developed the *intramolecular exchange process* (IEP) consisting on the formation of PbI_2-DMSO complexes in the precursor solution, in which DMSO can be easily replaced during conversion by external organic cations such as MAI or FAI because of their higher affinity toward PbI_2 (W. S. Yang et al., 2015). The chemical equation can be described as follows:

$$PbI_2 - DMSO + MAI(FAI) \rightarrow PbI_2 - MAI(FAI) + DMSO \uparrow \qquad (2.7)$$

To implement the IEP into the STS deposition method, an equimolar amount of DMSO relative to the amount of PbI_2 is added into the precursor solution containing PbI_2 and DMF. High-efficiency solar cells with a high degree of reproducibility have been demonstrated using this method (Castro-Chong et al., 2020; Qiu et al., 2017; W. S. Yang, Park, Jung, & Jeon, 2017).

2.5 Origins of instability in Perovskite Solar Cells

The lifetime of PSCs is a fundamental issue for this technology to be commercially viable. Moisture, oxygen, light and ionic migration are some of the degrading factors of the photoactive layer in PSCs. Furthermore, the synergy between decomposition of the perovskite film and reactivity of the other layers leads to alterations of the device and further deterioration of the photovoltaic parameters. Among the alterations observed are, decomposition of the perovskite material (Berhe et al., 2016; Niu, Guo, & Wang, 2015), reactivity and degradation at the electrodes (Carrillo et al., 2016; Kato et al., 2015), and related changes in the electrical properties, such as current-voltage (*J*-*V*) curve hysteresis variations.

A Moisture

The sensitivity of the hybrid lead halide perovskite material to water has its origin in the hygroscopic nature of the amine salt (R. Wang et al., 2019). The methylamine group evaporates once bound to a water molecule and PbI_2 forms; the hydrolysis reaction is represented by the following chemical equations:

$$CH_3NH_3PbI_3(s) + H_2O \leftrightarrow PbI_2(s) + CH_3NH_3I(aq) \quad (2.8)$$

$$CH_3NH_3I(aq) \leftrightarrow CH_3NH_2(aq) + HI(aq) \quad (2.9)$$

$$4HI(aq) + O_2(g) \leftrightarrow 2I_2(s) + 2H_2O(l) \quad (2.10)$$

$$2HI(aq) \leftrightarrow H_2(g) + I_2(s) \quad (2.11)$$

Encapsulation is a determining factor in the stability of the devices; however, the requirement to improve the intrinsic stability of the hybrid halide perovskite materials to water molecules is crucial. Lee *et al.* investigated the incorporation of cesium in the perovskite structure to strengthen the interaction between the cation and iodide (J.-W. Lee et al., 2015). Noh *et al.* explored the substitution of I ions with Br ions and found an enhanced moisture stability due to a change in the lattice constant (Noh et al., 2013). Smith *et al.* included a very stable two-dimensional (2D) layered perovskite in the photoactive layer forming a hydrophobic barrier (Smith, Hoke, Solis-Ibarra, McGehee, & Karunadasa, 2014). The former strategies have demonstrated high potential to reduce moisture induced decomposition processes and are currently very popular for their simple implementation at the lab scale. However, the scaling-up of the PSCs using these strategies still needs further investigation.

B Oxygen and Light

Oxygen can also influence the stability of the PSCs in the presence of light. Aristidou *et al.* showed that when PSCs are exposed to light, photoexcited electrons in the perovskite material react with molecular oxygen in air generating a harmful superoxide (O_2^-), Fig 2.7. The O_2^- species deprotonates the methylammonium cation yielding methylamine, PbI_2 and I_2 as products (Aristidou et al., 2015). The yield of superoxide production appears to be influenced by the electron transporting layer (ETL): efficient electron extraction from $CH_3NH_3PbI_3$ precludes the decomposition reaction.

This finding illustrates the importance of interfacial engineering in the PSCs. An interesting approach is the creation of strong interfacial dipole moments at the perovskite interfaces to improve the energy band level alignment and facilitate electron injection (W. H.

Lee et al., 2017; Lu et al., 2018). Other examples include the insertion of a chemical barrier to passivate the perovskite surface and prevent oxygen infiltration (M. Kim, Motti, Sorrentino, & Petrozza, 2018; N. Li et al., 2017). Evidently, the need for optimization of the device characteristics have spanned the interest in the field of PSCs, leading to highly specialized research.

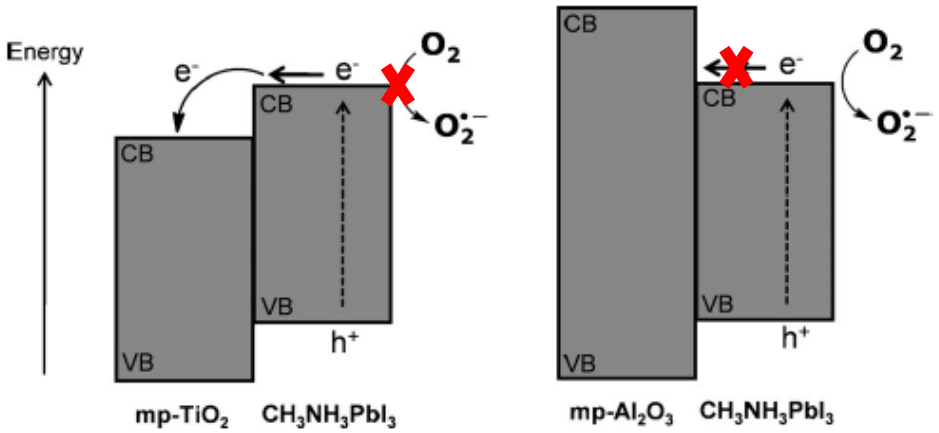

Figure 2.7. Schematic model for the electron transfer of photoexcited electrons in the MAPI layer to oxygen resulting in the formation of superoxide. Bryant *et al.* observed a higher yield of superoxide generation was observed in the system with an Al_2O_3 dielectric scaffold, demonstrating the importance of electron transfer in the stability of PSCs; figure adapted from Bryant *et al.* (Bryant et al., 2016).

C Ionic Migration

In hybrid organic-inorganic lead halide perovskite films, charged ions are have been observed to be mobile under applied or photogenerated electrical field, Fig 2.8. In addition to the redistribution of the built-in electrical field, migrating ions can reduce the device performance by forming charge traps and reaction sites at the interfaces causing degradation of the electrodes. The degradation is originated by chemical reactions between migrating species from either the perovskite material, the charge transport layers (CTLs) or counter

electrode. Oxidation of Ag to silver iodide (Kato et al., 2015), reduction of spiro-OMeTAD^{+} by I^{-} ions (Carrillo et al., 2016), soft acid - base reaction between Au and I^{-} (Shlenskaya, Belich, Grätzel, Goodilin, & Tarasov, 2018), and diffusion of 4-tert-butyl pyridine (tBP) related species into the perovskite layer (Bastos et al., 2018), have all been observed. Two major strategies to prevent detrimental reactions are: (i) enhance intrinsic stability of the perovskite material (El-Mellouhi et al., 2019), and (ii) implementation of a chemical insulating layer (Back et al., 2016). While important advancements have been made, the major challenge of these approaches is to obtain a material with the appropriate properties but not to create any drawbacks in the device operation.

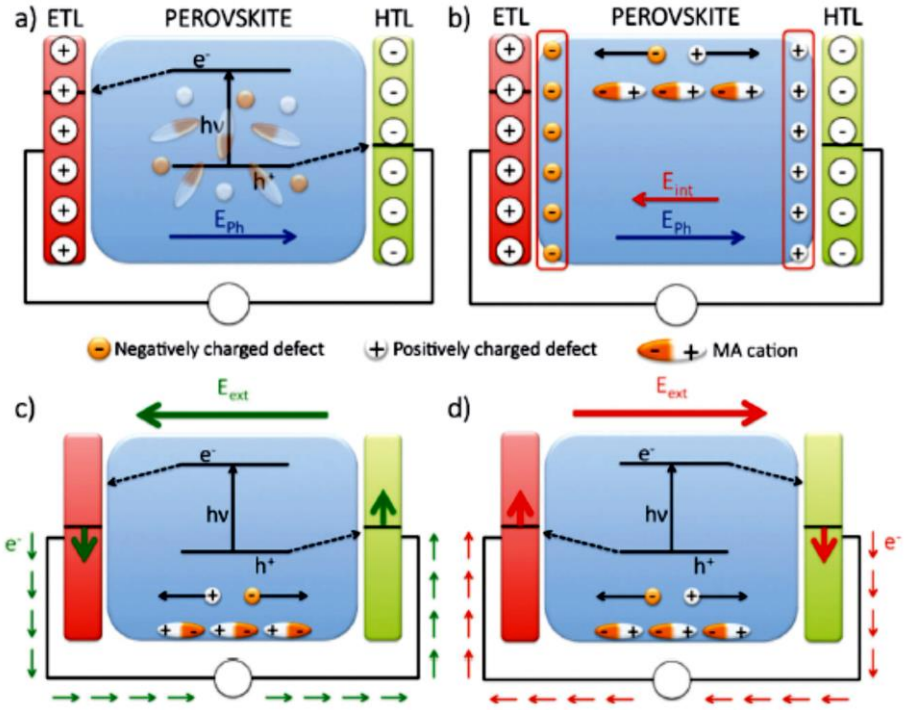

Figure 2.8. Sketch of ion migration and its impact on the PSC band energy alignment. a) shows the separation of the charge carriers driven by the photogenerated potential (E_{Ph}), along with the even distribution of the ions; b) depicts the migration of ions in response to E_{Ph}, and the internal potential developed as a consequence (E_{int}); (c) and (d) show the switchable current as a function of the applied external field (poling); figure adapted from Azpiroz *et al.* (Azpiroz, Mosconi, Bisquert, & De Angelis, 2015)**.**

A widely observed phenomenon related to ion migration in PSCs is the anomalous photocurrent hysteresis effect (Calado et al., 2016; B. Chen et al., 2015; Jacobs et al., 2017; W. Tress et al., 2015; Yu, Lu, Xie, Zhou, & Zhao, 2016). The rearrangement of ionic charges would change the depletion region at a rate that is dependent on the activation energy. The corresponding time scales measured vary from few seconds to hundreds of seconds, which affect the *J-V* sweeps at certain scan rates resulting in the observed hysteretic behavior, Fig 2.9. *J-V* hysteresis characteristics of PSCs have been related to ionic migration triggered degradation (Rizzo et al., 2019).

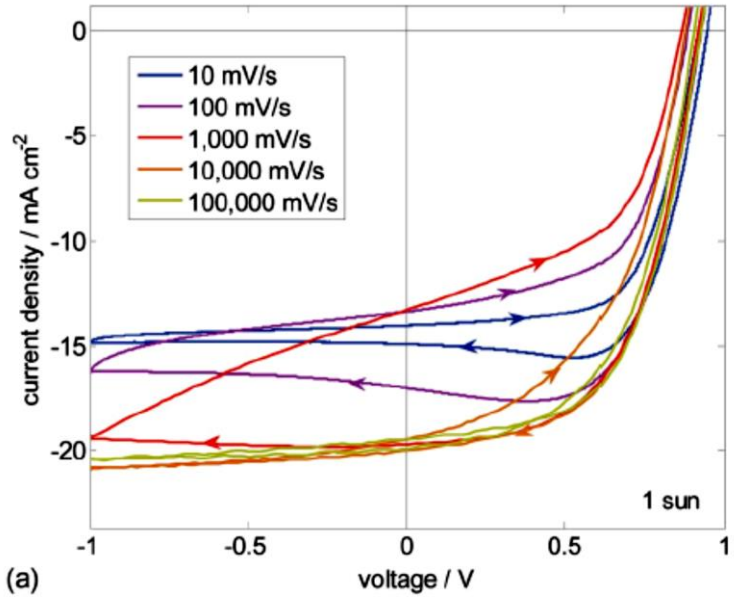

Figure 2.9. Current–voltage curves of TiO_2 based MAPI devices. Scans with different scan rates from 1 V to -1 V and back to 1 V. Sweep rates are from 10 to 100 000 mV s^{-1}, arrows denote the sweep direction; figure adapted from Tress *et al.* (W. Tress et al., 2015).

2.6 Impedance Spectroscopy of Perovskite Solar Cells

Impedance spectroscopy (IS) is a small perturbation frequency domain technique that consists in obtaining a linear output response of a system to an input stimulus. IS provides information about the electrical properties of the system, which may be ionic, semiconducting or even insulating. In photovoltaics, IS has been used to obtain information on the electrical characteristics of the devices such as the electrochemical potential distribution in the cell, recombination and collection time constants, series internal resistance, and charge accumulation (Carnie et al., 2013; Han et al., 2005; Sacco, 2017; van de Lagemaat, Park, & Frank, 2000). In the middle of the past decade, an equivalent circuit of a DSSC was proposed (Fabregat-Santiago, Bisquert, Garcia-Belmonte, Boschloo, & Hagfeldt, 2005; Q. Wang, Moser, & Grätzel, 2005), which allowed a very straightforward understanding of the electron transfer mechanisms in this type of devices, and extended the use of the technique to other technologies such as organic solar cells (Fabregat-Santiago, Garcia-Belmonte, Mora-Seró, & Bisquert, 2011; Perrier, De Bettignies, Berson, Lemaître, & Guillerez, 2012) and perovskite solar cells (Contreras-Bernal et al., 2019; Pockett et al., 2015; Zarazua, Han, et al., 2016).

Perovskite solar cells as a case study turned out to be rather noteworthy owing to their complicated electronic behavior. The IS characterization is not the exception and, though some of the mechanisms governing electron transfer are now understood, there remain open questions. However, in order to exploit the vast potential of IS a consensus about measuring conditions, the origin of the features composing the spectra and a general equivalent circuit is still needed.

In a typical impedance spectrum of a PSC two semicircles or arcs are the principal observed features, one at high frequencies >10 kHz and one at low frequencies <100 Hz (Contreras-Bernal et al., 2019; Klotz, Tumen-Ulzii, Qin, Matsushima, & Adachi, 2019; Pitarch-Tena, Ngo, Vallés-Pelarda, Pauporté, & Mora-Seró, 2018; Zarazua, Han, et al., 2016), Fig 2.10a. There is no consensus on the mechanisms underlying these two main features but there is a tendency towards a broad explanation. According to most of the researchers, the capacitive component of the high frequency response is dominated by the perovskite bulk, so-called geometrical capacitance (Pockett et al., 2015; Zarazua, Han, et al., 2016). The resistive high frequency component has been attributed either to transport (Guerrero, You, et al., 2016; C. Wang et al., 2017), or to recombination resistance (Pockett et al., 2015; Zarazua, Han, et al., 2016). The interpretation of the low frequency impedance response is certainly elusive, and its origin has been ascribed to several processes. These include: electron transfer through trap sites (Miyano, Tripathi, Yanagida, & Shirai, 2016), a giant dielectric effect (Juarez-Perez et al., 2014), charge accumulation at the electrode interfaces (Zarazua, Bisquert, & Garcia-Belmonte, 2016), and ion migration (Bag et al., 2015).

Additional features that have been observed in the low frequency range of the impedance spectra of PSCs are inductive loops, which can also be described by a negative capacitance. A negative capacitance indicates that the current output lags the alternating driving voltage. Zohar *et al.* observed negative capacitances in the IS measurement of perovskite films, and they suggest an electrochemical reaction in the material possibly involving vacancy and defect migration (Zohar et al., 2016), Fig 2.10b. Guerrero *et al.* observed an inductive feature in their spectra which is strongly dependent on the ETL

thickness, thus they suggested that this feature is associated to charge accumulation at the perovskite/contact interface (Guerrero, Garcia-Belmonte et al., 2016).

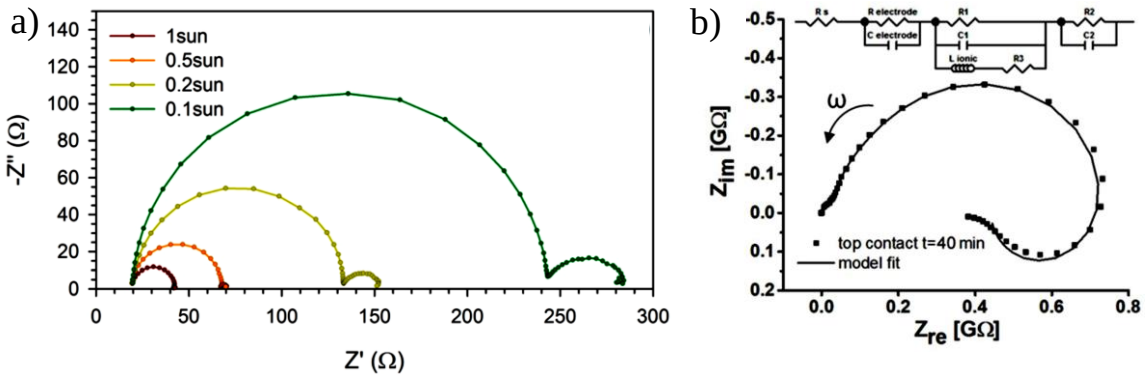

Figure 2.10. a) Nyquist plots for a MAPI-based PSC at different light intensities and open-circuit potential conditions, the frequency range is 1 MHz−0.1 Hz. Pitarch-Tena *et al.* (Pitarch-Tena et al., 2018) b) Nyquist plot for a MAPI film with Au top contact (deposited on glass), with residence of 40 minutes in an O_2-free environment, as proof of an electrochemical process in the perovskite film. Zohar *et al.* (Zohar et al., 2016).

Ghahremanirad *et al.* explained the presence of an inductive loop as a slow buildup of ionic charge at the perovskite interface; the kinetic relaxation constant would determine the rapidity of ion displacement (Ghahremanirad, Bou, Olyaee, & Bisquert, 2017). According to their model, the accumulated charge gives rise to an internal surface polarization voltage V_s which cannot follow the external bias voltage instantaneously but reacts at a velocity imposed by the ion displacement at the specified illumination. The contribution of the excess charge to the extracted current would give rise to the negative capacitance in the impedance spectra. Since IS measures the electrical response of the device as a whole, it is unfeasible to ascribe the observed inductive behavior to ion displacement. Nonetheless, owing to the time scale of these specific features it seems likely that the inductive behavior is by some means related to ionic charges in the perovskite material.

CHAPTER 3

Methodology

CHAPTER 3

Methodology

3.1 Fabrication Techniques

3.1.1 Spray Pyrolysis

Spray pyrolysis (SP) is a process in which a thin film is deposited by spraying a solution onto a heated surface. The precursor solution and temperature are selected such that the desired compound bonds to the substrate while the other products and solvent are evaporated (Bhagyaraj, Oluwafemi, Kalarikkal, & Thomas, n.d.).

Here, SP was used for the preparation of high-temperature (HT) TiO_2 blocking (BL) layers. The BL layers were deposited on the surface of the transparent conductive material, fluorine-doped tin oxide (FTO): a solution of 1 mL of titanium diisopropoxide bis(acetyl acetonate) (75% in 2-propanol, Sigma-Aldrich) in 24 mL of pure 2-propanol was used as precursor. Twenty 2 x 2 cm^2 FTO-coated glass substrates were kept at 350 °C on a hot plate and sprayed with 25 mL of precursor solution. The deposition was performed manually, with the distance between the spray nozzle and the substrate set to 40 cm making an angle of 60° with the surface of the substrate. The air manometric pressure was set to 0.2 MPa. The velocity with which the spray gun was displaced manually to scan the substrate area was approximately 1 cm s^{-1}. A cycle consisted on scanning the entire substrate area longitudinally

back and forth once and waiting a lapse of 40 s before starting again. The number of cycles was repeated until the volume of 25 mL was exhausted. A BL TiO_2 layer of 60 nm was obtained. After deposition, the substrates were kept at 350 °C for 15 minutes.

3.1.2 Atomic Layer Deposition

Atomic layer deposition (ALD) is a vapor phase technique capable of depositing conformal thin films of materials of varying compositions on diverse substrates. ALD film growth is based on sequential, self-saturating surface reactions.

In the present work, low-temperature (LT) TiO_2 BL layers were fabricated using the ALD method. The ALD process was performed with a Savannah equipment from Cambridge NanoTech. Tetrakis(dimethylamino)titanium (TDMAT) and H_2O were used as precursors for the surface chemical reaction leading to the formation of a TiO_2 film. The deposition process was performed using a recipe provided by the equipment provider: "G2 Savannah TiO_2 Thermal, TDMAT & H_2O". The H_2O and TDMAT pulse durations were 0.015 and 0.1 s, respectively; with evacuation time of 10 s each. The temperature of TDMAT and the reactor chamber were 75 °C and 100 °C, respectively. The observed growth rate was about 0.7 Å/cycle.

3.1.3 Thermal Evaporation Techniques

Thermal evaporation processes comprise evaporating source materials in a vacuum chamber below 2×10^{-6} mbar and condensing the evaporated atoms on a substrate. The heating can be resistive, or electron beam (e-beam) assisted. Resistive heating is the most commonly used method, while electron beam heating is mainly used to evaporate refractory metals. The deposition rate depends on the evaporation rate, source geometry and position relative to the substrate (Adachi & Wasa, 2012). These techniques are especially interesting

for LT processes since the substrates are prevented from warming up by recirculating water from a chiller.

A E-Beam Evaporation

E-beam evaporation was used for the deposition of TiO_x compact layers in the fabrication of all LT devices. Titanium pellets were evaporated at a rate of 1 Å/s onto indium-tin oxide (ITO) substrates, using a partial O_2 pressure of 1.7×10^{-4} Torr, until a compact TiO_x layer of 20 nm was obtained. The deposition was performed with an Angstrom Engineering evaporation system with initial pressure smaller than 2×10^{-6} mbar.

B Resistive Heating Evaporation

Resistive heating was used for the evaporation of a 60-90 nm-thick gold layer. A delimitation mask was used to obtain both electrode and counter electrode Au films. The deposition process was performed with a Tecuum-VCM 600, desktop vacuum evaporator. A current of 90 A was applied to a tungsten boat, and the initial pressure was 2×10^{-6} mbar; the growth rate was ~ 0.8 Å/s.

3.1.4 Sol-Gel Synthesis Method

The sol-gel method is a chemical synthesis approach to prepare metal oxide nanoparticles (NPs) and mixed oxide composites. The formation of the metal oxide involves different consecutive steps, (i) hydrolysis to produce a metal hydroxide, (ii) condensation and formation of the gel, and (iii) drying processes.

In this work the sol-gel method was used to obtain TiO_2 NPs, in the anatase phase, with variations from the standard procedure (Ito et al., 2008): 0.07 mol titanium iso-propoxide was dropwise added to 0.07 mol acetic acid with stirring at room temperature. The

mixture was kept under agitation for 15 min and was then dropwise added to 145 mL water. After adding 1.4 mL concentrated nitric acid (65.4%), the mixture was heated to 80 °C in 40 min, and then peptized for 75 min. After aging for one week with agitation, aliquots from the resultant mixture were hydrothermally treated at 200 °C for 30 h in a Teflon-lined titanium autoclave (Parr Instruments). The nanoparticulate slurry obtained was centrifuged and washed with ethanol three to four times to eliminate remnant water. The washed TiO_2 nanoparticles were dispersed either in butanol or ethanol. Spin coating inks were prepared by dispersing the TiO_2 nanoparticles at 1.2 wt.%.

3.1.5 Spin Coating

Spin coating is a deposition technique used to deposit uniform coating of materials on a flat substrate. The substrate is placed on a turntable, the solution is dispensed on the substrate surface, and the turntable is spun at a high speed; the applied solution is distributed via centrifugal force. The deposit is either ‘static’ or ‘dynamic’ depending on the moment at which the solution is dispensed, i.e. before or during turntable spinning. The thickness of the deposited layer is controlled by the viscosity of the coating solution and the speed of rotation.

In the present work, spin coating was used for the deposition of three different materials: the mesoporous (mp) TiO_2 layer, the hybrid organic-inorganic lead halide perovskite film and the spiro-OMeTAD. The conditions of the spin coating process and the obtained thickness with one deposit for each material are summarized in Table 3.1 in the next section.

3.1.6 Perovskite Solar Cell Fabrication

Glass substrates with either ITO or FTO electrodes were cleaned in an ultrasonic bath, using detergent, deionized water, acetone, and iso-propanol. In the case of the FTO covered glasses, the substrates were heated to 450 °C for 30 min to activate the surface. For the preparation of the compact (c) and mesoporous (mp) layers, two different routes were followed depending on the desired process temperature. The LT process consisted in depositing a TiO_x BL using either e-beam evaporation or ALD (Sections 3.1.2 and 3.1.3A), followed by spin coating of the dispersion of TiO_2 NPs to obtain the mesoporous layer, (Section 3.1.5). The spin coating deposition of the dispersion was repeated several times to achieve the desired thickness, and immediately afterwards the film was annealed for 60 min at 120 °C. In the HT process a TiO_2 BL was achieved using the spray pyrolysis method at 350 °C. Afterwards, the mp-TiO_2 layer was prepared using either the dispersion of TiO_2 NPs or a dilution of a commercial TiO_2 paste (Greatcell Solar, 18NR-T, 150 mg mL^{-1}). The HT samples were annealed at 500 °C for 60 min.

Deposition of the perovskite film was achieved by spin coating using the intramolecular exchange process adapted to the two-step spin coating sequential method, as described in Section 2.2 in Chapter 2. Standard solutions designed for the fabrication of planar PSCs were used (Qiu et al., 2017), and were further optimized for mesoscopic cells. Two standard solutions were first prepared:

- Solution A consisted of 1.25 M PbI_2 in a mixture of N, N-dimethyl formamide and dimethyl sulfoxide (DMF/DMSO: 90/10, v/v).
- Solution B consisted of $CH(NH_2)_2I$ (FAI), CH_3NH_3I (MAI) and CH_3NH_3Br (MABr) (71:19:10 molar ratio) in isopropanol.

The precursor solution chemistry was optimized for each mp-film thickness (Section 5.3.2, Chapter 5). Precursor solution A was stirred at 75 °C for 10 min and left to cool while solution B was stirred for 10 min at room temperature. A sufficient amount of solution A to cover the substrate (80-120 µL) was first spin-coated at 3000 rpm for 30 s onto the substrate and, immediately afterwards, 70 µL of solution B was deposited at 3000 rpm for 30 s. The obtained films were annealed on a hot plate at 100 °C for 30 min to form the crystalline perovskite. After cooling to room temperature, 80 µL of an 80 mg/mL spiro-OMeTAD solution with 17.5 µL lithium bis(trifluoromethanesulfonyl)imide (520 mg/mL in acetonitrile) and 28.5 µL 4-tert-butylpyridine was spin-coated onto the perovskite films. All spin-coating processes were performed in an N_2-filled glove box (H_2O < 10 ppm, O_2 < 100 ppm). After coating with spiro-OMeTAD, the samples were exposed to air overnight (t > 17 h, 30% R.H.) for oxygen doping of the hole transporting layer. The small area devices were completed by thermal evaporation of a 60-90 nm Au layer through a shadow mask. The composition and thickness of each layer in the solar cell device is shown in Figure 3.1, and Table 3.1 summarizes the spin coating conditions and the thickness obtained with one deposit for each material; the volume given was used for a surface area of 4 cm^2.

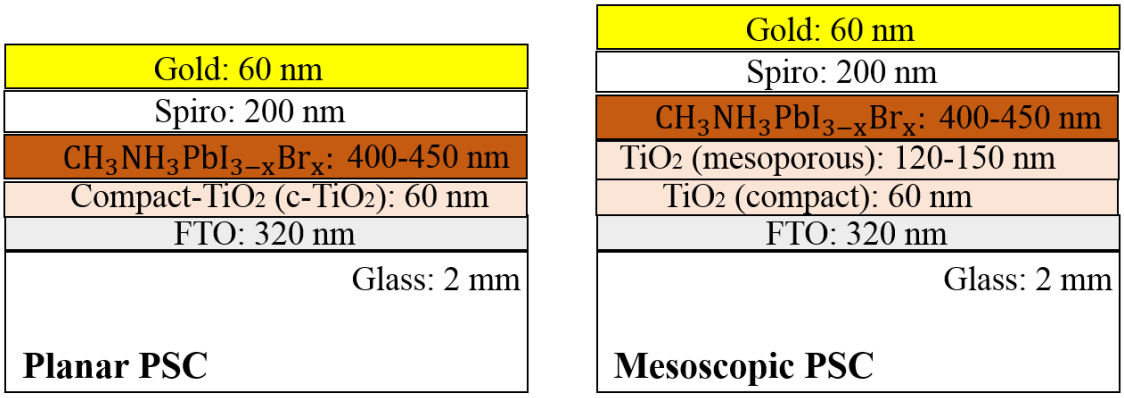

Fig 3.1 Device composition and layer thickness for planar and mesoscopic perovskite solar cells.

Table 3.1 Spin-coating conditions and thickness obtained for the different materials in PSCs.

Material	**Type of process**	**Volume of the ink [µL]**	**Velocity [rpm]**	**Thickness [nm]**
TiO_2 mp layer	static	60	4500	~60
Perovskite solution A	static	80-120	3000 or 1900*	~400
Perovskite solution B	dynamic	55	3000 or 2000*	~480
spiro-OMeTAD	dynamic	60	2000	~200

*The optimization of the fabrication process for the Nanomaterials lab at Cinvestav resulted in lower spin coating speeds than the original recipe reported by Qiu *et al.* (Qiu et al., 2017), see Chapter 4.

3.2 Characterization Techniques

3.2.1 Scanning Electron Microscopy

Scanning electron microscopy (SEM) is a surface imaging method in which the incident beam scans across the sample surface and interacts with the sample to generate backscattered and secondary electrons that are used to create an image of the sample. Secondary electron image (SEI) are generated when the electron beam strikes the sample and ionizes the atoms of the sample. The interaction depth is very shallow thus, SEI provides images of the sample surface morphology. Low-angle backscattered electrons (LABE) are electrons from the SEM beam that strike the atoms of the sample and are ejected back out of the surface of the sample. LABE detector is more sensitive to compositional, representing heavier elements with brighter images (Ul-Hamid, 2018).

In the present work, SEI and LABE micrographs were obtained to study NPs size and shape, coverage and thickness of thin films, uniformity of the deposits, and grain size and morphology of the fabricated materials. The images were obtained with a JEOL JSM-7600F scanning electron microscope.

3.2.2 X-Ray Diffraction

X-ray diffraction (XRD) is a characterization technique that provides detailed information on the crystallographic structure and phase segregation in the materials. Information on the crystal planes derives from the elastic scattering of x-ray photons by atoms in the periodic lattice; the spacings are obtained using Bragg's law. In order to identify the structure and composition, the diffraction pattern is recorded and compared with standard line patterns available in a database (Waseda et al., 2011).

XRD was used to identify crystallographic phases and composition of the materials. The diffractogram of the obtained TiO_2 NPs was recorded to identify the crystalline phase obtained in the synthesis. Diffractograms of the hybrid perovskite were recorded to investigate the presence of specific compounds, which indicate incomplete chemical conversion or degradation of the material. X-ray diffraction patterns were recorded with a Siemens D-5000 diffractometer using Cu-Kα radiation.

3.2.3 External Quantum Efficiency

The incident photon-to-electron conversion efficiency (*IPCE*), also called *external quantum efficiency* (*EQE*) of the solar cell, describes how many of the incoming photons at a certain wavelength, λ, are converted to electrons:

$$EQE\ (\lambda) = \frac{electrons\ out\ (\lambda)}{incident\ photons\ (\lambda)} = \frac{J_{SC}}{q\Phi(\lambda)} = \frac{hc}{q} \cdot \frac{J_{SC}(\lambda)}{\lambda P_s(\lambda)}, \tag{3.1}$$

where q is the elementary charge, Φ the photon flux, $P_s(\lambda)$ *is* the spectral irradiance, and h and c Planck's constant and the speed of light, respectively.

EQE spectra were measured with a photo spectrometer set-up (Bentham PVE300) by illuminating the solar cell with modulated monochromatic light (Xe and quartz halogen lamps) at a chopper frequency of 377 Hz, spectral resolution of 5 nm and without light bias.

3.2.4 UV-Vis Absorbance Spectroscopy

The optical absorbance of a material depends on the electronic transitions between orbitals or bands of atoms, ions or molecules in the material, and is given by,

$$\alpha(\lambda) = 1 - R(\lambda) - T(\lambda), \tag{3.2}$$

where $R(\lambda)$ and $T(\lambda)$ are the reflectance and transmittance of the material. A standard spectroscope measures direct transmittance as a percentage (%T); this represents the percentage of the incident beam of light transmitted by the sample. There are two kind of reflectance, specular and diffuse. Specular reflectance refers to the part of the incident beam reflected at the same angle as the angle of incidence. Diffuse reflectance refers to the part of the incident beam reflected in all directions (Perkowitz, 1993).

In this work, $T(\lambda)$ and $R(\lambda)$ have been measured using a spectrometer (AVANTES, model AVASpec 2048) and a deuterium-halogen lamp as the light source (AVANTES, AvaLight-DH-S-BAL), coupled through optical fibers (AVANTES, FC-UV600-2). The configuration for optical reflectance measurements includes an integrating sphere (Ocean Optics model ISP-50-8-R-GT; spectral range: 200–2500 nm), which has an optical trap that allows us to perform total and diffuse reflectance spectroscopy separately. The optical fibers are attached to the integration sphere to illuminate and collect the reflected light by the sample (placed at the bottom side), while in the transmittance configuration the optical fibers are faced, with the sample placed between them.

3.2.5 Photoluminescence Spectroscopy

Photoluminescence (PL) is the spontaneous emission of light from a material under optical excitation. Photoexcitation of a semiconductor material promotes an electron from the valence band to the conduction band, leaving a ‘hole’ in the valence band. The excited electron in the conduction band relaxes through scattering processes and then recombines with the hole; if the recombination process is radiative, a photon is emitted. PL spectroscopy has shown to be a useful technique to identify electronic transitions that produce radiative recombination, providing information about the energy levels in the system. PL spectroscopy

of semiconductors quantifies the radiative recombination providing information about the bandgap energy and electron-hole recombination mechanisms (Perkowitz, 1993). PL spectra were recorded using an iHR Horiba spectrometer, and a mounted-in OBIS LX/LS laser with wavelength at 660 nm.

3.2.6 Current-Voltage Characterization

Current-voltage (*J-V*) characterization is used to test the performance of a solar cell. In order to test the response of the device to solar light, it is usually illuminated with an irradiance of 1 sun (100 mW cm^{-2}, *AM* 1.5G) during the measurement. The source of light is commonly a xenon arc lamp, and the light passes through several filters that modify the intensity and spectrum to better match the solar spectrum. The technique consists in scanning a range of voltages, between $V < 0$ V and V > open-circuit voltage (V_{OC}), while recording the generated current. The scan is performed either in *reverse* direction from V_{OC} to V=0, or in *forward* direction from V=0 to $V_{OC.}$

The *J-V* curve and *power-V* curves of an ideal solar cell are shown in Figure 3.2. The cell *power density* is given by

$$P = JV. \tag{3.3}$$

The *maximum power point* (*MPP*) corresponds to a point at which the product of the current density and voltage (J_{MPP}, V_{MPP}) is maximum. As shown in Figure 3.2, the V_{OC} is the maximum voltage generated by a solar cell, and it occurs at zero current. The *short-circuit current* density (J_{SC}) is the current through the solar cell when the voltage across the solar cell is zero. The *fill factor* is defined as the ratio

$$FF = \frac{J_{MPP}V_{MPP}}{J_{SC}V_{OC}}, \tag{3.4}$$

and describes the 'squareness' of the *J-V* curve. The *power conversion efficiency* (*PCE*) of the cell is given by,

$$PCE = \frac{J_{MPP}V_{MPP}}{P_S} = \frac{J_{SC}V_{OC}FF}{P_S}, \tag{3.5}$$

where P_S is the irradiance or incident light power density (Nelson, 2003). The four quantities: J_{SC}, V_{OC}, *FF* and *PCE* are the key performance characteristics of a solar cell and will be referred to in this work as the *photovoltaic* (PV) *parameters*.

An important feature in perovskite solar cells is the hysteresis in current-voltage measurements. In theory the measured *J-V* curve should be independent of the sweep direction, nonetheless hysteresis occurs due to deviations from the steady state. In order to quantify the hysteretic behavior, a hysteresis index (HI) can be calculated at the *MPP* using the formula,

$$\frac{(J_{MPP})_{rev} - (J_{MPP})_{fwd}}{(J_{MPP})_{rev}}, \tag{3.6}$$

Where the *reverse* direction of the sweep is from *open-circuit* to *short-circuit* and the *forward* direction is the inverse.

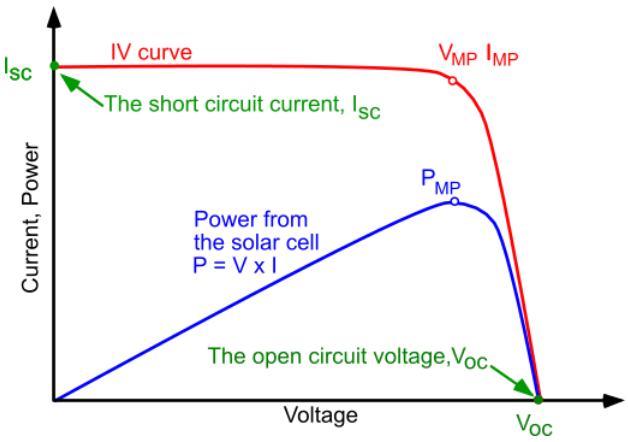

Figure 3.2 Current-voltage and power-voltage curves of an ideal solar cell.

The PV parameters were measured under two different conditions, depending on the place of fabrication of the devices. Within the TFPV group at imec, the devices were measured under a nitrogen atmosphere using a Keithley 2602A Source-Measure Unit and an Abet solar simulator with 100 mW cm^{-2} simulated AM 1.5G illumination, using a calibrated ISE Fraunhofer certified Si photodiode equipped with a KG-5 band pass. In the Nanomaterials' lab at CINVESTAV, the measurement was performed under ambient atmosphere using an Autolab PGSTAT302N and a xenon arc lamp, Oriel 66924 equipped with AM 1.5G and water filters; the calibration is performed with a Newport calibrated reference Si solar cell with an incorporated KG-5 optical filter.

3.2.7 Impedance

Impedance spectroscopy (IS) has demonstrated to be a powerful tool to characterize electrochemical systems, providing information about its electrical properties. IS consists of the measurement of the AC electrical current, $\hat{I}(\omega, t)$, as a function of the angular frequency, ω, when a certain AC voltage, $\hat{V}(\omega, t)$, is applied to the system. During an impedance measurement, the steady state of the system is achieved by applting a DC offset and fixed illumination intensity, and superimposing a small amplitude AC voltage signal. The impedance $Z(\omega, t)$ is measured by scanning the frequency at a range typically from 1 mHz to 10 MHz, and is calculated through Ohm's law, i.e. $Z = V/I$.

The sinusoidal input and output signals are given by,

$$V = V_0 e^{j\omega t}, \tag{3.7}$$

$$I = I_0 e^{j(\omega t - \theta)}, \tag{3.8}$$

where V_0 and I_0 are the amplitudes, ω is the angular frequency given by $\omega = 2\pi f$, where f is the frequency, and θ is the phase angle between input and output signals. Using the complex number notation, the impedance is found to be,

$$Z(\omega, t) = \frac{V_0}{I_0} e^{j\theta} = |Z(\omega)| e^{j\theta}. \tag{3.9}$$

Graphically, the impedance can be represented in the complex plane reporting Z'' as a function of Z', referred to as a Nyquist plot. Additionally, in Bode plots, $\log|Z|$ and θ are graphed as a function of $\log(f)$.

An impedance spectrum is composed of separate features distinguishable in the frequency domain; each of them is related to an electrical process with a characteristic time constant. The most commonly used method of analysis consists in applying equivalent circuits to model the system response to the input signal and to obtain the electrical element values of each feature. The simplest circuit element is the resistor: in this case the current response is in phase with the excitation ($\theta = 0$), and Eq. 3.8 becomes,

$$Z_R(\omega, t) = \frac{V_0}{I_0} = R. \tag{3.10}$$

For a capacitor, the current can be expressed as a function of the voltage as $I(\omega, t) = C(dV(t)/dt) = C\omega V_0 e^{j(\omega t + \frac{\pi}{2})}$, hence, the current response is out of phase with respect to the voltage with $\theta = -\pi/2$. The capacitor is a purely imaginary component and its impedance in the complex form becomes,

$$Z_C(\omega, t) = \frac{1}{j\omega C}. \tag{3.11}$$

Similarly, for an inductor, the voltage can be expressed as a function of the current as $V(t) = L(dI(t)/dt)$. The inductor results in a purely imaginary component with phase angle $\theta = \pi/2$ and its impedance is given by,

$$Z_L(\omega, t) = \omega L e^{\frac{j\pi}{2}} = j\omega L. \quad (3.12)$$

The impedance response of a real system often shows non-ideal capacitive behavior. In these situations, the circuit can be modelled using a constant phase element (CPE). The impedance of a CPE is therefore given by,

$$Z_Q(\omega, t) = \frac{1}{Q(j\omega)^P}. \quad (3.13)$$

Where *Q* is the CPE pre-factor and *P* is the CPE index with value between 0 and 1; i.e., if *P*=1, the CPE behaves like a capacitor (Sacco, 2017).

A simple electrical circuit often found is the Voigt element, which consists of a of a resistance and a capacitor in parallel, Fig 3.3a. The impedance response in a Nyquist plot is in the form of a semicircle centered at *R*/2. In practice the semicircle in the Nyquist plot appears displaced with center at R_s + *R*/2, Fig 3.3b. In this case the Voigt element is used in addition of a series resistance, and the equivalent impedance is given by,

$$Z = R_s + \frac{R}{1+j\omega RC}. \quad (3.14)$$

In Eq. 3.13 the product *RC* has the dimension of time and is a characteristic time constant. At the same time, the inverse is the characteristic frequency associated to the process,

$$\tau = \frac{1}{\omega} = RC. \quad (3.15)$$

Bode plots of $\log|Z|$ and θ as a function of $\log(f)$ are shown in Fig. 3.3b.

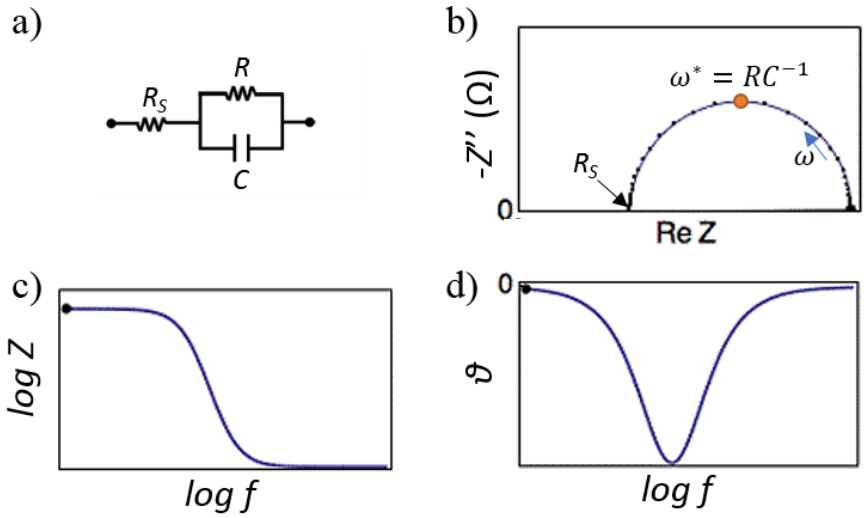

Figure 3.3. a) Electrical circuit of a resistance in series with a Voigt element. Impedance response of the shown electrical circuit: b) Nyquist plot, and c), d) Bode plots.

CHAPTER 4

Insertion of a Low Temperature TiO_2 Mesoporous Layer in Planar Mixed Hybrid Perovskite Solar Cells

CHAPTER 4

Insertion of a Low Temperature TiO_2 Mesoporous Layer in Planar Mixed Hybrid Perovskite Solar Cells

Abstract

We used low temperature (LT) processing (≤ 120 ^oC) to fabricate high-efficiency planar and mesoscopic TiO_2-based hybrid perovskite solar cells with comparable performance, highlighted by a champion LT mesoscopic solar cell with 16.2% efficiency. Comparison of LT and high temperature (HT) devices suggest that a HT treatment (≤ 500 ^oC) of the mesoporous (mp) layer is not essential in this type of devices. Photovoltaic efficiencies of 14% - 16% have been achieved for a mp film thickness ranging from 120 to 480 nm by fine-tuning the precursor solution chemistry.

4.1 Introduction

LT processed organic-inorganic halide perovskite solar cells (PSCs) are promising for semi-transparent and flexible photovoltaics, combining the remarkable optoelectronic characteristics of these hybrid perovskites with scalability and low energetic cost. Although the light-absorbing and hole-conducting materials in PSCs do not require HT treatments, the electron transport layer (ETL) usually does, particularly when a mesoporous (mp) film, typically consisting of TiO_2 nanoparticles (NPs), is included in the mesoscopic configuration.

We developed a route to prepare mesoscopic TiO_2-based PSCs at low temperature (LT) ($T \leq 120$ °C). The results show high-efficiency mesoscopic PSCs in the range of 14% to 16% for a mp film-thickness ranging from 120 nm up to 480 nm; this is to our knowledge the first report where a high solar cell efficiency is maintained for thick mp-films. Generally, cells with thicker metal oxide supports are reported with lower power conversion efficiency (PCE), for example, by Yang *et al.* and Lee *et al.* (D. G. Lee et al., 2017; J. Yang, Fransishyn, & Kelly, 2016), Fig. 4.1. The decrease in PCE has been related to charge transport limitations of the electrode thus, a mp layer of limited thickness of up to 150 nm is generally recommended.

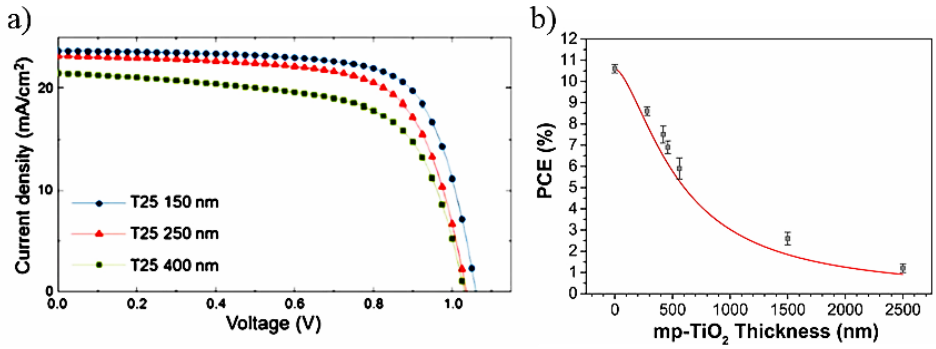

Figure. 4.1. a) Reported *J-V* curves of perovskite solar cells with mp-TiO_2 layer thicknesses of 150 nm, 250 nm, and 400 nm (D. G. Lee et al., 2017). b) Reported power conversion efficiency of mesoscopic PSCs as a function of mp-TiO_2 layer thickness; adapted from Yang *et al.* (J. Yang et al., 2016).

In this Chapter, a route to obtain optimized LT mesoscopic-TiO_2 PSCs is presented. LT mesoscopic PSCs were prepared with three different values for the mp-TiO_2 thickness: 120, 300 and 480 nm, and compared to LT planar PSCs. The importance of adjusting the mixed hybrid perovskite precursor solution chemistry for different mp-TiO_2 layer thicknesses is demonstrated. The results show that when proper infiltration of the mixed hybrid

perovskite into the mp layer is achieved, the latter's thickness has a minimal influence on the PCE of the devices.

4.2 Experimental

Both LT planar and mesoscopic PSCs were prepared. The 20 nm TiO_x compact (c-TiO_x) layer was prepared using e-beam physical vapor deposition. The mp layer was obtained by depositing a film of TiO_2-anatase NPs with particle size between 15-25 nm. The NPs were prepared using a variation on the standard sol-gel method reported by Ito *et al.* (Ito et al., 2008), as described in Section 3.1.4, Chapter 3. A spin-coating ink was prepared by dispersing the TiO_2 NPs in butanol at 1.2 wt.%, and by adjusting the pH to control the ζ-potential at a value of 8 mV; the dispersion was stable for 8 to 12 weeks. The mp-TiO_2 film was prepared by spin coating 60 μL of the ink onto the compact TiO_2 underlayer at 4500 rpm for 30 s until a 60 nm-thick layer was obtained. The number of repetitions was adjusted to achieve the desired thickness and the film was finally annealed for 60 min at 120 °C. The obtained ITO/c-TiO_x and ITO/c-TiO_x/mp-TiO_2 electrodes were used for the preparation of PSCs. Both LT mesoscopic and planar PSCs were fabricated with the intermolecular exchange method as reported by Seok *et al.* (W. S. Yang et al., 2015) (Section 2.2 in Chapter 2), using a mixed perovskite containing methyl ammonium iodide (MAI) and formamidinium iodide (FAI) and methyl ammonium bromide (MABr) (FA/MA-Pb-I/Br) with the final, estimated composition of $FA_{0.71}MA_{0.29}PbI_{2.9}Br_{0.1}$. Details on the experimental procedure to obtain the solar cell devices are given in Section 3.1.6, Chapter 3.

4.3 Results

4.3.1 Insertion of the mesoporous TiO_2 layer

One of the main differences between planar and mesoscopic PSCs is the larger surface area at the perovskite/ETL interface, which would provide a better electron extraction capability. Even though the need of a conducting material for the mp layer has been discarded, anatase TiO_2 is still the most used material because of the high efficiencies achieved (Mahmood, Sarwar, & Mehran, 2017). Its effectiveness relies on the higher photocurrent obtained compared to other materials such as Al_2O_3 that may result in a higher open-circuit voltage (V_{OC}) (Listorti et al., 2015). However, it is important to obtain anatase NPs with good crystallinity and of the optimal particle size. The corresponding X-ray diffraction pattern and a representative SEM image of the anatase NPs prepared in this work are shown in Fig. 4.2. The XRD patterns agrees with the JCPDS card no. 21-1272 (anatase TiO_2). There are no spurious diffraction peaks found in the pattern. According to the SEM micrography, the obtained NPs are round shaped with particle size between 15-25 nm.

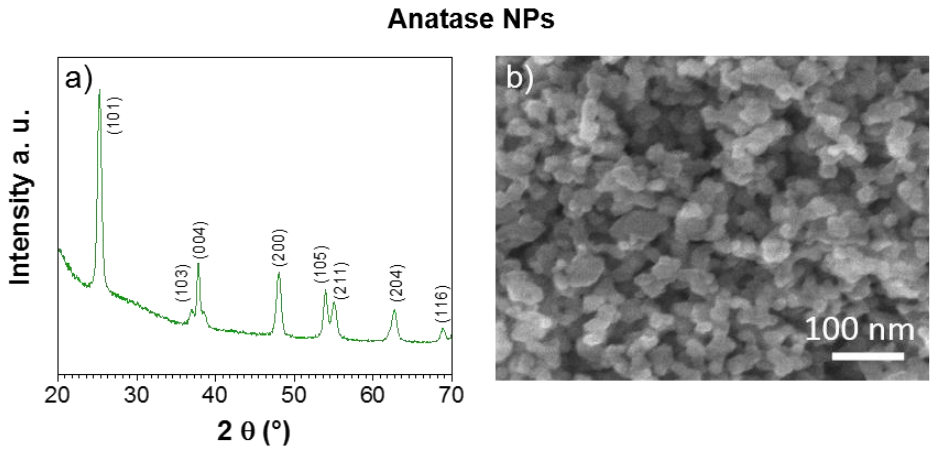

Figure. 4.2. a) X-ray diffraction spectroscopy (XRD) pattern of anatase TiO_2 NPs obtained by the sol-gel method. b) SEM (SEI: secondary electron imaging) image of anatase TiO_2 NPs.

The performance of PSCs in both the planar and mesoscopic configurations has been shown to depend on the thickness of the mixed hybrid perovskite overlayer. In addition, for mesoscopic PSCs the performance has been reported to vary with the mp-layer thickness, with optimum values anywhere between 150 – 280 nm, depending on the size and structure of the NPs (Abdi-Jalebi et al., 2016; H. S. Kim & Park, 2014; D. G. Lee et al., 2017; J. Yang et al., 2016). Hence, in order to maximize performance, the thickness of both layers needs to be optimized.

Mesoscopic PSCs were prepared with four different values for the mp-TiO_2 thickness: 60, 120, 300 and 480 nm, where the thickness was controlled by the number of spin-coating cycles. For comparison, planar PSCs were also prepared with every batch of mesoscopic cells, corresponding to the "0 nm" system. In Figure 4.3a the current-voltage (*J-V*) curves of the highest performing devices are presented. The curves show that the photovoltaic (PV) performance decreases with increasing mp-layer thickness: both the fill factor (*FF*) and short-circuit current density (J_{SC}) decrease significantly. Nonetheless, the V_{OC} is higher for devices with mp-layer thickness ≥ 120 nm. The solar cells with the 60 nm mp-layer demonstrate a performance very similar to planar devices with a somewhat lower V_{OC}, possibly due to uncovered pinholes on the compact layer. The results show that the decrease in J_{SC} might be originated by an increased series resistance; shunting paths are only present for the thicker (480 nm) mp-TiO_2 layer. These results are in accordance with what has been reported before relating a decrease in PV performance of thick mp-layers to an increased interfacial series resistance with increasing TiO_2-TiO_2 interfacial area (D. G. Lee et al., 2017; J. Yang et al., 2016).

It is known that a high temperature treatment of the mp layer results in a film of interconnected NPs with improved electrical characteristics (Zardetto et al., 2013). Therefore, in order to determine if the decrease of the photocurrent was caused by a lack of NP interconnection, mesoscopic devices were prepared with annealing treatment at 500 °C using the NP dispersion. Mesoscopic HT PSCs exhibited higher performance than LT devices, as shown in Figure 4.3b. In particular, the value of J_{SC} is higher in the HT devices, although it decreases with increasing mp film-thickness. Interestingly, HT devices with a 480 nm-thick mp-TiO_2 film displayed a J_{SC} only slightly higher than obtained for LT PSCs. Comparison of J_{SC} vs. mp-TiO_2 film thickness for both LT and HT PSCs are shown in Figure 4.3c. Both, the HT and LT devices show a decrease in photocurrent. However, for the HT devices the decrease follows a lineal tendency, while the LT devices seem to decrease exponentially.

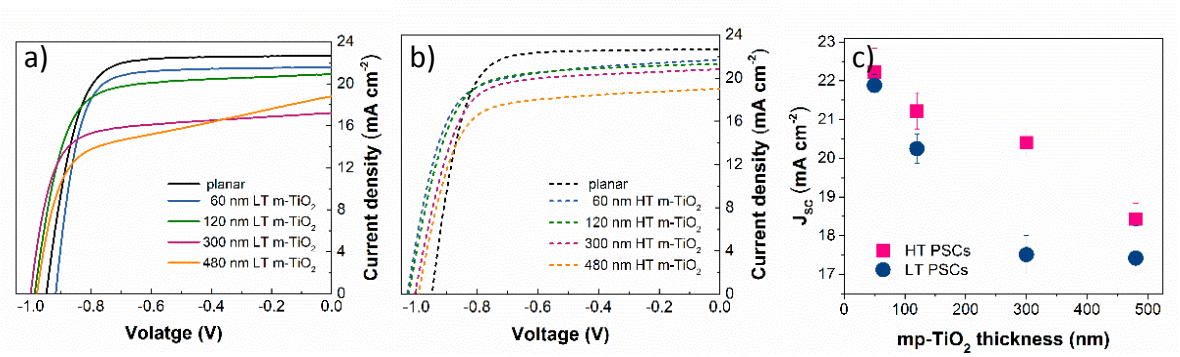

Figure. 4.3. *J-V* curves of the highest performing devices with mp-TiO_2 thickness: 0, 60, 120, 300 and 480 nm: a) LT mesoscopic PSCs and b) HT mesoscopic PSCs. c) J_{SC} vs mp-TiO_2 thickness for both LT and HT devices. The PV characteristics of the cells were measured in the reverse scan direction from -1.2 to 0.25 V with scan rate 0.1 V s^{-1}.

The functions of a mp-TiO_2 layer are: i) to separate electrons and holes in the perovskite layer by fast electron injection to the TiO_2 layer, and ii) to transport the injected electrons to the electrode. From this, it follows that charge transport and recombination properties of the devices should be affected by the mp film-thickness. In mesoscopic PSCs, an increased effect of recombination is mainly related to an increased number of trap sites as the mp-TiO_2 thickness increases, and is reflected in V_{OC} decline. On the other hand, charge transport depends on the electrical properties at both TiO_2/TiO_2 and perovskite/TiO_2 interfaces, affecting the diffusion length, and is reflected in a decrease of both J_{SC} and *FF*.

LT devices showed relatively stable V_{OC} thus, a change in the recombination kinetics is not likely to be important. At the same time, both J_{SC} and *FF* decrease (from 22 to 18 mA cm^{-2} and from 74% to 60%, respectively). This implies a high contact resistance, either due to bad TiO_2 NPs interconnection or to bad contact at the perovskite/TiO_2 interface. On the other hand, HT devices also showed a decrease in both J_{SC} and *FF* for thicker films, which points to a phenomenon that is not related to the TiO_2 NPs interconnection.

4.3.2 Optimization of the perovskite infiltration

In the mesoscopic configuration two different grain domains of perovskite coexist: pore-infiltrated and of the capping layer (Listorti et al., 2015). The mp scaffold might be filled with the PbI_2 solution prior to the formation of an overlayer during the spin coating process. To investigate the effect of the mp-TiO_2 thickness on the perovskite/TiO_2 interface, careful control of both domains is essential. SEM images in Figure 4.4 illustrate that incomplete infiltration is obtained for a mp film of 200 nm if a 1.15 M PbI_2 solution is used, while full infiltration is observed using a 1.25 M PbI_2 solution. These results indicate that the mixed hybrid perovskite precursor solution chemistry is critically important for the

infiltration of the PbI_2, in agreement with a previous report (Bi, El-Zohry, Hagfeldt, & Boschloo, 2015), and that poor infiltration might cause high interfacial resistance. It was found that complete infiltration can be achieved for mp-layer thickness up to 480 nm using adjustments in the spin-coating solution chemistry as shown in Table 1. The concentration of DMSO was kept constant to properly use the intramolecular exchange method. The reactant concentrations in solution B were also adjusted, maintaining the concentration ratios the same.

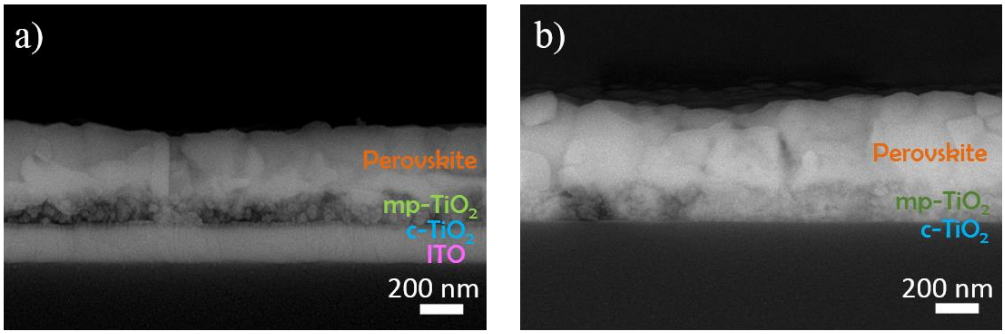

Figure. 4.4. SEM-LABE images of mp-TiO_2 scaffolds with a spin-coated FA/MA-Pb-I/Br hybrid perovskite layer deposited on top; a) 1.15 M PbI_2 solution (glass/ITO/c-TiO_2/mp-TiO_2/perovskite); b) 1.25 M PbI_2 solution (glass/c-TiO_2/mp-TiO_2/perovskite). The scale bars correspond to 200 nm.

4.3.3 Optimization of the perovskite overlayer

With increasing mp-TiO_2 film thickness, a concomitant decrease of thickness of the FA/MA-Pb-I/Br overlayer was observed, which is also an important parameter to optimize. To achieve the desired thickness of the perovskite over layer the spin-coating velocity was varied, the used velocities for each case are presented in Table 4.1. Figure 4.5 shows the J_{SC} and V_{OC} values of LT mp-TiO_2 (120 nm) PSCs as a function of the thickness of the mixed

Table 4.1: Optimized concentrations of solutions A and B used for the deposition of the FA/MA-Pb-I/Br mixed hybrid perovskite film on mp-TiO_2 scaffold layers of different thickness.

mp-TiO_2 thickness (nm)	**[PbI_2] (M)**	**[FAI] (mM)**	**[MAI] (mM)**	**[MABr] (mM)**	**Spin-coating velocity [rpm]**
0	1.25	314	90	68	3000
60	1.25	314	90	68	3000
120	1.25	314	90	68	2500
300	1.35	330	94	71	2800
480	1.50	367	105	79	3500

hybrid perovskite overlayer in the range between 150 and 600 nm. The J_{SC} reaches a maximum value of about 22 mA cm^{-2} for a device with a 385 nm overlayer and remains constant for thicker films. The open circuit voltage reaches a maximum of 0.99 V for an overlayer thickness of 480 nm and decreases significantly for thicker films.

Hence, the optimum thickness of the overlayer for a LT mp-TiO_2 (120 nm) PSC was defined to be 480 nm. Remarkably, in planar devices the perovskite optimum film thickness is also 480 nm (Qiu et al., 2017). This observation is in accordance with previous reports of the overlayer thickness determining the performance of the device (Listorti et al., 2015), independent of the architecture used, and is consistent with the impedance spectroscopy (IS) results obtained in this work, which are discussed in Chapter 6.

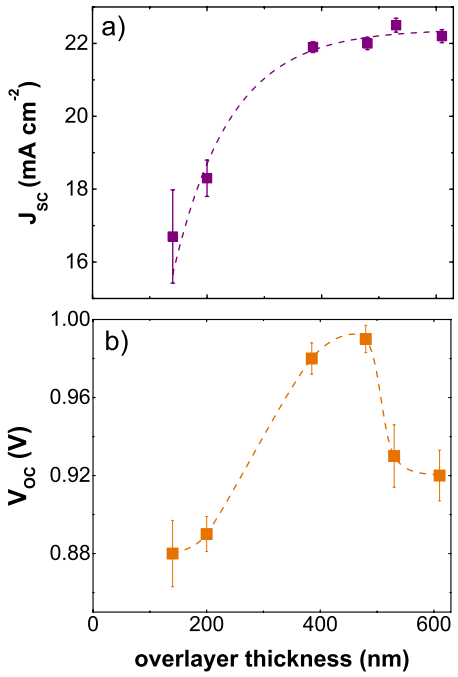

Fig. 4.5. Dependence of J_{SC} and V_{OC} of LT mp-TiO_2 PSCs on the FA/MA-Pb-I/Br mixed hybrid perovskite overlayer thickness, using a 120 nm mp-TiO_2 layer.

4.3.4 Optimized mesoscopic devices with various mp-layer thicknesses

After carefully tuning the spin coating solution chemistry, for good infiltration and proper capping layer thickness, the optimized devices displayed stable values of photocurrent and *FF*. To our knowledge, there are no previous reports of mesoscopic cells maintaining a high *FF* at these large values of the mp-TiO_2 film thickness, with particle size > 20 nm. The *J-V* curves of representative optimized devices show that the most important difference between these devices is a decrease in J_{SC} that is not related any more to shunting paths, and seem to be little influenced by an increased series resistance in thicker devices (Fig 4.6).

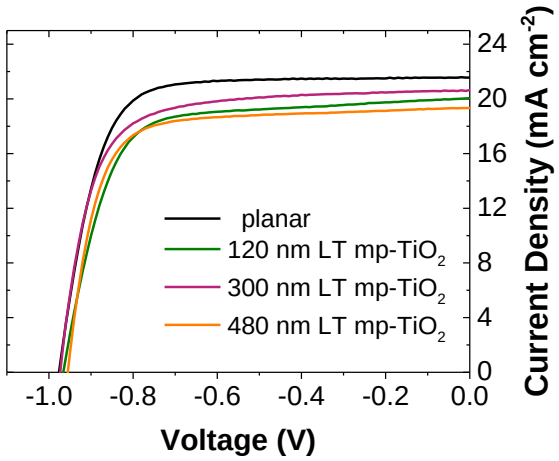

Figure. 4.6. *J-V* curves of representative devices with mp-TiO_2 thickness: 0, 120, 300 and 480 nm after optimization of the perovskite overlayer and infiltration. The PV characteristics of the cells were measured in the reverse scan direction from -1.2 to 0.25 V with scan rate 0.1 V s^{-1}.

Figure 4.7 shows the photovoltaic parameters of both non-optimized and optimized mesoscopic PSCs as a function of mp-TiO_2 film thickness, illustrating the improvement of the solar cell performance for the optimized devices. The resulting devices demonstrated a *PCE* of 14% or larger, even for a 480 nm LT mp-TiO_2 film. Interestingly, the insertion of the LT mp layer into the planar configuration results in an increase of V_{OC} from 0.98 V to 1.1 V. The combined results suggest that the inclusion of a mp-layer decreases the recombination kinetics, either by decreasing the effect of pin holes in the blocking layer or by more efficient electron extraction. It is important to notice that the bandgap of TiO_x has been reported to be larger than that of TiO_2 by 0.2 - 0.3 eV (Ju, Li, Wu, & Jiang, 2011; S. H. Lee, Yamasue, Ishihara, & Okumura, 2010), which might be at the origin of the V_{OC} improvement. The improved *FF* also indicates more efficient electron extraction and shows that the electrical properties of the LT mp-TiO_2 film are adequate for an optimized PSC. Accordingly, the

decrease in J_{SC} seems to be related to a parasitic absorption of light from thicker mp-TiO_2 films. Based on the photovoltaic measurements, we conclude that the mp-TiO_2 interlayer thickness has a minimal detrimental effect on charge transport properties if good interfacial contact at the perovskite/TiO_2 interface is guaranteed.

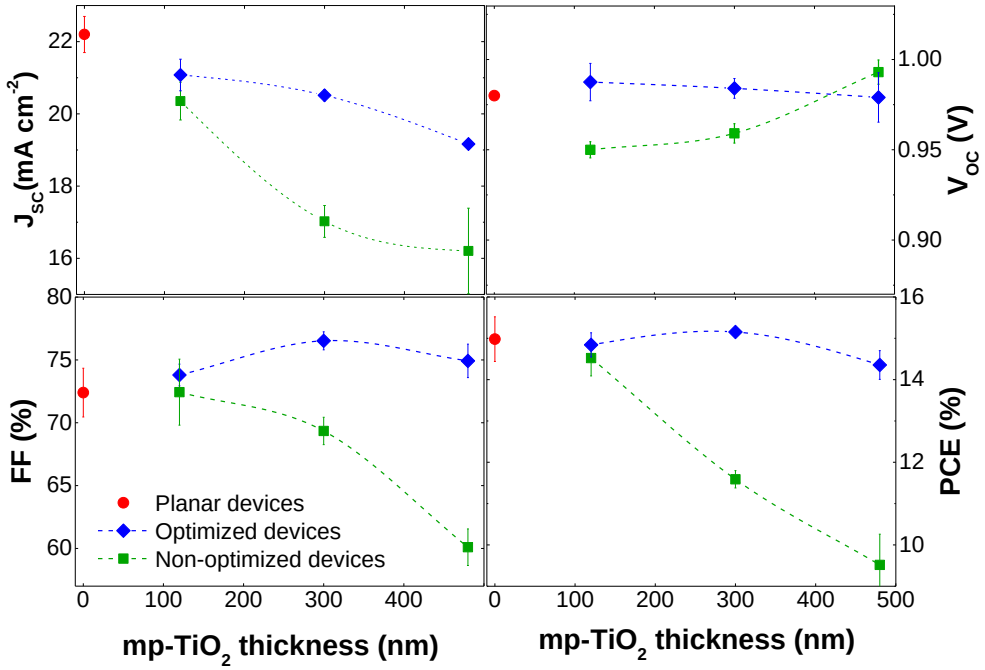

Fig. 4.7. Solar cell parameters versus the mp-TiO_2 film thickness for LT PSCs before and after optimization of the mixed hybrid perovskite layer. At x=0, the parameters for the planar devices fabricated at the same time are shown.

4.3.5 Photovoltaic and Optical Characterization

Optimum mesoscopic TiO_2-based LT-PSCs were prepared using a 120 nm LT mp-TiO_2 film and 480 nm FA/MA-Pb-I/Br hybrid perovskite overlayer, with a reproducible conversion efficiency of 15.6 ± 0.5% (n = 72 cells). Figure 4.8 shows a cross-sectional SEM-

LABE image of a mesoscopic LT PSC optimized in this study, the stack consists of a 20 nm-thick c-TiO_x prepared by e-beam evaporation, a LT mp-TiO_2 layer of 120 nm, a 480 nm-thick layer of $FA_{0.71}MA_{0.29}PbI_{2.9}Br_{0.1}$, a spiro-OMeTAD layer of 200 nm and an evaporated Au layer of 90 nm. In addition, the *J-V* curve of the best performing device is shown in Figure 4.8 with a *PCE* of 16.2%, J_{SC} = 22.3 mA cm^{-2}, V_{OC} = 1.00 V, and *FF* = 72.8 %, in the reverse scan. The hysteresis index (HI) was calculated using Eq. 3.6 with a value of the is 0.3, which is in accordance with values reported in the literature (H. S. Kim & Park, 2014; Yu et al., 2016).

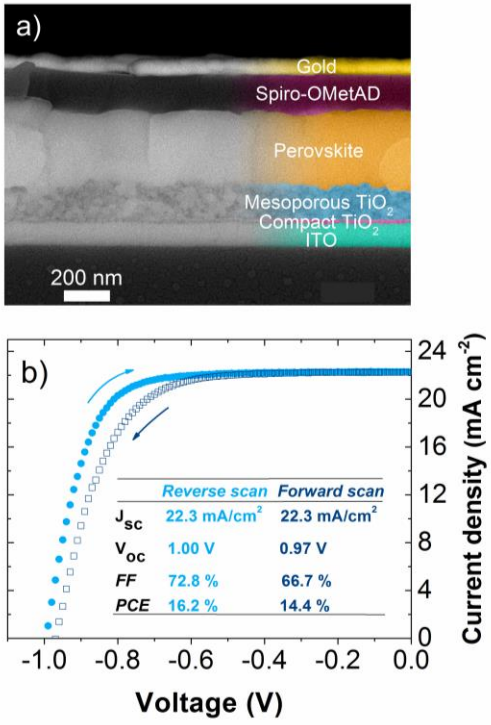

Figure 4.8. a) Scanning electron microscope (SEM-LABE) image of a mesoscopic perovskite solar cell fabricated by the LT process with a 120 nm mp-TiO_2 layer. b) *J-V* curves of the champion LT mp-TiO_2 PSC; the scan rate is 0.1 V s^{-1}.

External quantum efficiency (*EQE*) and absorptance spectra of planar, and mesoscopic LT and HT (500 °C) are shown in Figure 4.9a. The reduced *EQE* in the "blue" region of the spectrum ($\lambda < 350$ nm) indicates a certain degree of front surface recombination. At the "red" portion of the spectrum, the *EQE* of mesoscopic and planar devices present differences that do not appear to be originated from a difference in the absorptance. This has been observed before in simulated *QE* values of devices with different TiO_2 thicknesses (Qarony et al., 2015). However, the integrated current density results in very similar values for the three different types of devices.

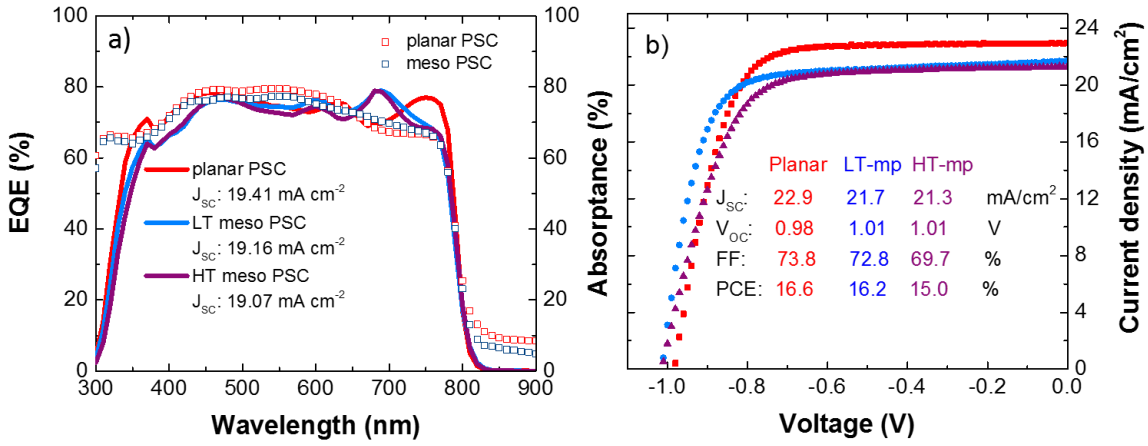

Figure 4.9. a) External quantum efficiency (solid line) and absorptance spectra (squares) of the record planar and mesoscopic cells; the integrated EQE current is indicated. b) Current – voltage curves of the champion planar and HT mesoscopic PSC, reverse scan; the scan rate is 0.1 V s^{-1}.

J-V curves of planar, and mesoscopic LT and HT (500 °C) are shown in Figure 4.9b. The best planar device gave a *PCE* of 16.6% with J_{SC} of 22.9 mA cm^{-2}, V_{OC} of 0.98 V, and *FF* of 73.8 %, in the reverse scan. The best mesoscopic HT device gave a *PCE* of 15.0% with J_{SC} of 21.3 mA cm^{-2}, V_{OC} of 1.01 V, and *FF* of 69.7 %, in the reverse scan; note that the

electrical conductivity of ITO is affected by the HT treatment, which affects the *FF*. These results illustrate the successful insertion of the LT mp-TiO_2 layer into the solar cells. Please note that the difference on the extracted J_{SC} from the EQE and *J-V* curves might be due to an error in measuring the active area.

In Figure 4.10, the steady-state photoluminescence (PL) spectra of FA/MA-Pb-I/Br hybrid perovskite deposited on top of mp-TiO_2, c-TiO_2 and Al_2O_3 films are shown. It can be observed at the PL spectra of the perovskite deposited on compact TiO_2 and alumina films an emission peak centered at 790 nm; the peak matches the absorption onset of the FA/MA-Pb-I/Br hybrid perovskite (Jesper Jacobsson et al., 2016). The spectrum of the mixed hybrid perovskite deposited on the mp film presents strong quenching.

PL quenching has been related to efficient electron (hole) extraction by the electron (hole) transport material (Azmi et al., 2018; Q. Jiang et al., 2016; Valadez-Villalobos et al., 2019; M. Wang et al., 2018); accordingly, for the alumina ETL where electron extraction does not occur, the PL emission presents the stronger intensity. The observed PL emission of the mixed hybrid perovskite in the different configurations demonstrate the superior electron extraction efficiency of the mp-TiO_2 layer. This result agrees with the superior electrical properties attributed to crystalline TiO_2 (Zardetto et al., 2013).

4.4 Conclusions

We demonstrate that mp-TiO_2 layers with good electrical properties can be prepared with low temperature processing ($\leq 120\ ^oC$). It was found that optimization of the perovskite solution chemistry leads to proper infiltration of the PbI_2 solution into the mp scaffold, resulting in high efficiency PSCs with mp-TiO_2 layer-thickness up to 480 nm

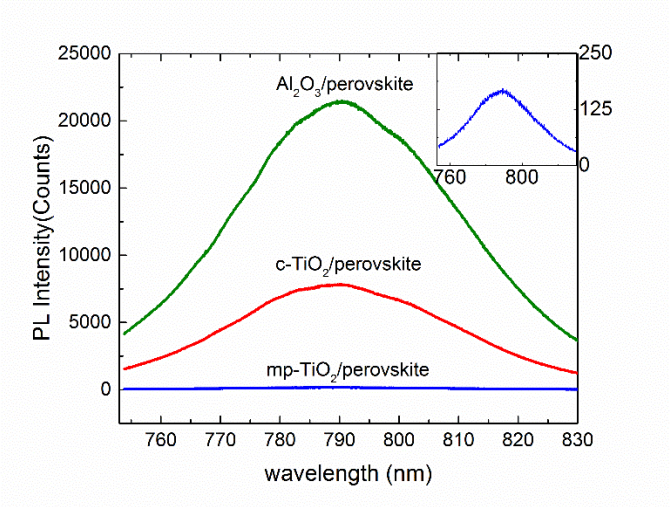

Figure 4.10. Photoluminescence spectrum of FA/MA-Pb-I/Br hybrid perovskite deposited on mp-TiO_2 (blue), c-TiO_2 (red) and Al_2O_3 (green), the excitation wavelength is 660 nm.

Increased values for the *FF* and J_{SC} were obtained after the optimization; these properties were interpreted as related to a reduced electrical resistance due to a better interfacial contact at the perovskite/TiO_2 interface. The optimum perovskite capping layer thickness in mesoscopic PSCs was found to be 480 nm, which is equal to the optimum thickness of the perovskite layer in planar PSCs, this suggests that the electrical properties of this type of devices are dominated by the bulk of the absorbing material. We observed an enhanced electron extraction when using a mp scaffold as ETL, seemingly related to more adequate optoelectronic characteristics of TiO_2 vs TiO_x. The influence of these better electrical properties on the stability of the devices will be discussed in Chapters 5 and 6.

Acknowledgment

The author would like to thank the Thin Film Photovoltaics group and technicians at Imec for the collaboration and facilitation for the use of equipment.

CHAPTER 5

Mesoporous TiO_2 Layer in Low-Temperature Perovskite Solar Cells: Study of the Stability

CHAPTER 5

Mesoporous TiO_2 Layer in Low-Temperature Perovskite Solar Cells: Study of the Stability

Abstract

A critical issue for the viable commercialization of the perovskite solar cell (PSC) is the performance stability under conditions of high relative humidity and exposure to light. There is evidence that PSCs containing a mesoporous (mp) electron transport layer (ETL) benefit from the nanoparticle/perovskite heterojunction, but the origin remains unclear. In this chapter the evolution with time of the photovoltaic (PV) parameters upon exposure to light and moisture is studied in detail. As expected, mesoscopic devices show better stability with half-life time (T_{50}) almost twice than that of planar devices. The decomposition of the hybrid perovskite material is examined for both types of configuration. It is demonstrated that the extraction efficiency of the ETL plays an important role in the performance preservation, despite some chemical decomposition of the perovskite material.

5.1 Introduction

Organic- inorganic hybrid lead halide PSCs are a potentially low cost and efficient PV technology; however, the instability of the hybrid perovskite represents a major drawback. In the early stages of research on PSCs two main configurations emerged: mesoscopic and planar. Advantages of using either of these architectures is still under debate since both have demonstrated certified efficiencies in excess of 20% (Green et al., 2018). Nonetheless, there are indications that PSCs containing a mp-TiO_2 layer exhibit improved stability under exposure to moisture and light when compared to planar heterojunction TiO_2-based devices.

Yang *et al.* (J. Yang et al., 2016) reported a longer time of retained optical absorbance upon exposure to a 98% relative humidity (RH) environment for $CH_3NH_3PbI_3$ (MAPI) films deposited onto mp-TiO_2 as compared to deposited directly onto the compact TiO_2 layer (c-TiO_2). Haque *et al.* (Bryant et al., 2016) compared planar and mesoscopic HT PSCs aged in dry air under 1 sun illumination, and obtained a T_{50} of 0.6 and 2.2 hours, respectively. The improved stability of the solar cells in the mesoscopic configuration is in many cases attributed to a better electron extraction capability, which prevents light-induced degradation processes. On the other hand, in addition to the well-known decomposition pathways of the hybrid perovskite material (D. Wang, Wright, Elumalai, & Uddin, 2016), it is now understood that devices present degradation caused by ionic mobility and redox chemistry (Bastos et al., 2018; Carrillo et al., 2016; Eames et al., 2015; Shlenskaya et al., 2018; W. Tress et al., 2015). Moreover, there are indications that interfacial ion accumulation at the mp-TiO_2/perovskite interface can lower degradation (Gagliardi & Abate, 2018).

In Chapter 4, both planar and mesoscopic low temperature (LT) PSCs using the hybrid organic-inorganic mixed lead halide perovskite $FA_{0.71}MA_{0.29}PbI_{2.9}Br_{0.1}$ were prepared showing comparable PV performance. In this chapter, experimental results for a degradation test of both type of devices are presented. Correlation of the performance of planar and mesoscopic cells after ageing and chemical decomposition of the mixed hybrid perovskite indicates that the presence of the mp-TiO_2 film enhances the lifetime of the device despite some degradation of the perovskite material. Specifically, the half-life time, T_{50}, which is the time it takes for the solar cell to present 50 % if its initial *PCE*, almost doubles for mesoscopic PSCs.

5.2 Experimental

The PV response of as-prepared, *non-encapsulated* planar and mesoscopic LT PSCs was recorded, and the cells were then exposed to air in conditions of relatively high humidity (60% ± 5% R.H.), either under illumination (0.2 sun; AM 1.5G) or in dark; we used a relatively low light intensity to be able to better monitor the degradation. Subsequently, current-voltage (*J*-*V*) curves were recorded after a continuous period of aging of either 20 h or 40 h. The characterization was performed in the TFPV group lab, as described in Section 3.2.6, Chapter 3.

5.3 Results

5.3.1 Evolution of the Photovoltaic Parameters with Degradation

Figure 5.1 shows the solar cell parameters of the devices as-prepared, after 20 h, and after 40 h of ageing. At least 3 separate substrates containing 12 pixels each were used in each experiment for both configurations. It can be seen that the non-encapsulated cells exposed to 60% R.H. in the dark only exhibit a slight decrease in efficiency, maintaining a power conversion efficiency (*PCE*) ≥ 12% for both configurations. On the other hand, under illumination, a significant decrease in the solar cell performance is observed, especially for the planar devices, while maintaining *PCE* < 8% for exposure up to 40 h. This result confirms previously reported observations of light-induced degradation (Ahn et al., 2016; Bryant et al., 2016).

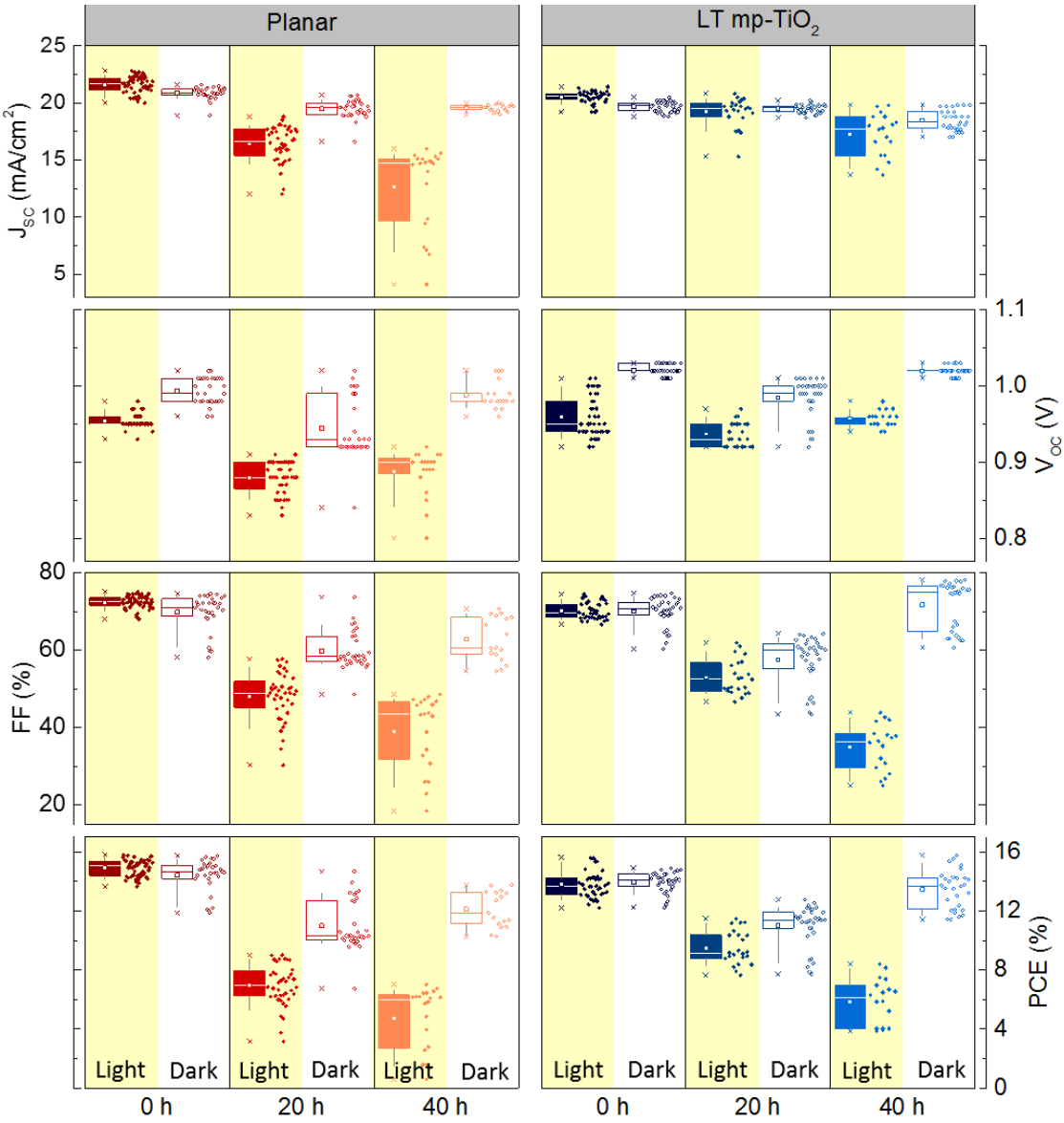

Figure 5.1. Short-circuit current density (J_{SC}), open-circuit voltage (V_{OC}), fill factor (*FF*) and efficiency of planar and low temperature mesoscopic solar cells at 0, 20 and, 40 h of exposure to humidity (60 ± 5 % R.H.) under illumination (closed symbols) or in dark (open symbols): 50% of the data points are within the boxes and 80% within the whiskers. The horizontal line and the point in the boxes represent the median and the mean value, respectively. Two sets of cells were prepared for each configuration, one for the experiments in the dark and the other under illumination; for the as-prepared samples (0 h), the specific sets of cells used in each type of experiment are shown separately although all cells represent the same starting conditions. Half of the as-prepared cells were exposed for 20 h, and the other half for 40 h.

In Table 5.1 the percentages of retained J_{SC}, V_{OC}, *FF*, *PCE* and T_{50} for both configurations aged under illumination are summarized. When examining the PV parameters individually, there are significant differences between both planar and mesoscopic cells. For the planar cells, all PV parameters decrease with ageing time, while for LT mesoscopic cells both the J_{SC} and the V_{OC} are remarkably stable. In both configurations a significant decrease of the *FF* is observed, indicating that degradation may induce an increased cell series resistance or new recombination processes and pathways at the interfaces.

Table 5.1. Retained percentages of the PV parameters for planar and LT mesoscopic PSCs after 20 and 40 h of exposure to 60±5% R.H. in air under illumination at 0.2 sun, AM1.5G.

	Configuration	***Retained Jsc (%)***	***Retained Voc (%)***	***Retained FF (%)***	***Retained PCE (%)***	T_{50}
20 h	Planar	76 ± 5	92 ± 2	66 ± 9	46 ± 9	
	LT-mp-TiO_2	94 ± 5	100 ± 2	77 ± 7	72 ± 8	
40 h	Planar	58 ± 17	93 ± 3	55 ± 14	32 ± 15	20 h
	LT-mp-TiO_2	84 ± 10	97 ± 2	48 ± 9	40 ± 12	> 40 h

Representative *J-V* curves of as prepared and degraded (20 and 40 hours at 60 ± 5% R.H.) devices are shown in Figure 5.2. Besides deterioration of the PV parameters, the hysteretic features of the curves change with the ageing time. In fresh devices, a more pronounced hysteresis is observed in mesoscopic PSCs compared to planar devices, with hysteresis indexes (HI) 0.3 and 0.1 respectively, contrary to what has been reported previously (H. S. Kim & Park, 2014). On the other hand, for the planar configuration, as the cell degrades the hysteresis becomes more pronounced (HI_{meso}=0.3 and HI_{plan} ≥0.5). Hysteresis has been related to the rearrangement of ionic charges, which changes the

depletion region at a rate that is dependent on the activation energy; this affects the *J-V* sweeps giving rise to the observed hysteretic behavior (Calado et al., 2016; B. Chen et al., 2015; Jacobs et al., 2017; W. Tress et al., 2015; Yu et al., 2016). Interestingly, hysteresis in PSCs has been related to charge accumulation at the interfaces, that may lead to long-term degradation (Rizzo et al., 2019). Thus, it is reasonable to think that the faster degradation of the planar PSCs might be related to mobile ionic species accumulating at the perovskite interfaces.

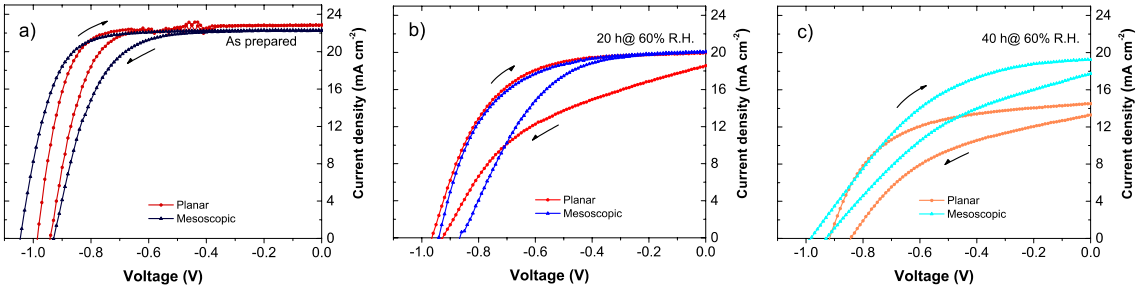

Figure 5.2. Representative *J-V* curves of planar and mesoscopic devices: a) as-prepared; b) degraded for 20 h; and c) degraded for 40 h at 60% R.H. and under illumination. The scan rate is 0.1 V s^{-1}.

5.3.2 Decomposition of the Hybrid Perovskite Material

To examine the decomposition of the hybrid perovskite material due to air and humidity exposure, X-ray diffraction (XRD) analysis and absorbance spectroscopy were performed on $FA_{0.71}MA_{0.29}PbI_{2.9}Br_{0.1}$ films deposited on both c-TiO_x and LT mp-TiO_2. Formation of PbI_2 is expected as the principal degradation product of the decomposition of the hybrid perovskite (Asghar, Zhang, Wang, & Lund, 2017; Berhe et al., 2016; Niu et al., 2015), which causes reduction of the optical absorption yield. Figure 5.3a shows the diffraction patterns of the hybrid perovskite films: after 80 h in the dark no PbI_2 was detected; however, under illumination, a PbI_2 peak was detected for both the planar and mesoscopic

configuration. This result was confirmed for completed, aged PSCs, as shown in Figure 5.3b. From the relative intensity of the PbI_2 (001) peak at 12.5° with respect to the $FA_{0.71}MA_{0.29}PbI_{2.9}Br_{0.1}$ (110) peak at 13.9°, it seems that the amount of lead iodide is even higher in the mesoscopic case.

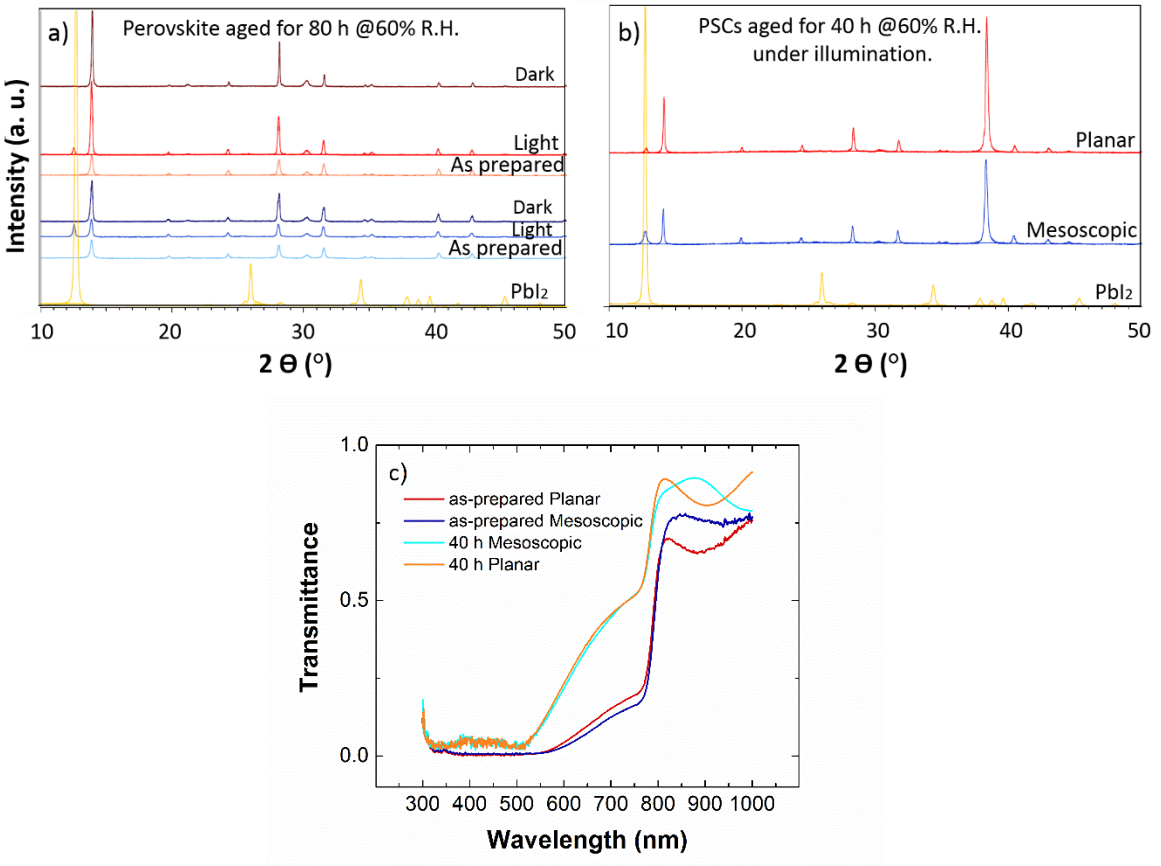

Figure 5.3. XRD diffraction patterns of: a) degraded (80 h @60% R.H. & 0.2 sun AM 1.5G) $FA_{0.71}MA_{0.29}PbI_{2.9}Br_{0.1}$ perovskite: ITO/c-TiO_x/perovskite (red) and ITO/LT mp-TiO_2/perovskite (blue), and b) XRD degraded (40 h @60% R.H. & 0.2 sun AM 1.5G) planar and LT mesoscopic PSCs. The pattern of a pristine PbI_2 film is shown for comparison. c) Transmittance spectra of as-prepared and aged planar and LT mesoscopic PSCs.

UV-Vis absorption was recorded for planar and mesoscopic as-prepared and aged devices; the transmittance spectra are shown in Figure 5.3c. The results show that the formation of PbI_2 is accompanied by a decreased absorbance; nonetheless, both device

configurations present alike increased transmittance in the 500-800 nm range. It is important to mention that a measurement of the reflectance of aged devices is missing; however, changes in optical absorbance have previously been used to highlight degradation of the hybrid perovskite, and specifically accompanied by a change in PbI_2 composition (Du et al., 2017; Jacobsson et al., 2016).

Figure 5.4 shows SEM images of the perovskite films deposited on compact (Figures 5.4 a, c, e) and mp scaffolds (Figures 5.4 b, d, f), which reveal a different change in morphology if films are exposed to humidity, either under illumination or in the dark. When kept in the dark, growth of the grains indicates an effect of coarsening due to humidity, nonetheless, there is no evidence of degradation or PbI_2 formation. In contrast, when exposed to light, PbI_2 crystals of about 300 nm can be observed on the perovskite surface of the ITO/c-TiO_x/perovskite configuration. The ITO/mp-TiO_2/perovskite configuration do not show PbI_2 formation on the surface, however surface degradation is evident. Photographs of completed devices are shown in Figures 5.4 g, h, i, j. In the dark, none of the two configurations present apparent degradation. Nonetheless, planar devices present strong apparent degradation that seems to be affecting the gold counter electrode which is not the case for mesoscopic devices. Deterioration of the metallic electrodes has been observed as a result of chemical reactions with mobile species of the perovskite material (Kato et al., 2015; Shlenskaya et al., 2018).

Henceforth, the observation of a decreased performance in the planar configuration cannot be ascribed to a more severe decomposition of the mixed hybrid perovskite material in this type of devices. It is proposed that, even if chemical degradation occurs, the mesoscopic configuration can retain higher performance, which is due to a larger photocurrent density.

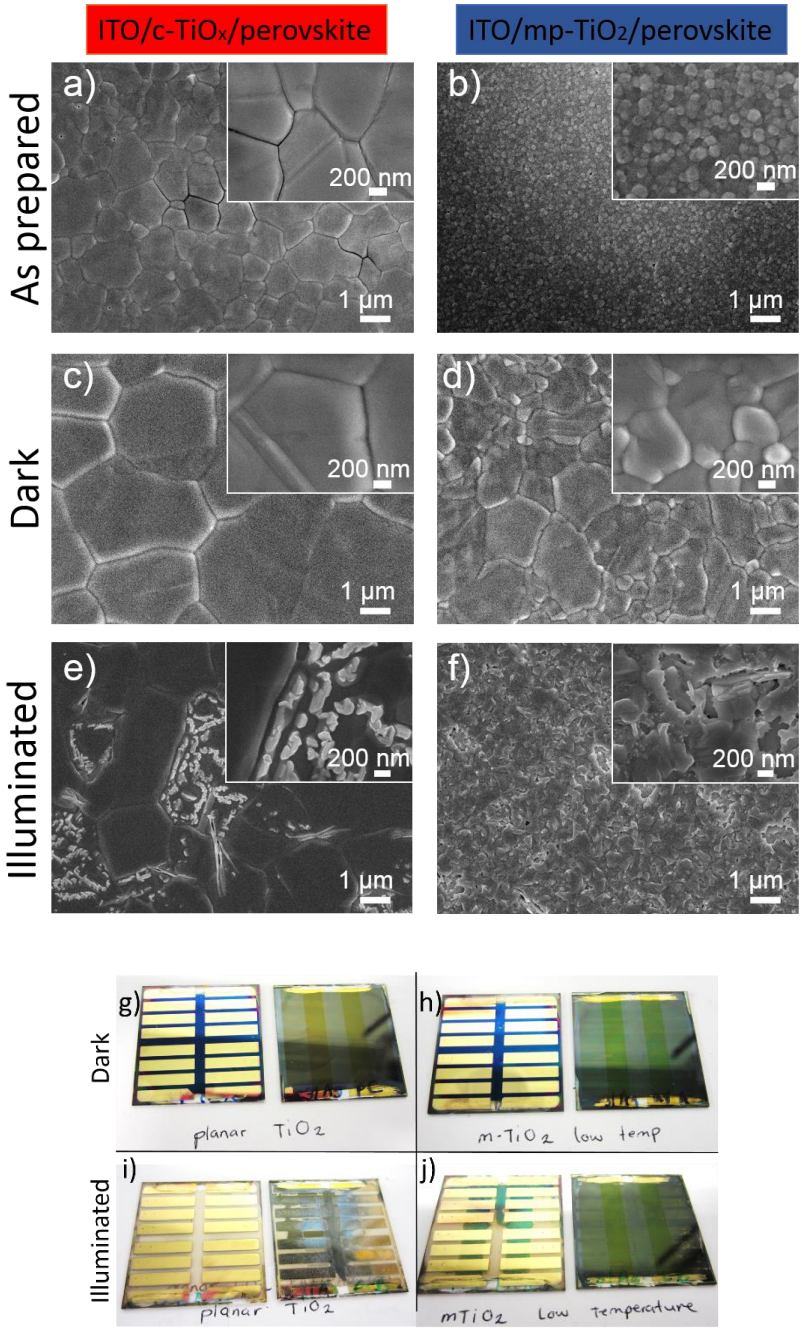

Figure 5.4. SEM (SEI: secondary electron imaging) top-images of $FA_{0.71}MA_{0.29}PbI_{2.9}Br_{0.1}$ film morphology. As-prepared films: a) ITO/c-TiO_x/perovskite and, b) ITO/mp-TiO_2/perovskite. Partially degraded films after 80 h @ 60 ± 5 % R.H.: c) ITO/c-TiO_x/perovskite in the dark; d) ITO/mp-TiO_2/perovskite in the dark; e) ITO/c-TiO_x/perovskite exposed to room illumination; f) ITO/mp-TiO_2/perovskite exposed to room illumination; g), h), i) and j) photographs of planar and mesoscopic PSCs degraded in the dark or under illumination.

5.3.3 Higher J_{SC} Retention in Mesoscopic PSCs

According to the steady-state continuity equation for J_{SC}, the current density is determined by the balance between the generation rate (G_n) and the recombination rate (R_n), which can be expressed as a function of the excess carrier density (Δn) and the carrier lifetime (τ_n):

$$J_n(x) = q \int_0^d (G_n(x) - \frac{\Delta n(x)}{\tau_n})\, dx. \quad (5.1)$$

The generation rate is mainly determined by absorption, which decreases with the same magnitude for both, planar and mesoscopic PSCs, as shown in Figure 5.3c. Therefore, the decrease of J_{SC} in aged planar devices would be originated by an increase in the recombination rate, either because of a reduced carrier lifetime or due to an increased excess carrier density, both causing a deficient carrier extraction efficiency at the interfaces.

In addition to deterioration of the counter electrode, reduced carrier extraction might be affected by the electrical properties of the ETL. In order to study the relation between the J_{SC} decrease and the carrier extraction capacity of the scaffold, Al_2O_3-based mesoscopic PSCs were prepared and tested under the same conditions of light and moisture. The *J-V* curves and retained percentages are shown in Fig. 5.5a; after exposure to light and moisture for 80 h the PV performance is lost, while there is no severe damage in the performance for PSCs aged in the dark. In Fig. 5.5b, the XRD patterns of $FA_{0.71}MA_{0.29}PbI_{2.9}Br_{0.1}$ films are shown for as-prepared films, and after 80 h in the dark and under illumination. A PbI_2 peak was detected in the film exposed to light; the peak corresponds to the (001) reflection of PbI_2. SEM images of the surface of ITO/Al_2O_3/perovskite after exposure to 60% R. H. under illumination or in the dark are shown in Fig. 5.5c, d, e. Accordingly, grain coarsening and

the formation of PbI_2 crystals is evident on the surface of the film aged under illumination. The resulting pronounced degradation of the Al_2O_3-based mesoscopic PSCs is clear evidence of a light induced degradation mechanism related to the electron extraction capacity of the ETL material.

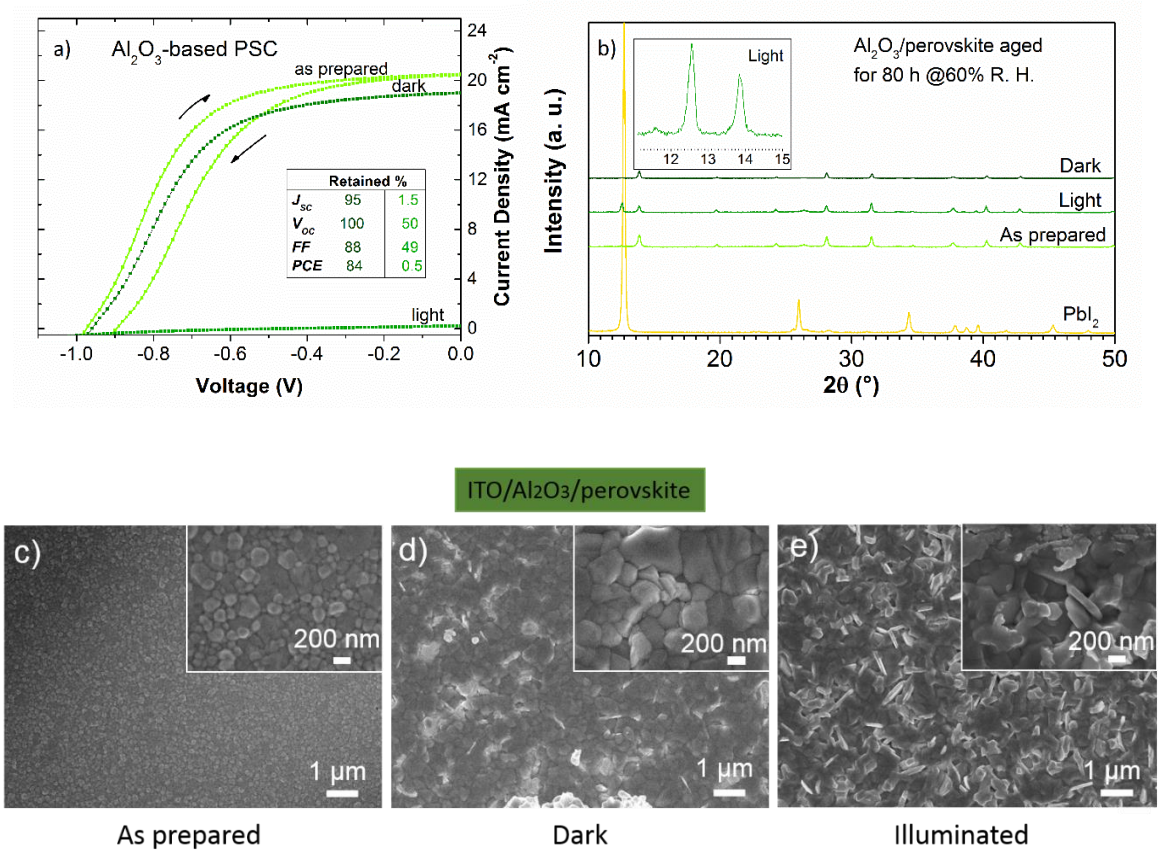

Figure 5.5. a) *J-V* curves of Al_2O_3-based mesoscopic PSCs, as prepared (lemon), and aged under illumination (green) and in the dark (dark green), for 80 h @60% R.H. b) XRD diffraction patterns of as-prepared and degraded $FA_{0.71}MA_{0.29}PbI_{2.9}Br_{0.1}$ films deposited on Al_2O_3. SEM (SEI) top-images of ITO/Al_2O_3/perovskite: c) as-prepared, d) aged in the dark, e) aged under illumination.

The superior extraction efficiency of the mesoporous scaffold as compared to that of the compact film was demonstrated from the photoluminescence spectra shown in Fig. 4.9, in Chapter 4. The PL spectrum of $FA_{0.71}MA_{0.29}PbI_{2.9}Br_{0.1}$ deposited on an Al_2O_3 layer was also included, showing the reduced extraction capacity of this material.

In Figure 5.6, XRD diffractograms show the evolution of principal peaks of $FA_{0.71}MA_{0.29}PbI_{2.9}Br_{0.1}$ (110 at 13.9°) and PbI_2 (001 at 12.5°), and the evolution of the *J-V* curve after degradation for devices based on Al_2O_3, c-TiO_x, LT mp-TiO_2 and HT mp-TiO_2. The device based on Al_2O_3 presents strong decomposition of the perovskite material with high relative intensity of the principal peak of PbI_2 with respect to the principal peak of the perovskite material, and after 80 h of ageing the PV parameters are null. The device based on c-TiO_x presents low relative intensity of the PbI_2/perovskite XRD peaks, however, after 40 h of ageing the *J-V* curve show an increased shunt current which according to the observations might be related to the formation of PbI_2 crystals at the surface; after 80 h of ageing degradation is complete. The device based on LT mp-TiO_2 presents high relative intensity of the PbI_2/perovskite XRD peaks, interestingly, in this case, after 40 h of ageing, the series resistance is mostly affected which suggests a deficient contact at the ETL/perovskite interface; after 80 h degradation is not complete. The device based on HT mp-TiO_2 presents low decomposition, according to the relative intensity of the PbI_2/perovskite XRD peaks, series resistance seems slightly affected after 40 of ageing and, after 80 h this device retains a higher yield of the PV parameters as compared to the other configurations.

From the results, it can be hypothesized that despite chemical decomposition of the hybrid perovskite material in a PSC, a high yield of short-circuit current density might be

retained in devices using selective layers with enhanced electron extraction efficiency, as the LT mp-TiO_2 scaffold used in this study (Chapter 4, Fig 4.10). On the other hand, lower decomposition and increased PV performance is observed in the HT mp-TiO_2 based devices, which suggests that the better electronic properties of this mesoporous scaffold prevent the decomposition of the material. The latter result is in accordance with the work of Bryant *et al.*, in which a reduced decomposition after light and moisture of the perovskite material results from an enhanced electron extraction by the ETL (Bryant et al., 2016). The work is discussed in the Section 2.5B of the Chapter 2.

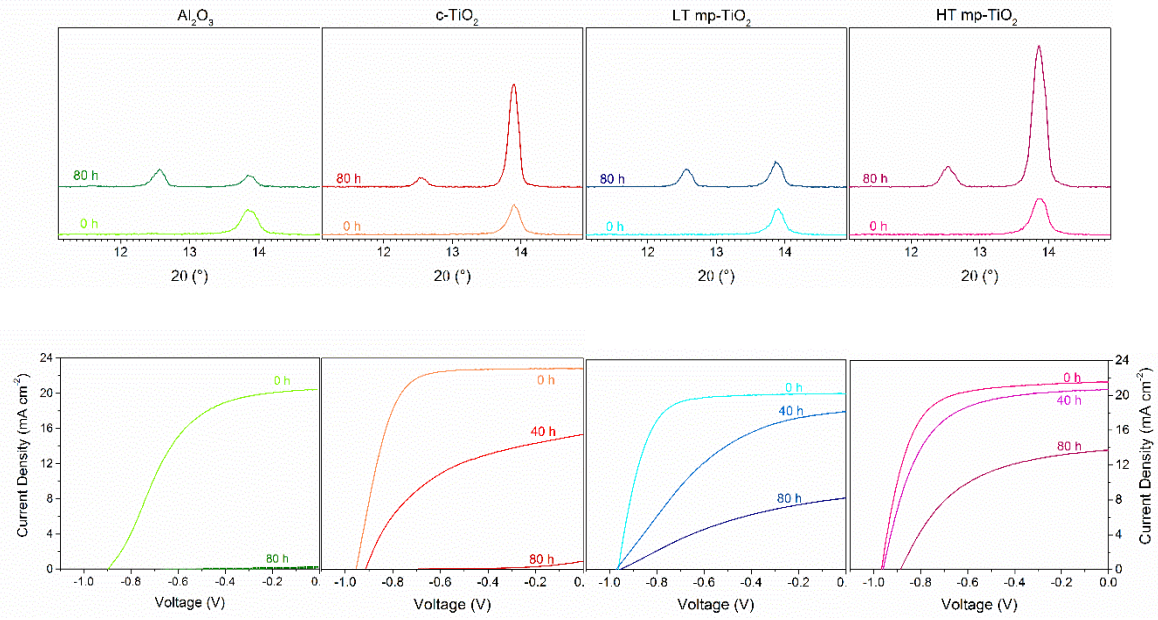

Figure 5.6. XRD diffraction patterns of as-prepared and degraded (80 h @60% R.H. & 0.2 sun AM 1.5G) $FA_{0.71}MA_{0.29}PbI_{2.9}Br_{0.1}$ perovskite deposited on Al_2O_3 (green), c-TiO_x (red), LT mp-TiO_2 (blue) and HT mp-TiO_2 (pink). *J-V* curves of TiO_2-based PSCs as prepared and aged under illumination for 40 h and 80 h @60% R.H. Note that the *J-V* curve of the alumina-based device after 40 h of ageing could not be measured.

5.1 Conclusions

A decrease in performance has been observed for PSCs exposed to both light and moisture; specifically, after ageing the J_{SC} is affected in devices with reduced electron extraction capacity of the ETL material. Comparing planar and LT mesoscopic PSCs chemical decomposition of the $FA_{0.71}MA_{0.29}PbI_{2.9}Br_{0.1}$ results somewhat stronger in LT mesoscopic PSCs, as seen from the relative intensity between the PbI_2 and the $FA_{0.71}MA_{0.29}PbI_{2.9}Br_{0.1}$ principal XRD peaks. However, despite the stronger chemical decomposition of the perovskite, LT mesoscopic devices retain higher percentage of its initial J_{SC}, i.e., 84% vs 58% in planar PSCs; resulting in T_{50} values of ~ 40 h and 20 h for LT mesoscopic and planar devices, respectively. The results suggest that the preserved performance in LT mesoscopic devices is due to superior electron extraction, which according to the continuity equation (Eq. 5.1) is at the origin of lower yield of charge recombination. On the other hand, we observed a prevented degradation of the perovskite material in HT mesoscopic PSCs in accordance with previous works relating high charge injection and precluded degradation (Bryant et al., 2016). Deterioration at the counter electrodes was observed for planar PSCs, which might be an indication of larger ionic mobility in this type of devices, as reported by other authors (Kato et al., 2015; Shlenskaya et al., 2018). Accordingly, a more pronounced hysteretic behavior was observed in planar PSCs, which has been related to ionic mobility (Calado et al., 2016; B. Chen et al., 2015; Jacobs et al., 2017; W. Tress et al., 2015; Yu et al., 2016). Our findings demonstrate the importance of including crystalline TiO_2 in LT TiO_2 based PSCs in order to improve the stability of the devices.

Acknowledgment

The author would like to thank Dora Huerta Quintanilla and Daniel Aguilar Treviño from LANNBIO at CINVESTAV-Mérida for their technical support and training in scanning electron microscopy and X-ray diffraction analysis.

CHAPTER 6

Insights into the Degradation of Planar and Mesoscopic PCSs through Impedance Spectroscopy Analysis

CHAPTER 6

Insights into the Degradation of Planar and Mesoscopic PCSs through Impedance Spectroscopy Analysis

Abstract

Impedance spectroscopy (IS) at the open-circuit potential (V_{OC}) was performed on partially degraded planar and LT mesoscopic perovskite solar cells (PSCs). The frequency-dependent response of the two configurations was compared. Two recombination mechanisms depending on the irradiation intensity were elucidated for the two types of PSCs: the Shockley Read Hall recombination mechanism dominates at low light intensities (< 10 mW cm^{-2}), whilst at higher light intensities the band-to-band recombination dominates. Furthermore, the recombination resistance was observed to be higher in mesoscopic PSCs in accordance with the higher V_{OC} observed in thus type of devices. On the other hand, a higher magnitude of the capacitive element in planar PSCs indicates larger charge density accumulated at the interfaces. An inductive loop is observed in mesoscopic PSCs, which suggests stabilization of ionic charges in these devices. The IS analysis along with the observations from the stability study were used to develop a model accounting for the delayed degradation in mesoscopic PSCs.

6.1 Introduction

In photovoltaics, impedance spectroscopy has been used to obtain information on the electrical characteristics of the devices. It is now widely employed for the characterization of PSCs and allows a more detailed understanding of some of the mechanisms governing the charge dynamics such as recombination resistance, geometric capacitance and ideality factors (Almora et al., 2018; Contreras-Bernal et al., 2019; Pockett et al., 2015). IS is applied to characterize full solar cells while they are being operated under technically relevant conditions, which makes this technique an interesting tool to study charge transport, transfer and recombination mechanisms. Among the most studied phenomena is the dependence of charge collection and recombination on the nature of the perovskite/transport layer interface (Contreras-Bernal et al., 2017; Correa-Baena et al., 2017; Pockett et al., 2015; Zarazua, Han, et al., 2016). Surprisingly, relatively limited research has been done on the degradation mechanisms in PSCs using IS analysis, which is a topic of utmost importance.

Guerrero *et al.* reported the energetic properties at the perovskite/cathode interface of ITO/PEDOT:PSS/Perovskite/PCBM/Metal solar cells before and after degradation (Guerrero, You, et al., 2016). They observed an additional resistance in the IS measurements of degraded devices, which was related with the extraction of carriers at the contact. According to the authors, poor extraction would result in the formation of an interfacial dipole due to the accumulation of photogenerated carriers producing the displacement of iodide atoms towards the interface, resulting in further degradation. Klotz *et al.* observed a reversible increase of the electrical resistance and a reduction of the capacitance with ageing time of PCSs (Klotz et al., 2019). They ascribed the observed behavior to a temporary reduction of the electronically active area caused by accumulation of charged ions at the

perovskite/transport layer interfaces. The ionic charges would act as recombination centers inhibiting charge carrier injection into the electrodes. Interestingly, both studies coincide in a degradation mechanism due to a reduced carrier extraction capacity in the presence of ionic charge accumulation at the interfaces.

In Chapter 5, the degradation of planar and LT mesoscopic PSCs after exposure to light and moisture was compared. Decomposition of the perovskite absorbing layer was observed in both type of devices, according to the XRD diffraction analysis. Nonetheless, LT mesoscopic PSCs retained 84% of its initial J_{SC}, as compared to 58% retained by planar PSCs (Table 5.1, Chapter 5). It was possible to conclude that the deterioration of the planar devices occurred due to a reduced charge extraction capacity of the electron transport layer (ETL), The conclusion was supported by an observed stronger degradation for PSCs containing a less conductive ETL, i.e., Al_2O_3. According to the J_{SC} continuity equation (Eq 5.1), the decrease of J_{SC} in aged planar devices would be originated by an increase in the recombination rate (R), either because of a reduced carrier lifetime or due to an increased excess carrier density, both causing a deficient carrier extraction efficiency at the interfaces.

Here, we employed IS to compare the electrical response between aged planar and LT mesoscopic TiO_2-based PSCs. We observed two domains of recombination depending on the irradiation value, for both types of devices. A charge transport mechanism related to accumulation at the interfaces dominates at high illumination intensities, with larger charge accumulation presented by planar devices. Additionally, an inductive loop is observed in mesoscopic PSCs, which suggests stabilization of ionic charges, therefore delaying ion-induced degradation.

6.2 Experimental

To cast light on the degradation mechanisms, IS was performed on partially degraded low temperature (LT) planar and mesoscopic PSCs, with PCE ≥ 10% for both configurations. The impedance response of three planar and three mesoscopic PSCs was investigated at the open-circuit potential (V_{OC}) using a Gamry electrochemical workstation. The V_{OC} was set by controlling the light intensity of a Xe-arc lamp with an AM 1.5G optical filter and a 10 cm water filter. Impedance measurements were performed at different illumination intensities: 0.5, 1, 3, 5, 10, 20, 40 and 100 mW cm^{-2}. The spectra were recorded from 10^5 Hz to 1 mHz, using an amplitude of 10 mV(rms). A protocol similar to the one reported by Pitarch-Tena *et al*. (Pitarch-Tena et al., 2018) was used to minimize the effect of degradation and pre-conditioning of the devices in the analyzed results, which consisted in monitoring the V_{OC} and the *J-V* curve before and after each recorded spectrum and, discharging the cell ($V_{applied}$ = 0) before starting to record each spectrum.

6.3 Results

In Chapter 5, it was shown that planar PSCs present faster degradation dynamics than mesoscopic PSCs under exposure to light and moisture. The PV performance of each device was tested before the IS measurement; Figure 6.1 shows representative *J-V* curves of the devices used for the IS analysis. As expected, the two configurations show differences due to their dissimilar response to light and moisture exposition; i.e. there is an important decrease in the photocurrent for planar PSCs accompanied by an increased hysteresis with HI values of 0.3 and 0.5 for LT mesoscopic and planar devices, respectively.

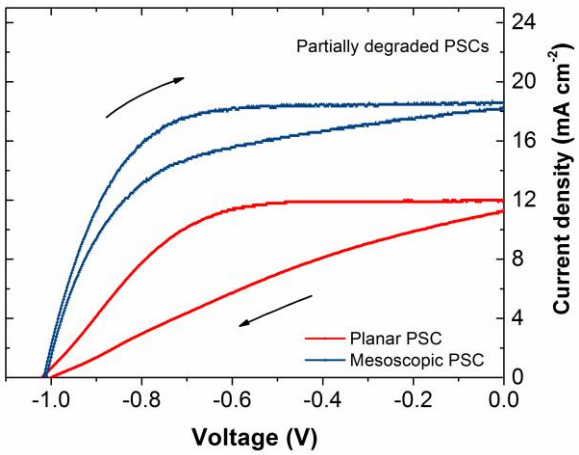

Figure 6.1. Representative current density – voltage curves of partially degraded planar and mesoscopic PSC used for the IS analysis; the scan rate is 0.05 V s^{-1}.

6.3.1 Ideality Factor from V_{OC} Measured at Different Light Intensities

The generated V_{OC} at the different illumination intensities: 0.5, 1, 3, 5, 10, 20, 40 and 100 mW cm^{-2} are shown in Figure 6.2a. The V_{OC} at 1 sun (100 mW cm^{-2}) is 1.02 and 1.07 V for planar and mesoscopic PSCs, respectively. The V_{OC} depends logarithmically on the light intensity (I), as expected from the diode equation:

$$eV_{OC} = E_g - n_{ID}k_BT\ ln\frac{I_0}{I} \tag{6.1}$$

where E_g is the bandgap of the absorbing material, e is the elementary charge, k_B is the Boltzmann constant, T is the absolute temperature, I_0 is a constant with the same units as I and n_{ID} is the so-called ideality factor. For a Schottky junction n_{ID} = 1 for recombination in a highly doped material (Wolfgang Tress et al., 2018), i.e. $N_D^+ = n \gg p$, generally observed in the quasi-neutral region, whereas n_{ID} around 1.4 to 2 is assigned to the Shockley-Read-Hall (SRH) recombination mechanism (Almora et al., 2018; Contreras-Bernal et al., 2017; Wolfgang Tress et al., 2018; Zarazua, Han, et al., 2016).

Interestingly, in this work two different behaviors of the V_{OC} are observed, depending on the illumination intensity. For low light intensity (< 10 mW cm^{-2}) n_{ID} = 1.3 - 1.4, while for high light intensity n_{ID} = 0.7. Values for n_{ID} < 1 due to surface recombination have been observed before, contrary to common belief (Wolfgang Tress et al., 2018). According to the results, the recombination is originated by the same mechanism in both type of cells, since both PSC configurations show the same values of n_{ID}. Nonetheless, in mesoscopic devices a higher V_{OC} is generated at the same light intensity, by a constant difference of about 0.05 V. According to Eq. 6.1, if n_{ID} is equal for both configurations E_g must be 0.05 eV larger in mesoscopic PSCs. In both types of devices, the absorbing material is identical, i.e., E_g is the same; thus the change in photovoltage must be produced by a more favorable position of the conduction band (CB) of the electron transport layer (ETL) with respect to that of the perovskite in LT mesoscopic devices, as compared to planar devices (C. Ding et al., 2018).

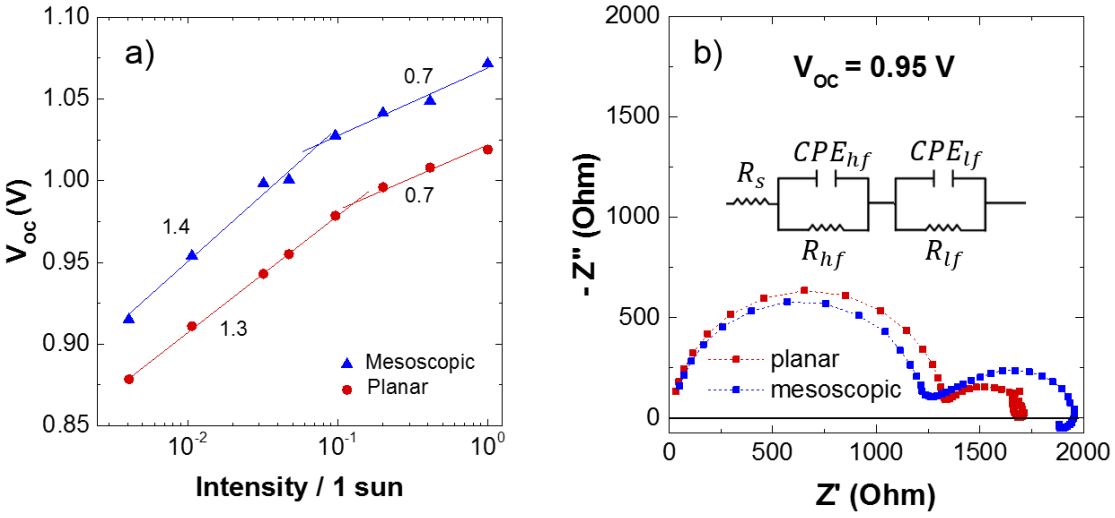

Figure 6.2 a) V_{OC} vs light intensity, lines show a logarithmic fit and the numbers indicate the n_{ID} obtained from the slope. b) Nyquist plots at V_{OC}=0.95 V. The equivalent electrical circuit is displayed in the inset.

6.3.2 Analysis of the electrical properties of PSCs using IS

Representative Nyquist plots of both types of devices at V_{OC} = 0.95 V are shown in Figure 6.2b. The impedance response is characterized by two semi-circles, one at high frequency (*hf*) from 10^3 to 10^5 Hz, and a second one at low frequency (*lf*) from 10^{-1} to 10^3 Hz. In addition, an inductive loop is observed in the very low frequency range (< 1 Hz). Interestingly, for mesoscopic PSCs the imaginary component crosses over to positive values. The impedance spectra were fit using the equivalent circuit shown in Figure 6.2b, comprising a resistance R_s in series with two Voigt elements. The capacitive elements were modeled as a constant phase element *CPE*, with $Z_{CPE} = 1/Q(j\omega)^P$, Eq. 3.11 in Chapter 3. The high frequency arc has a shape that is close to a semicircle with *P* ranging from 0.9 to 1, while for the low frequency arc, *P* is between 0.75 and 0.85. According to Brug *et al.*, in order to obtain a physically relevant interpretation of the capacitive response, the *P* value should be between 0.8 and 1 (Brug, van den Eeden, Sluyters-Rehbach, & Sluyters, 1984).

In Figure 6.3 the elements of the electrical analysis of the IS spectra are displayed as a function of the V_{OC} generated at different light intensities. In general, both R_{lf} and R_{hf} decrease exponentially as the V_{OC} increases (Figs 6.3a, b), as expected for a recombination resistance (Contreras-Bernal et al., 2017; Correa-Baena et al., 2017). The recombination resistance can be described by

$$R_{hf,lf} = \left(\frac{\partial J_{rec}}{\partial V}\right)^{-1} = R_{00} exp\left[-\frac{eV_{OC}}{n_{ID}\, k_B T}\right] \quad (6.2)$$

where J_{rec} is the recombination current density, R_{00} is the resistance at zero potential, and n_{ID} is the diode ideality factor. In contrast, the capacitive component shows different behaviour at high and low frequency. Figure 6.3c shows the capacitive element, CPE_{hf}, which is

generally ascribed to the bulk dielectric response of the perovskite layer (Almora et al., 2015; Guerrero, Garcia-Belmonte, et al., 2016), in accordance with its independent response with light intensity. On the other hand, CPE_{lf} is associated with charge accumulation processes at the interfaces, including ionic interactions at the surface (Almora et al., 2015; Contreras et al., 2016; Juarez-Perez et al., 2014). The *lf* capacitance has been described by the following expression (Almora et al., 2018)

$$C_{lf} = \frac{dQ}{dV} \propto exp\left[\frac{qV_{OC}}{\gamma\, k_B T}\right] \tag{6.2}$$

where Q is the charge per unit surface, and γ is an exponential coefficient that serves as a fitting parameter. The time constant (τ) is the characteristic time associated to the process and is obtained from the product *RC* according to Eq. 3.14 (Fig. 6.3d). However, specifically in the *hf* domain, it cannot be properly considered as a carrier lifetime since the nature of the CPE is dielectric and not chemical (Pockett et al., 2017; Zarazua, Han, et al., 2016).

In detail, R_{hf} yields two different values of n_{ID} consistent with the behaviour observed in the dependence of V_{OC} with light intensity: $n_{ID} \sim 2$ for SRH recombination at intensity < 10 mW cm^{-2} and $n_{ID} \leq 1$ for high light intensity. In addition, R_{lf} for planar PSCs displays n_{ID} = 1.3 with no apparent dependence on light intensity, which is also in the regime of a SRH recombination (Almora et al., 2018). On the other hand, for mesoscopic PSCs in the *lf* domain n_{ID} is dependent on light intensity with n_{ID} = 1.6 and 0.9, in accordance with the two recombination mechanisms so far observed. The magnitude of the resistive elements in the *hf* domain is similar for both types of devices at low light intensity values, while it is one order of magnitude larger for LT mesoscopic devices at high light intensity, evident at V∼1.02 V. In the *lf* domain it is again very similar for all light intensities.

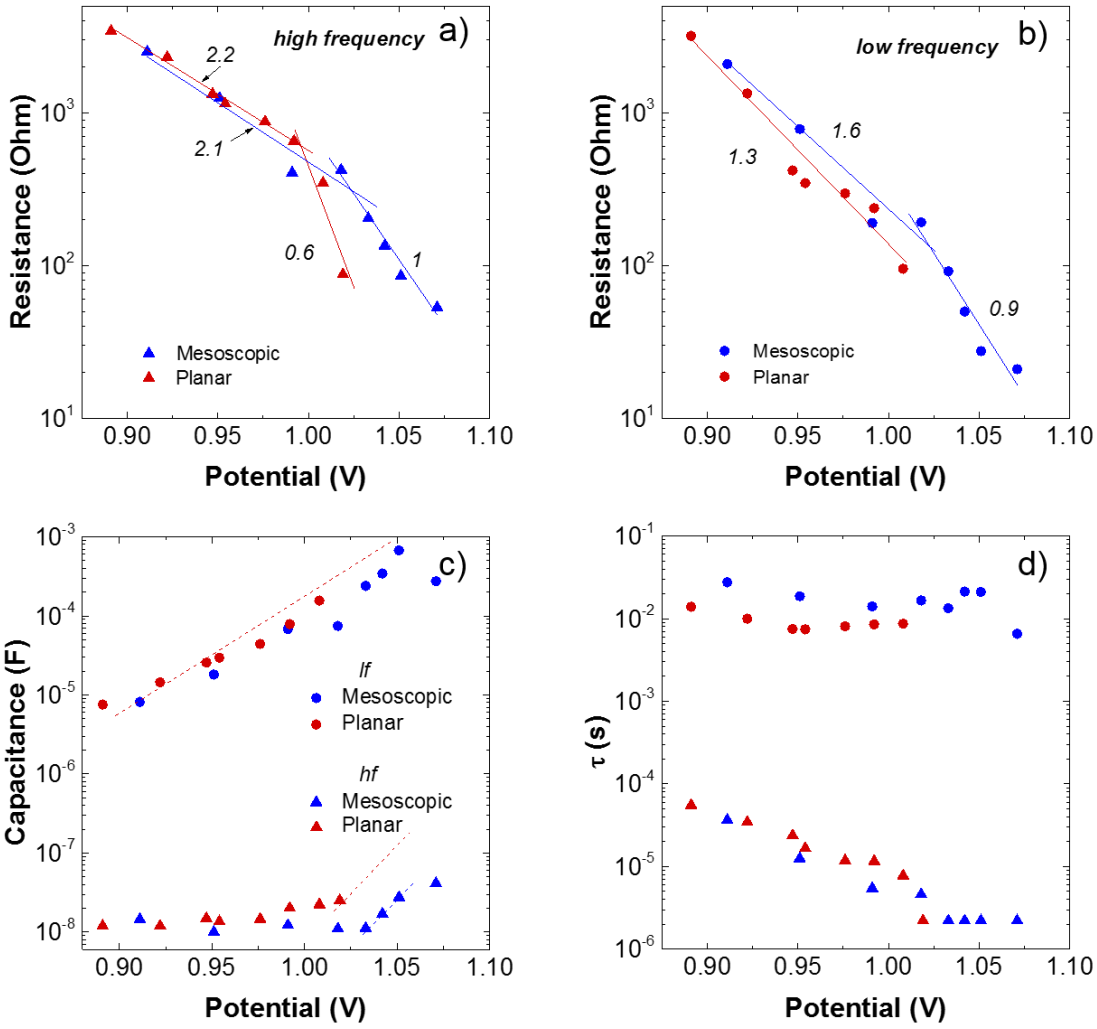

Figure 6.3 IS electrical elements obtained from the equivalent circuit of aged planar and mesoscopic PSCs. a) and b) Resistive elements obtained in the high and low frequency domains, respectively. c) and d) Capacitive elements and time constant (τ). The lines correspond to logarithmic fits and the numbers indicate n_{ID} deduced from the slope.

The CPE_{lf} exhibits an exponential increase with V_{OC}, which has been ascribed to charge accumulation at the interfaces (Almora, Guerrero, & Garcia-Belmonte, 2016; Correa-Baena et al., 2017; Zarazua, Bisquert, et al., 2016). Interestingly, CPE_{hf} changes from being linear to an exponential behavior for light intensities > 10 mW cm^{-2}, indicating that at high

light intensity a process related to charge accumulation at the interfaces dominates. In addition, the capacitive element of planar devices appears larger at high irradiation intensities: in the *hf* domain the tendency line indicates larger capacitance. These results are a strong indication of charge accumulation at the interface that is more pronounced in planar PSCs at high light intensity.

The time constant τ is found to be independent of the light intensity in the *hf* regime at high light intensity, which is consistent with charge accumulating at the interface. According to Zarazúa *et al.,* a τ independent of the light intensity would contain information of surface recombination processes occurring and not from the bulk, since bulk carrier density is dependent on light intensity (Zarazua, Han, et al., 2016).

The ideality factor is a parameter that characterizes the predominant recombination process, nonetheless its interpretation might vary according to the specific characteristics of the device (Wolfgang Tress et al., 2018). According to Tress *et al.,* a n_{ID} value close to 1 can be attributed either to surface recombination via intragap defects in devices displaying low V_{OC}, or to band to band recombination if the V_{OC} is high. The devices studied in this work displayed $V_{OC} > 1$ V with 1 sun illumination, which is considered high photovoltage. Thus, it is possible to think that at high illumination intensities the SRH recombination is suppressed and the band to band recombination dominates. The latter would be explained by trap filling due to a higher population of minority carriers at the ETL/perovskite interface (Péan, De Castro, & Davies, 2019).

6.3.3 Inductive Loops in the Impedance Spectra of PSCs

An additional observation in the IS spectra of both planar and mesoscopic PSCs is the appearance of an inductive loop at the end of the low-frequency arc (< 1 Hz). In Figure 6.4, these features are highlighted. Inductive loops in the mid-frequency range are familiar features in PSCs; possible explanations include carrier accumulation at the interfaces, injection through intermediate surface states, ion/vacancy drift and accumulation, and electrochemical reactions (El Kamel, Gonon, Jomni, & Yangui, 2008; Ghahremanirad et al., 2017; Guerrero, Garcia-Belmonte, et al., 2016; Zohar et al., 2016). In figure 6.4, for mesoscopic PSCs the imaginary part crosses over to positive values, indicating that the current in the device exhibits a delay with respect to the driving voltage, while for the planar configuration the imaginary part of the impedance remains negative. Ghahremanirad *et al*. have proposed that a shift of the imaginary part to positive values occurs when a kinetic relaxation constant related to a slow buildup of ionic charge increases (Ghahremanirad et al., 2017).

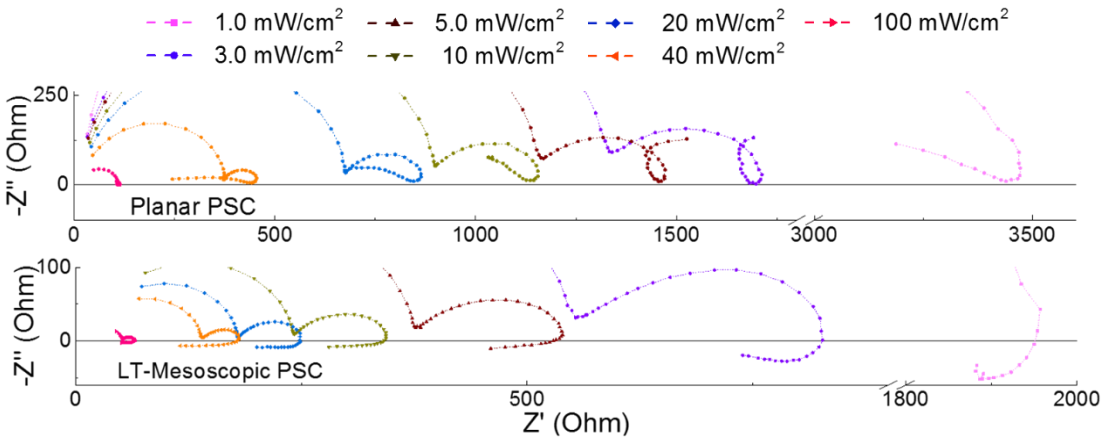

Figure 6.4 Zoom of the low frequency region of Nyquist plots measured under open-circuit conditions at different irradiation values for planar and mesoscopic PSCs, highlighting the inductive-loop features.

The results of the IS analysis can be summarized as follows:

- The V_{OC} vs light intensity measurements revealed that the difference in photovoltage (~ 0.05 V) is the result of a more favorable position of the CB of the mp-TiO_2 scaffold with respect to that of the perovskite in mesoscopic devices, as compared to planar devices.
- Two different recombination mechanisms are observed depending on the light intensity: at irradiance < 10 mW cm^{-2} the SRH recombination seems to dominate, with n_{ID} ~ 2, and at irradiance > 10 mW cm^{-2} trap-filling would allow band-to-band recombination to dominate, with $n_{ID} \leq 1$.
- Lower recombination processes are observed in mesoscopic PSCs, supported by the larger magnitude of the R_{hf} at high light intensity and larger values of τ_{lf}, pointing to better electronic properties of the mp-TiO_2 scaffold.
- Larger charge accumulation at the interfaces appears to occur in planar PSCs. In addition, the CPE_{hf}, which is generally ascribed to the bulk dielectric response of the perovskite layer, changes from being linear to an exponential behavior for light intensities > 10 mW cm^{-2}, indicating that under high irradiation a process related to charge accumulation at the interfaces dominates in both types of devices.
- The inductive loop in mesoscopic PSCs is associated to a negative capacitance which origin is not clear. However, due to the frequency dependence of IS, it is reasonable to think that in mesoscopic devices the charges move at slower speed, possibly due to a different electrostatic environment at the nanostructured mp-TiO_2 as compared to the compact surface in planar PSCs.

6.3.4 Model of the Mechanism of Retarded Degradation in Mesoscopic PSCs

Based on the IS analysis and the observations from the stability study experiments, a mechanism accounting for the slower degradation dynamics in LT mesoscopic PSCs as compared to planar PSCs is proposed (Fig. 6.5):

i. A build-up of charge at high light intensities (> 10 mW cm^{-2}) is accumulated at the compact-TiO_2 electrode surface in planar PSCs accompanied by a more pronounced hysteretic behavior. This latter can be attributed to ionic charges accumulating at the surface inducing the observed electrode degradation in this type of devices.

ii. In the presence of a nanostructured TiO_2 films an electric field is generated across the perovskite film, providing beneficial conditions for the stabilization of harmful ionic charges far enough from the interface to delay degradation in LT mesoscopic PSCs, as suggested from the inductive loop observed in the spectra of these devices.

iii. In LT mesoscopic PSCs the mp-TiO_2 ETL provide the device with higher recombination resistance due to its better electronic properties and more favorable CB alignment. This would account for the higher V_{OC} observed and higher J_{SC} retention after degradation of the perovskite material.

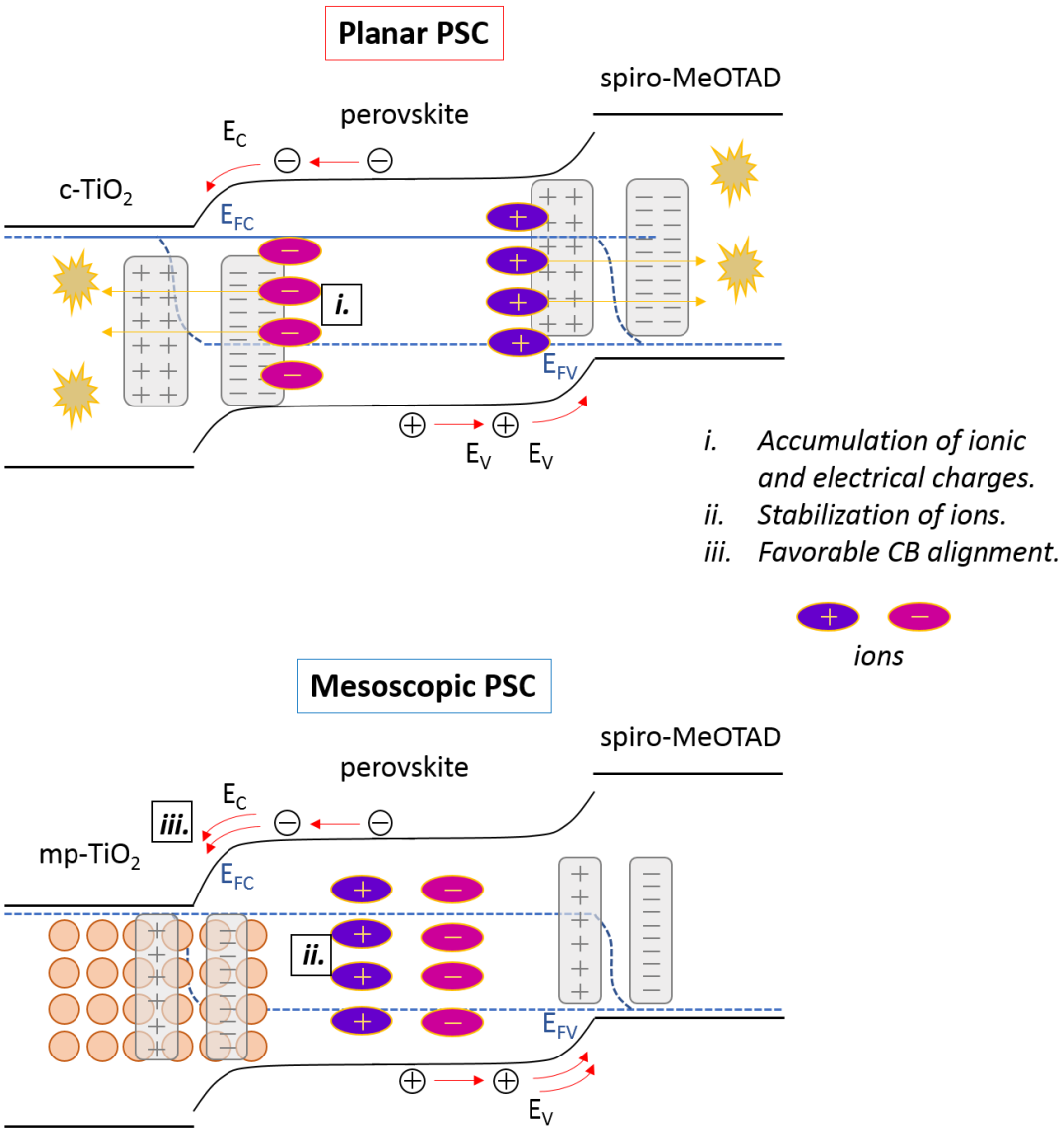

Figure 6.5. Schematic band diagram illustrating the proposed mechanism for delayed degradation in mesoscopic PSCs as compared to planar PSCs. The quasi Fermi levels splitting and the beneficial electrostatic ambient at the mp-TiO_2/perovskite interface are depicted. Boosting of the charge extraction and delayed degradation would result from such conditions.

6.4 Conclusions

In general, the IS response of planar and mesoscopic PSCs present differences. At low light intensities (< 10 mW cm^{-2}) the charge carrier dynamics are mainly determined mainly by SRH recombination in the bulk of the perovskite. On the other hand, at high light intensities (> 10 mW cm^{-2}) the SRH mechanism would be disabled by trap-filling, giving place to domination of the band-to-band recombination mechanism. The larger magnitude of the capacitive element of planar PSCs indicate a more pronounced charge accumulation in these types of devices; it is likely to think that this charge is of ionic nature due to the observation of a pronounced hysteretic behavior in this type of devices. In contrast, the inductive loop in the spectra of mesoscopic PSCs suggests that the generated electric field across the perovskite film in this type of devices slows down the ion-related degradation through the stabilization of the ionic species far from the interface. Finally, it became clear that the better electronic properties of the mp-TiO_2 scaffold would be at the origin of the higher photovoltaic performance retention observed in mesoscopic PSCs.

Acknowledgement

The author would like to thank Dr. Juan Antonio Anta, Dr. Jesús Idígoras, Dr. Rodrigo Rodríguez García and Dr. Isaac Zarazúa for the valuable discussions about this topic.

CHAPTER 7

Fabrication Method of PSCs under Controlled Atmosphere

CHAPTER 7

Fabrication Method of PSCs under Controlled Atmosphere

Abstract

The procedure to fabricate perovskite solar cells (PSCs) have demonstrated to be highly sensitive to the specific laboratory conditions. Three specific processes were identified as source of changes in the atmosphere composition during perovskite crystallization: i) spin coating conditions, ii) annealing process and iii) anti-solvent treatment. The optimization course to achieve proper processing conditions of mesoscopic perovskite solar cells under controlled atmosphere is presented. Mesoscopic PSCs with $FA_{0.71}MA_{0.29}PbI_{2.9}Br_{0.1}$ perovskite as absorber layer where successfully fabricated at Cinvestav-Mérida with a record PCE of 15.5 %. Additionally, the insertion of certain carbon-allotropes into PSCs is reported.

7.1 Introduction

In 2009, methylammonium lead iodide, a member of the hybrid organic-inorganic lead halide perovskite family best known as $MAPbI_3$ was first used as the light absorbing material in a solar cell (Kojima et al., 2009). Since then, the remarkable physical properties of this type of materials have gained interest for optoelectronic and photovoltaic applications. For instance, $MAPbI_3$ has a high optical absorption coefficient of $\alpha \sim 1.5 \times 10^4$ cm^{-1} at 550 nm, long diffusion length of $L > 100$ nm, and exciton binding energy in the range 14-25 meV

(Galkowski et al., 2016; Park et al., 2016). Such advantageous properties make the hybrid halide perovskite an attractive candidate for the development of highly efficient solar cells. Consequently, a significant number of research groups in the materials field have studied this family of semiconductors in the recent years.

The most common method to obtain hybrid organic-inorganic lead halide perovskites is based on a simple wet chemical process (Burschka et al., 2013; M. M. Lee et al., 2012). Nonetheless, the crystallization dynamics of the hybrid halide perovskite are highly sensitive to the processing atmosphere (Pathak et al., 2015; Sheikh et al., 2015), adding challenge to the manufacture. Typical issues to the fabrication include incomplete conversion (C. Jiang, Lim, Goh, Wei, & Zhang, 2015), defect formation (Fedeli et al., 2015), poor crystallinity (Cohen & Etgar, 2016) and phase segregation (Patel, Milot, Wright, Herz, & Johnston, 2016). All these defects directly affect the optoelectronic properties of the perovskite and the device performance, making it necessary to design a strategy to control the crystallization. Furthermore, highly controlled processes to deposit the selective conductive materials and enhance the electrical contacts are also crucial for optimizing the device performance.

In this chapter, the optimization process to obtain high-quality hybrid halide perovskite films with final estimated composition $FA_{0.71}MA_{0.29}PbI_{2.9}Br_{0.1}$ is presented. In addition, optimization of the fabrication methods of the blocking and mesoporous layers are also described. Please refer to Chapter 3 for a full description of the complete device structure and functioning. At the end of the chapter, the photovoltaic characteristics of PSCs in the course of the optimization process are presented, demonstrating the reliability of the study. The methodology to insert carbon-allotropes in PSCs is presented along with degradation and photovoltaic tests.

7.2 Optimization of PSCs

7.2.1 Blocking Layer Fabrication

The blocking layer (BL) constitutes an energetically favorable path for the photo-generated electrons, preventing recombination and enhancing charge collection at the contacts. TiO_2 has been the most widely used material since it provides a correct band alignment with the hybrid halide perovskite active layer and its synthesis is quite standardized (Mahmood et al., 2017). In order to obtain a good BL, the fabrication method should guarantee a pin-hole free and conformal layer, with the minimum thickness possible to ensure collection. The ideal thickness reported for a TiO_2 BL varies between 30 to 60 nm (Gouda et al., 2017). In this work, TiO_2 blocking layers were fabricated following two different methods: atomic layer deposition (ALD) and spray pyrolysis (SP).

A Atomic Layer Deposition

Atomic layer deposition of TiO_2 from tetrakis(dimethylamino)titanium (TDMAT) and water was performed using a recipe provided by the equipment vendor Savannah, the experimental details are addressed in Section 3.1.2 in Chapter 3. The number of cycles and a post thermal treatment were adjusted to obtain conformal films.

SEM images of the FTO and a 50 nm-thick TiO_2 blocking layer fabricated by ALD on FTO substrates are shown in Fig. 7.1 The profile image shows that the TiO_2 grows following very tightly the topography of the FTO grains (Fig 7.1b), as expected from the working principle of the technique. On the other hand, the top-view image shows that the grain boundaries of the FTO remain very well defined, which indicates weak interconnection in the as-prepared film (Fig7.1c). It was found that a post thermal treatment at 500 °C was required to sinter the material, resulting in good interconnection. The optimum BL thickness

prepared by ALD was found to be 60 nm achieved with 900 cycles (growth rate of ~ 0.66 Å/cycle).

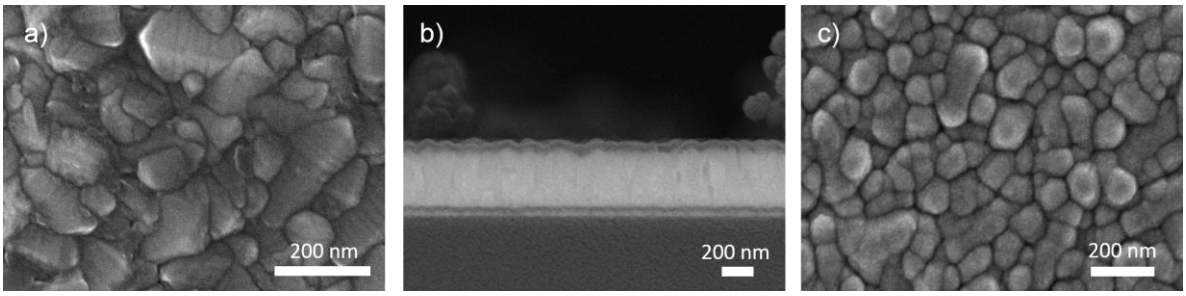

Figure 7.1. SEM (LABE: low angle back scattering) micrographies of: a) top view of glass/FTO, and b) cross section and c) top view of glass/FTO/c-TiO_2 deposited with ALD.

B Spray Pyrolysis

TiO_2 blocking layers were obtained using a solution of titanium diisopropoxide bis(acetylacetonate) in isopropanol at a concentration of 4% v/v and the pyrolysis was performed at 350 °C, according to the recipe reported by Watson *et al.* (Charbonneau et al., 2016). Nonetheless, in the SP technique, the central task is to achieve reproducibility. When the technique is implemented manually, as in this case, reproducibility relies on controlling: a) the position of the spray nozzle relative to the substrate, b) pulverization of the liquid into droplets, and c) time lapses between deposition cycles. Proper separation from the substrate prevents undesired solvent evaporation and contributes to the uniformity of the deposition. On the other hand, moderated pulverization and spraying velocity prevents agglomerations and allows the material to arrange neatly, favoring a better coverage of the substrate topography. In addition, the thickness of the film is controlled by the volume of precursor solution per covered area. In Fig. 7.2a a picture of the SP experimental arrangement is presented. The distance between the spray nozzle and the substrate was set to 40 cm making an angle of 60° with the surface of the substrate. The air manometric pressure was set to 0.2

MPa. The velocity with which the spray gun was moved to scan the substrate area was set to 0.01 m/s. A volume of 25 mL of the precursor solution was used to cover 20 FTO substrates with an area of 2 x 2 cm^2. SEM images of a compact TiO_2 film fabricated by SP are presented in Figs. 7.2b, c. The profile image (Fig 7.2b) shows a TiO_2 film of homogeneous thickness of 60 nm. The top-view (Fig 7.2c) reveals uniform coverage of the FTO grains as compared to the ALD films, indicating good interconnection within the film. On the other hand, a typical defect found on these films is also observed (upper left corner), which might be related to an unexpected droplet in the pulverized solution.

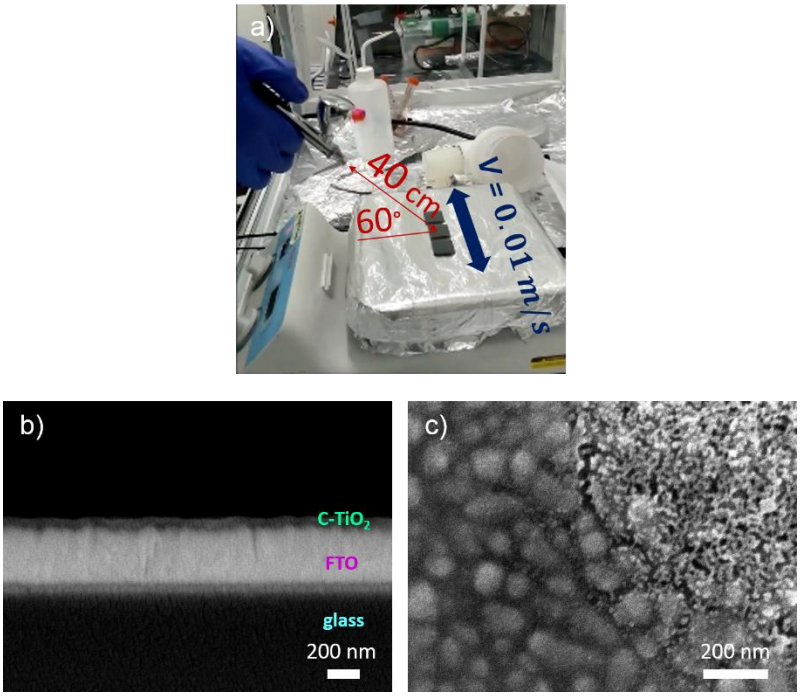

Figure 7.2. a) Picture of the manual spray pyrolysis arrange with distance and velocity indicated. SEM (LABE) b) cross section and c) top view micrographies of a 60 nm-thick TiO_2 blocking layer deposited with SP. FTO was used as substrate.

7.2.2 Blocking Layer Characterization

Electrochemical experiments were performed to evaluate the electrical rectifying characteristics of the TiO_2 films deposited by either ALD or SP. TiO_2 films deposited on FTO were used as working electrodes in a solid-liquid cell, using a cobalt (II/III) redox couple as electrolyte and a thin film of platinum as counter electrode. The blocking function of the TiO_2 layer, which is an n-type semiconductor, prevents the flow of an anodic current corresponding to oxidation of the redox couple. Fig. 7.3 shows a cyclic voltammetry of solid-liquid cells containing three different working electrodes: bare FTO (dotted line), FTO/ALD-TiO_2 (purple line) and FTO/SP-TiO_2 (blue line). At the bare FTO two pronounced peaks are observed, one at 0.24 V corresponding to the anodic current due to oxidation of the cobalt II to cobalt III at the FTO surface, and another at 0.14 V corresponding to the reduction of cobalt III to cobalt II; quality compact layers are expected to reduce the anodic current.

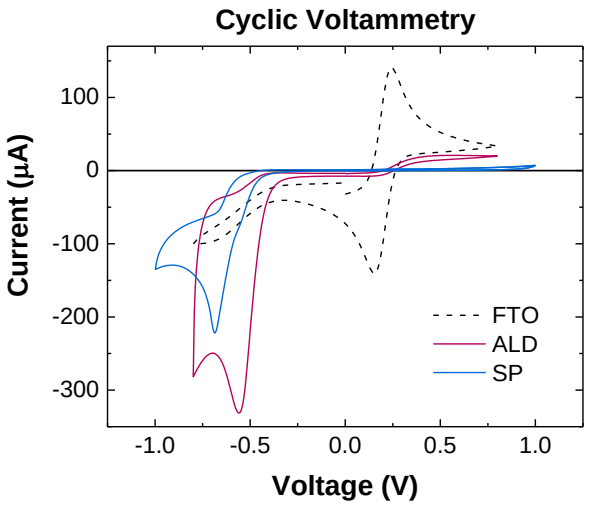

Figure 7.3. Cyclic voltammetry of the ferri/ferro-cyanide system using three different working electrodes: FTO (dotted line), FTO/ALD-TiO_2 (purple) and FTO/SP-TiO_2 (blue); an Ag/AgCl electrode was used as reference electrode.

The ALD-TiO_2 blocking layer reduces the anodic current two orders of magnitude, whilst the SP-TiO_2 blocking layer reduces it four orders of magnitude. The results show that both techniques produce high quality BL capable of rectifying the current. The TiO_2 BL also affects the reduction current shifting the peak to more negative potentials, which indicates that the kinetics of electron transfer to the solution at the TiO_2 film are slower than at FTO.

7.2.3 Mesoporous Layer

In PSCs, the mesoporous (mp) layer is a noteworthy component. It has been demonstrated that its insertion is not needed to achieve highly efficient devices (Heo, Song, & Im, 2014), yet important improvements have been reported in: a) reproducibility and b) stability (Eperon, Burlakov, Docampo, Goriely, & Snaith, 2014; J. Yang et al., 2016). A high-quality mesoporous layer should present good porosity and surface coverage, homogeneous layer thickness, and excellent electrical properties. In the present work, we focus on the use of TiO_2 anatase nanoparticles (NPs), a material that has been widely used in the n-i-p mesoscopic PSC configuration (Mahmood et al., 2017). One of the novelties of this work is the low-temperature fabrication of the mesoporous layer with appropriate electrical conductivity from a NP dispersion (Castro-Chong et al., 2020). The optimization process for the implementation of a low-temperature mesoporous layer is presented in Chapter 4.

7.2.4 Photoactive Layer

In order to take advantage of the optoelectronic properties of the hybrid lead halide perovskite, well-crystallized and pinhole-free films must be obtained. Reproducibly fabricating perovskite solar cells is quite challenging. Solution processing of perovskite thin

films is characterized by a nucleation process that is very sensitive to the precise conditions, which leads to poor crystallization control. For instance, the atmosphere significantly affects the perovskite film formation, as was observed in this work and reported elsewhere (J. Chen et al., 2017). Several parameters of the fabrication process influence chemical conversion, crystallization and defect formation; hence, careful design of the process is needed. In this work, three main aspects were identified: i) spin coating conditions, ii) annealing process, and iii) anti-solvent treatment.

i Spin Coating Conditions

One major criterion to evaluate the quality of the hybrid halide perovskite film is the complete conversion of the precursors into perovskite, which depends strongly on the fabrication method. Here, the two-step spin coating method, is adopted in combination with the intramolecular exchange process (IEP) (W. S. Yang et al., 2015). The method is detailed in Section 2.2 in Chapter 2. The IEP facilitates the incorporation of the organic halides into the Pb-I lattice and promotes the conversion to perovskite. Nonetheless, the deposition conditions need to be optimized.

We departed from the two-step spin coating recipe reported by Qiu et al. (Qiu et al., 2017). Two standard solutions were prepared:

- Solution A consisted of 1.25 M PbI_2 in a mixture of n,n-dimethyl formamide and dimethyl sulfoxide (DMF/DMSO: 90/10, v/v).
- Solution B consisted of $CH(NH_2)_2I$ (FAI), CH_3NH_3I (MAI) and CH_3NH_3Br (MABr) (71:19:10 molar ratio) in isopropanol.

Fig. 7.4 shows the X-ray diffractogram (XRD) of the obtained hybrid halide perovskite. Along with the perovskite corresponding peaks, the principal peaks of the PbI_2: (001), (002) and (003) are observed, which indicates incomplete conversion. The conversion process requires the replacement of DMSO molecules by the external organic halides during the second spin coating step; at this point the dynamic forces promote the interdiffusion while at the same time the solvent evaporates. An incomplete conversion might be caused by an excessive spinning speed that reduces the mobility of the species by a rapid evaporation, Figure 7.4 (green line). Thus, the spin coating speed was reduced from 3000 rpm to 2000 rpm. The XRD of hybrid halide perovskite with reduced spinning speed show that the strategy leads to complete conversion of the hybrid halide perovskite, Figure 7.4 (blue line). The latter is in agreement with previous reports that show that slow solvent evaporation favors the crystallization process (J. Chen et al., 2017).

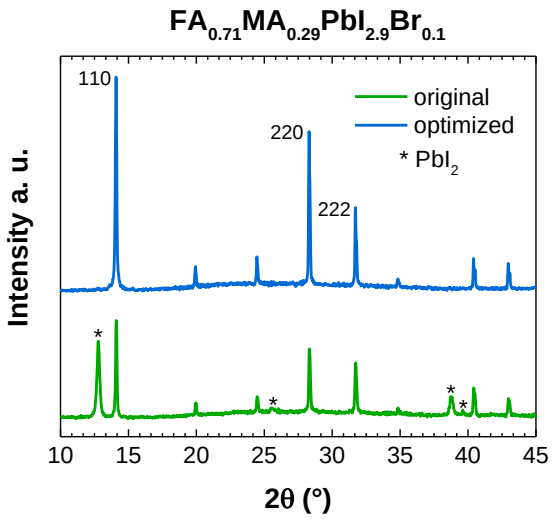

Figure 7.4. X-ray diffractograms of the mixed lead halide perovskite films: original recipe (light blue) and optimized recipe (blue). The main peaks of the perovskite material are assigned, the asterisks (*) indicate the PbI_2 peaks.

ii Annealing Process

Poor morphological control and bad surface coverage is known to induce efficiency variations in PSCs. Attempts to reduce pinholes and improve the grain morphology of the perovskite film have been mostly focused on solvent and precursor engineering (Gardner et al., 2016; Ye et al., 2018). However, a significant influence of the processing atmosphere on crystallization and grain size of hybrid halide perovskites has been observed.

Pathak *et al.* found that large grain domains were obtained when the annealing process of the perovskite films was performed in air rather than in nitrogen (Pathak et al., 2015). Interestingly, perovskite dissolves readily in H_2O. Investigations show that moisture promotes perovskite crystallization by conferring mobility to the ionic salts (Patel et al., 2016). However, under ambient conditions, a delicate control of the moisture level in the atmosphere is required since H_2O is a highly polar molecule which can incorporate into the PbI_2 : MAI complex (Aranda et al., 2017). Hence, the synthesis process is preferably performed under inert atmosphere to lower the moisture and oxygen content.

From the observations explained above it is possible to think that the availability of any high polar molecule in the surrounding atmosphere during perovskite crystallization can improve the film quality. Here, slow evaporation of the solvents is proposed to favor the crystal growth under a moisture-free atmosphere. The procedure consists in a retarded annealing process to enhance the solvent availability during crystallization. Originally, the films were annealed for 30 minutes at 100 °C inside the glovebox under nitrogen atmosphere. A novel treatment to slow evaporation consisted in annealing for 15 minutes at 70 °C followed by 30 minutes at 100 °C, performed inside the glovebox.

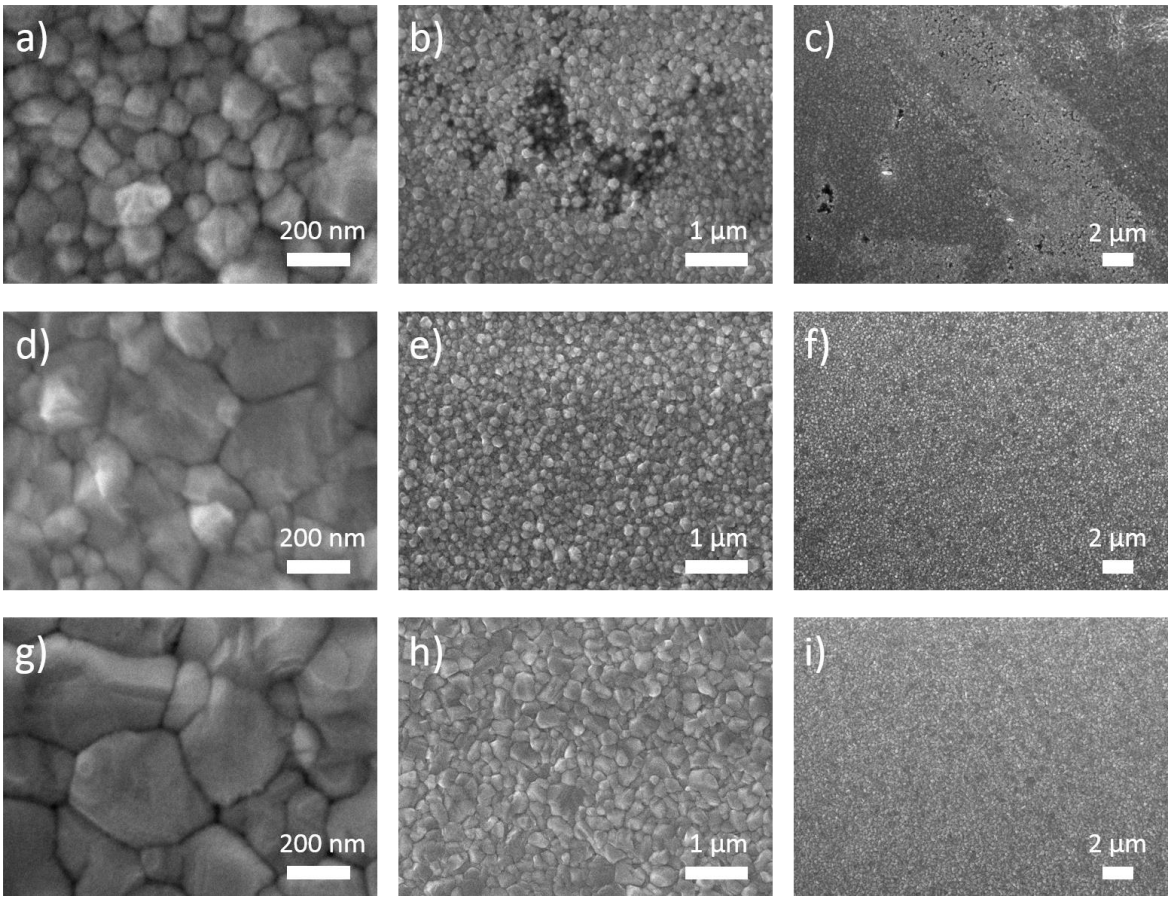

Figure 7.5. SEM (SEI) images of $FA_{0.71}MA_{0.29}PbI_{2.9}Br_{0.1}$ films with different annealing treatments. (a-c) Fast evaporation inside the glovebox: 30 min @100 °C in N_2, (d-f) Slow evaporation inside the glovebox: 15 min @70 °C + 30 min @100 °C in N_2, and (g-i) Fast evaporation in air: 30 min @100 °C with 30% R.H.

SEM images of $FA_{0.71}MA_{0.29}PbI_{2.9}Br_{0.1}$ films with the different annealing treatments are shown in Fig. 7.5. For comparison, images corresponding to annealing treatment of 30 minutes at 100 °C under air with 30 % R.H. are also shown. Upon fast crystallization inside the glovebox small perovskite grains with diameter of ~ 100 nm are observed and the film present holes in the order of microns. The slow evaporation treatment inside the glovebox allows the formation of larger grains with diameter of ~ 300 nm, and pinhole-free films are observed. In comparison, larger grains with diameter of ~ 500 nm and pinhole-free films are

obtained upon fast crystallization in air. The effect of the annealing atmosphere on the quality of the films is evident. The results confirm that the slow solvent evaporation process fosters the grain growth and is an appropriate strategy to obtain pin-hole free perovskite films under a controlled, moisture-free atmosphere. In addition, the good quality of the perovskite films obtained in air indicates the importance of the solvent availability in the atmosphere during crystallization.

iii Anti-solvent Treatment

A common observation when processing perovskite thin films is a difference in color from one sample to another within the same batch (same precursor solutions and apparent atmosphere conditions). The latter is representative of incomplete conversion: dark brown to dark orange films are obtained, which turn into orange pale within a minute. It was observed that this evolution in the composition of the films is related to a change in the atmosphere throughout the film processing. Specifically, during the spin coating step DMSO and DMF evaporate, increasing their concentration in the working atmosphere. When this concentration is too high, film formation is affected by the organic content in the atmosphere, and the crystallization of the perovskite phase is hindered. Here, we implemented the anti-solvent treatment as a strategy to modify the atmosphere content and impede the re-dissolution of the perovskite by solvent vapors. The anti-solvent treatment consists in dripping a non-polar solvent during the spin coating process to induce controlled crystallization (Jeon et al., 2014). The technique is mostly focused on the removal of solvents from the film; here, we extend this method as a purification process of the atmosphere. The difference relies on the volume of anti-solvent used, 500 µl of toluene are poured as compared to 20 µl reported by Kara *et al.* (Kara et al., 2016). After the implementation of the modified anti-solvent treatment no difference in color was observed among different samples.

7.2.5 Photovoltaic and Optoelectronic Properties

In Figure 7.6 the improvement in the performance of the perovskite solar cells during the optimization period is depicted. The PV parameters of PSCs after optimization of three different parameters of the photoactive layer: i) spin-coating conditions (Dec 2018), ii) annealing process (Feb 2019) and iii) anti-solvent treatment (Sep 2019), are shown. An increment in the average PCE from 5 to 12% was achieved, demonstrating the successful optimization of the fabrication process.

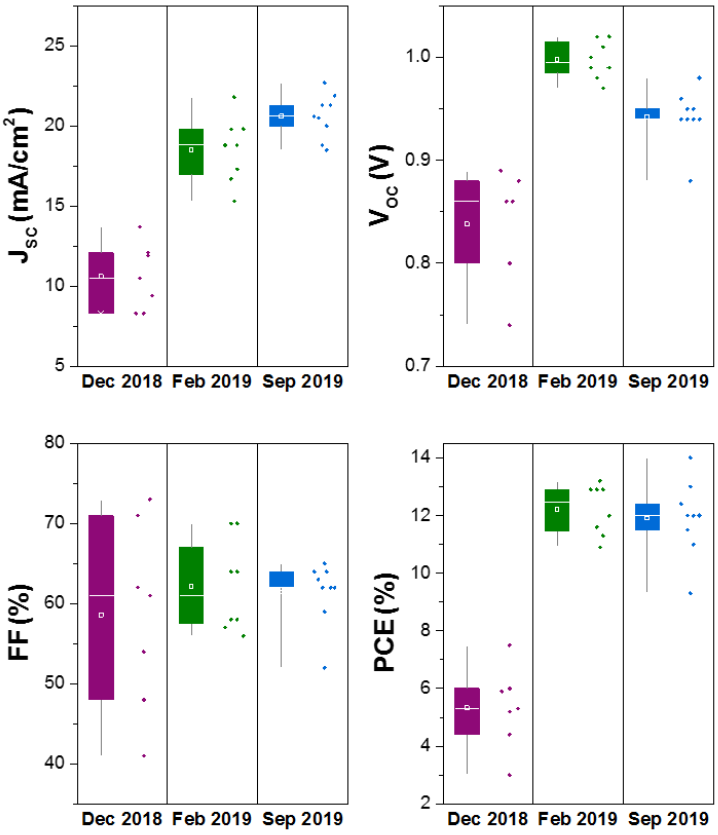

Figure 7.6. The photovoltaic parameters: short-circuit current (J_{SC}), open-circuit voltage (V_{OC}), fill factor (*FF*) and power conversion efficiency (*PCE*) of three batches of PSCs fabricated on different dates: December 2018 (purple), February 2019 (green) and September 2019 (blue).

Through optimization of the spin-coating conditions, functional devices were obtained depicted by an average PCE of ~ 5%. After implementing the slow annealing and anti-solvent treatments the average PCE was increased to 12%, due to an increment in V_{OC} and J_{SC}, in accordance with the obtention of pinhole-free films.

The optoelectronic properties of the $FA_{0.71}MA_{0.29}PbI_{2.9}Br_{0.1}$ perovskite obtained in this work have been characterized. The absorptance spectrum shows an onset of the absorption at 790 nm and a maximum absorption at 550 nm (Fig. 7.7a), in accordance with previous reports of similar perovskites (Jesper Jacobsson et al., 2016). A band gap of 1.57 eV was calculated using the Kubelka-Munk method. It has been demonstrated before that replacing the iodide with a larger ion would cause a change in the lattice parameters and thus result in a change in the band gap (Filip, Eperon, Snaith, & Giustino, 2014).

Steady-state photoluminescence (PL) spectroscopy has been used to characterize the perovskite films deposited on glass. One distinct PL-peak centered at the band gap energy is observed, which corresponds to direct recombination from the conduction band edge to the valence band edge, as shown in Fig. 7.7b. The external quantum efficiency (EQE) has been measured as a function of wavelength and shown for a high-performing PCE in Fig. 7.7c. The integrated current (green line) results in a lower J_{SC} than the one extracted from the *J-V* curve, possibly due to an error in calculating the active area.

The *J-V* curve of the champion 15.5% efficient (reverse scan) PSC fabricated with the optimized process is depicted in Fig. 7.7d. Short-circuit current and open-circuit voltage

are both very near the values reported for the record cells (NREL, 2020), while the fill factor is below the highest values reported, which is likely due to a series resistance at the contacts.

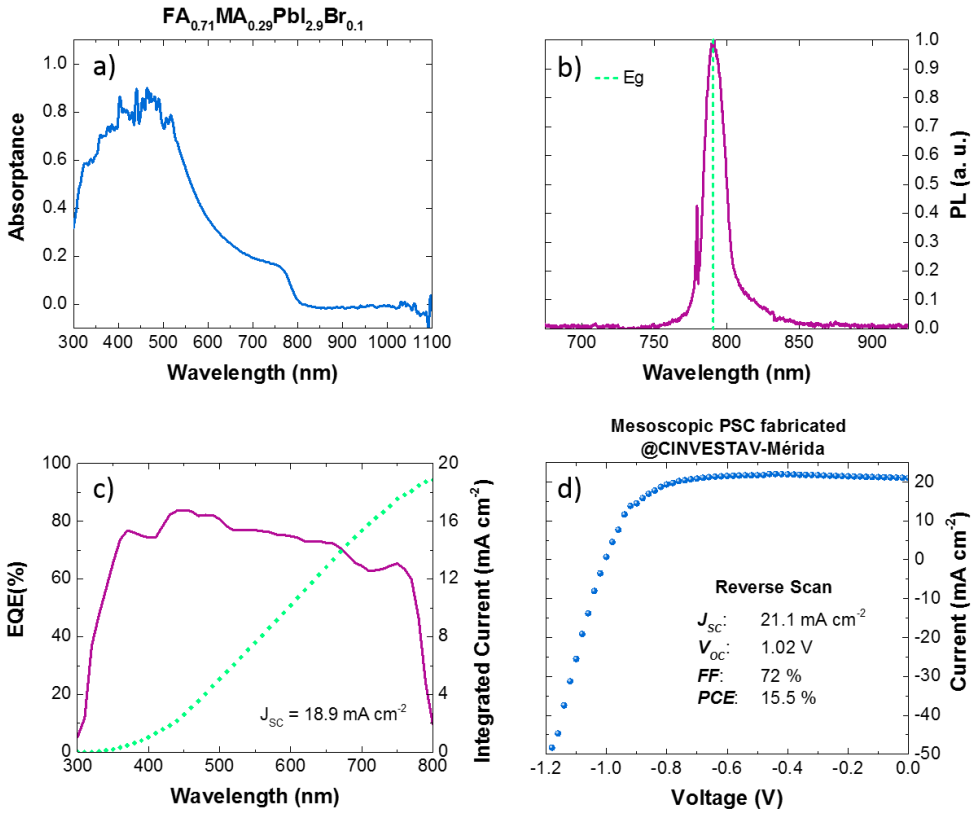

Figure 7.7. a) Absorptance spectrum of a $FA_{0.71}MA_{0.29}PbI_{2.9}Br_{0.1}$ film, b) Steady-state photoluminescence (PL) of a perovskite film deposited on glass, c) External quantum efficiency (EQE) of a high-efficiency perovskite solar cell, and d) *J-V* curve of a high-efficiency PSC, scan rate 0.1 V s^{-1}.

7.3 Insertion of Carbon-Allotropes into PSCs

Degradation of PSCs has been observed to be strongly related to poor electron and hole extraction efficiencies and to ionic mobility towards the interfaces. Insertion of carbon allotropes in PSCs is now widely studied due to their potential application in highly

conductive and functionalized layers (Acik & Darling, 2016; Bouclé & Herlin-Boime, 2016; Fang, Bi, Wang, & Huang, 2017; Hu, Chu, Zhang, Li, & Huang, 2017; Meng et al., 2019). In the present work we study the insertion of graphene-derived materials with the main goal to improve the electron and hole extraction efficiencies at the respective interface, and to prevent ionic transport across the interface.

Graphene and graphene-derived materials present properties that make them attractive for solar cell applications. Some of these properties are: large theoretical specific surface area (2630 $m^2 g^{-1}$), high intrinsic charge carrier mobility (200 000 $cm^2 V^{-1} s^{-1}$), high optical transmittance (~97.7%), and good electrical conductivity (Acik & Darling, 2016). On the other hand, the 0D structure of fullerene enables its use as a building block to construct functional materials and, in particular, its electron-accepting ability makes it a good candidate to hybridize with other materials (M. Chen, Guan, & Yang, 2019). Graphene has been applied in PSCs as conductive electrode, hole/electron transporting material, and to improve the stability of the photovoltaic devices (Agresti et al., 2017; Bouclé & Herlin-Boime, 2016; Liang Lim, Chin Yap, Hafizuddin Hj Jumali, Asri Mat Teridi, & Hoong Teh, 2015). Fullerene has been used as electron transporting material in inverted PSCs, in interfacial modification layers, and as additive in the absorbing perovskite film (Castro, Murillo, Fernandez-Delgado, & Echegoyen, 2018; Fang et al., 2017; Shao, Xiao, Bi, Yuan, & Huang, 2014).

In the present work the incorporation of two types of graphene-derived materials into PSCs is studied: (i) fullerites and (ii) guanidine (Gu) functionalized graphene oxide (GO). In the following sections, the methodologies for the insertion of this materials are presented. In the case of the fullerites, degradation and photovoltaic performance tests are presented.

7.3.1 Insertion of Fullerites into the Perovskite Film

Fullerites are hybrid nano-allotropes formed from a mixture of graphene sheets and fullerenes (C_{60}). These materials are defective graphene sheets with modified Van der Waals stacking interactions (Tapia, Larios, Bittencourt, Yacamán, & Quintana, 2016), in which surface functionalities can be exploited to improve the electrical properties (Sierra-Castillo et al., 2018).

Fullerites were synthesized by ultrasonication with the addition of C_{60} to previously exfoliated few layer graphene (FLG), according to the method reported by Tapia *et al*. (Tapia et al., 2016). The use of ultrasonication techniques allows control over size, morphology and composition of the nano-allotropes, in contrast to other commonly used techniques. The nano-allotropes were incorporated as an additive in the perovskite film by substituting 10% of the volume of DMF in solution A (Section 7.2.4i) with a solution of fullerites with concentration of 1 mg/mL in DMF. Pristine $FA_{0.71}MA_{0.29}PbI_{2.9}Br_{0.1}$ perovskite and perovskite + fullerite films are shown in Fig. 7.8a, b. The SEM images reveal smaller grain size and a smoother surface in the films containing fullerites.

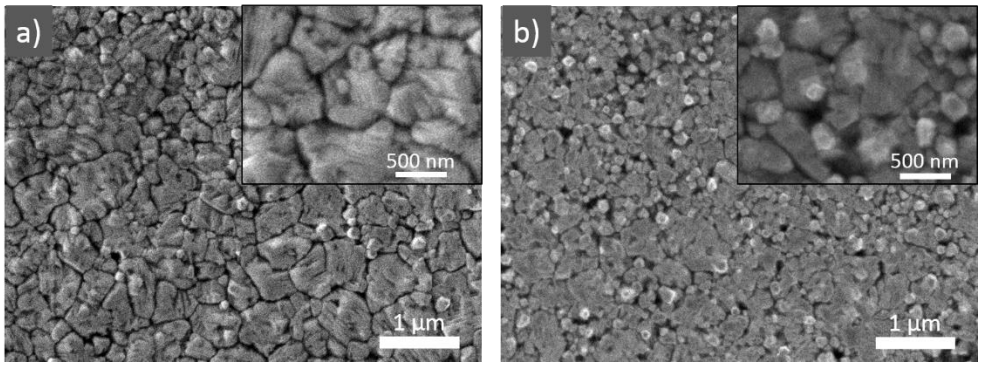

Figure 7.8. SEM (SEI) images of, a) pristine perovskite film and b) mixed perovskite + fullerite film.

Degradation of the perovskite material upon exposure to light and moisture was studied using XRD. Both pristine perovskite and perovskite + fullerite films were exposed for 12 h to ambient conditions, i.e. ~ 1000 W m^{-2} and 75% R.H. The diffractograms presented in Figure 7.9 a, b show differences in the crystallinity and composition of the perovskite before and after ageing. The perovskite peaks exhibit size broadening changes, evidenced from the change in height of the principal peak (110) at $2\Theta = 14°$ (Park et al., 2016). The augmentation in the full-width at half-maximum (FWHM) of the principal peak indicates an increment in the crystallite dimensions for the degraded samples. However, the changes are not as strong in the films containing fullerites as they are in the pristine films. On the other hand, formation of lead iodide (PbI_2) and methyl ammonium bromide (MABr) occurs in both types of material, as indicated from the observed (001) PbI_2 peak at 12.7 ° and a peak at 20.2 °corresponding to MABr (J. Ding et al., 2017).

J-V curves of PSCs fabricated using perovskite + fullerite as the absorbing material are shown in Figure 7.9c. J_{SC} of these devices are somewhat lower than that of PSCs without fullerites: 20.3 mA cm^{-2} versus 22.7 mA cm^{-2}, respectively. However, both the V_{OC} and *FF* values strongly decline from 0.98 V to 0.91 V, and from 63% to 51%. A low shunt resistance can be inferred from the *J-V* curve shape, indicating alternate paths for the photogenerated carriers, which would explain the reduction in current and voltage. Apparently, the insertion of the carbon-allotropes induces the formation of defects where the generated current might be lost. This could be related to the smaller grain size with the fullerite preventing grain interconnection.

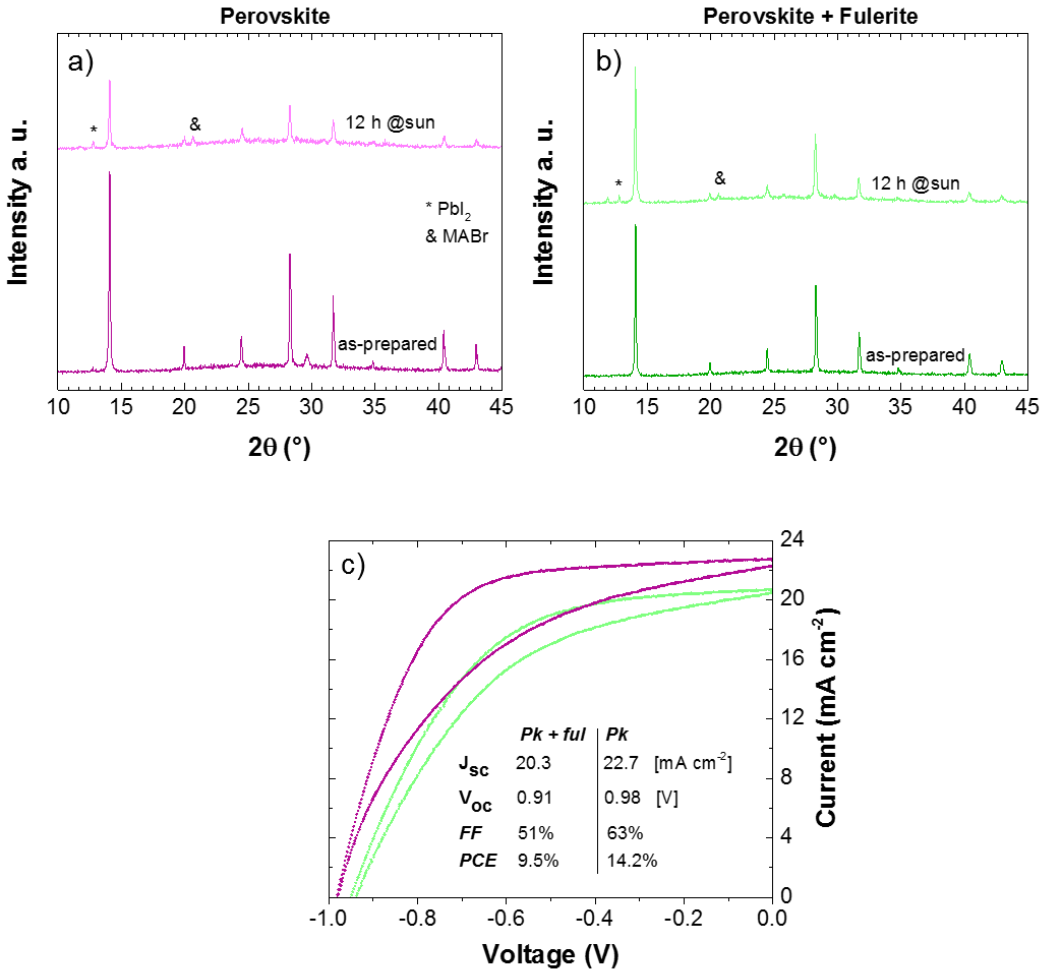

Figure 7.9. X-ray diffractograms of, a) pristine perovskite and b) perovskite + fullerite films. As prepared and aged (12 h @ under ambient conditions) films are shown. c) *J-V* curves of PSCs prepared with perovskite + fullerite as the absorbing material; the scan rate is 0.1 V s^{-1}.

7.3.2 Deposition of Graphene Oxide on the Perovskite Film

A functionalized graphene oxide (GO) was produced using a modified Hummers method (Eda & Chhowalla, 2010). The obtained GO was dispersed in water and guanidine hydrochloride (2 molar equiv. per GO) was added and stirred for 12 hours and finally rinsed. Figure 7.10a shows a transmission electron microscopy (TEM) image of a GO flake and the Raman spectrum. The micrography demonstrates the proper exfoliation of the graphite to

few-layer graphene and the Raman spectrum presents the principal peaks of the graphene oxide, in accordance with the literature (Kaniyoor & Ramaprabhu, 2012). The adequate functionalization of the material was studied through Fourier-transform infrared spectroscopy (FTIR), Figure 7.10b. In comparison with pristine GO, the FTIR spectrum of GO + Gu shows a peak appearing at 1660 cm^{-1}, which is mainly attributed to the -NH stretching in the Gu molecule (Kuppusamy et al., 2018; P. Li et al., 2017), confirming the presence of Gu.

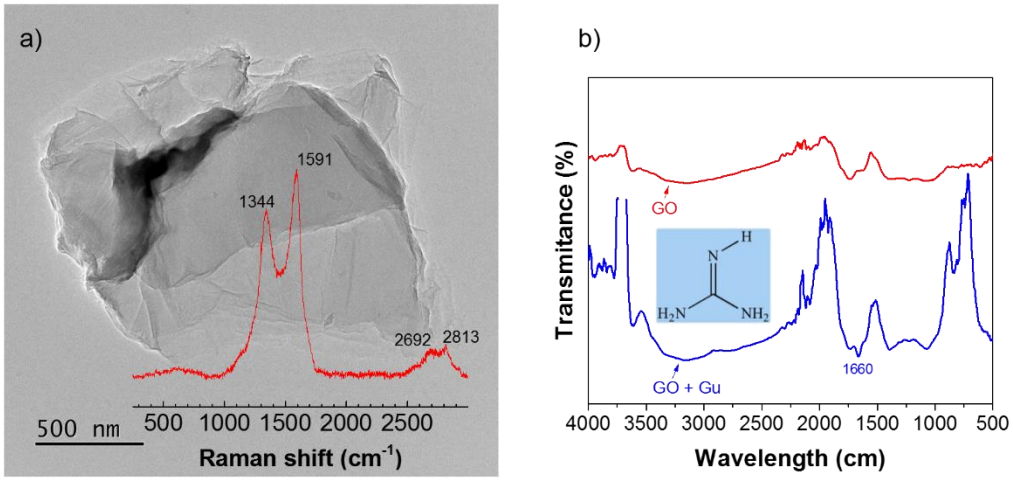

Figure 7.10. a) TEM image and Raman spectrum of the obtained GO, and b) FTIR spectrum of pristine GO (red) and GO functionalized with guanidine (Gu), Gu molecule is shown in the inset.

Thin layers of GO + Gu were deposited on top of perovskite films through spray pyrolysis of an ethanol-based dispersion (2 mg/mL) at 65°C, with the main idea to generate a chemical insulating layer that would interact with detrimental migrating species. The deposits were performed under air atmosphere at 30% R.H. without any apparent degradation of the perovskite films. Low roughness and conformal coverage are desired characteristics of these films, which has presented important challenges for the incorporation of this type of

materials (Agresti et al., 2017; D. H. Wang et al., 2013). In order to observe the evolution in film coverage, three different volumes of the dispersion were used to spray an area of about 25 cm^2: 1.5 mL, 3.0 mL and 6.0 mL. Figure 7.11 shows atomic force microscope (AFM) images of the perovskite film and the three different GO + Gu deposits. The images show that 1.5 mL of the GO + Gu dispersion is not enough to obtain a complete layer. With a volume > 3 mL a layer of GO + Gu is formed, and good coverage of the perovskite grains is obtained using > 6 mL of the dispersion. In addition, stacking of the material is observed to occur with larger volume, which limits the amount of material that can be deposited in order to keep the roughness low.

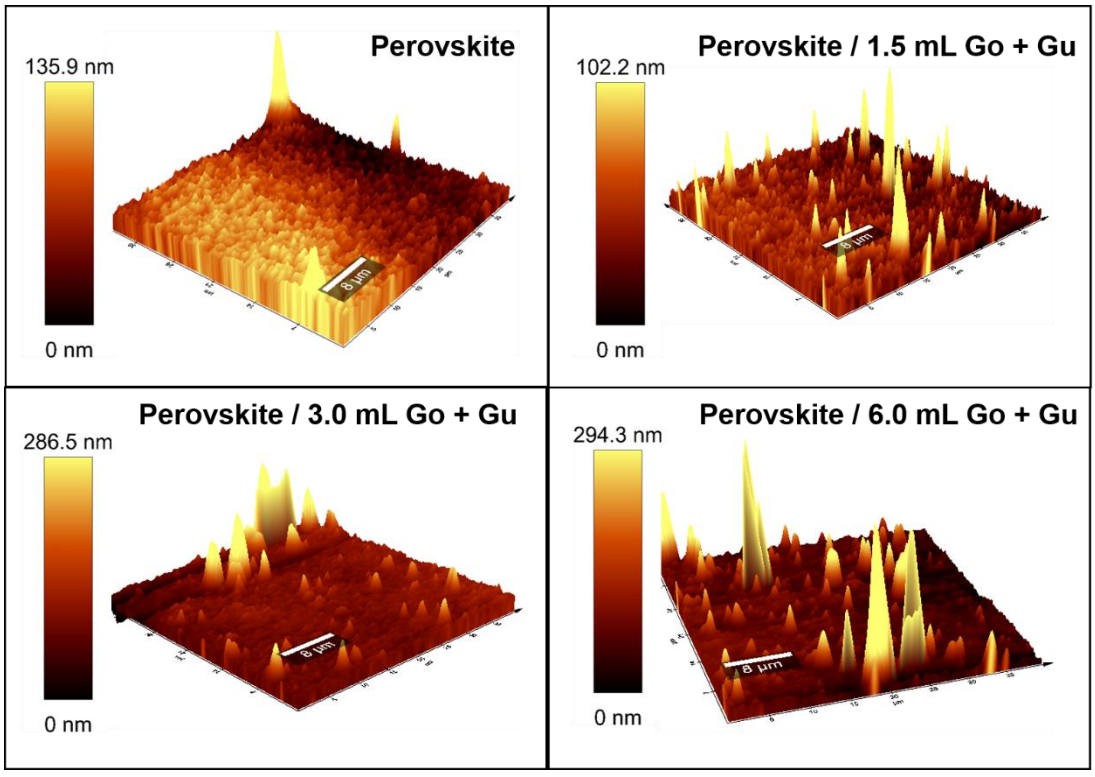

Figure 7.11. AFM images of plain perovskite and GO + Gu material deposited on top of the perovskite, using different volumes of the dispersion: 1.5 mL, 3.0 mL and 6.0 mL

7.4 Conclusions

The optimization process for the successful fabrication of high-efficiency perovskite solar cells is presented. Each strategy presented here is accompanied by relevant literature and observations that supported the process. The high sensitivity of the formation process of the perovskite material was depicted and the importance of a precise control on the crystallization process was demonstrated. The accomplishment of the optimization was demonstrated trough the improvement of the photovoltaic parameters along the process. Finally, the high quality of the $FA_{0.71}MA_{0.29}PbI_{2.9}Br_{0.1}$ films obtained were characterized showing optoelectronic properties that are in accordance with the literature.

Preliminary results on the incorporation of fullerites in the perovskite layer are presented, showing that the current remains high, but that both the V_{OC} and FF decrease, possibly related to the ability of the very fine NPs to generate shunts, which point to defects in the BL layer. In order to take full advantage of the fullerites, a careful study of the interaction between fullerites and perovskite is needed. On the other hand, it was demonstrated that the insertion of an interlayer of GO with good coverage can be achieved through spray pyrolysis of alcohol-based dispersions under ambient conditions. The main goal is to improve the electron and hole extraction efficiencies at the respective interface, and to prevent ionic transport across the interface, thus preventing degradation reactions.

Acknowledgment

The authors would like to thank Dr. David Meneses for his collaboration on the carbon-allotropes insertion experiments.

CHAPTER 8

Conclusions and Outlook

CHAPTER 8

Conclusions and Outlook

8.1 Summary

This thesis is focused on the fabrication and characterization of perovskite solar cells (PSCs) with the purpose of increasing its applications and improving its stability. Reducing the energy pay-back time and enlarging the lifetime of the devices is of utmost importance to improve the commercial viability of this technology. Considerable research has been done in recent years on these topics; however, there remain open questions to be assessed in order to fully exploit the potential of PSCs.

A low temperature (LT) fabrication route for the insertion of a mesoporous (mp) TiO_2-based scaffold was developed. Photovoltaic efficiencies of 14% - 16% were achieved for mesoscopic devices with mp film thickness ranging from 120 to 480 nm by fine-tuning the PbI_2 solution chemistry in each case. Unlike in DSSCs, it was observed that neither particle interconnection nor layer thickness of the mp scaffold is crucial if a proper infiltration of the perovskite material is achieved. This result is in accordance with suggestions of the charge carrier transport properties being dominated by the bulk of the absorbing material (Contreras-Bernal et al., 2017; Correa-Baena et al., 2017; Guerrero, Garcia-Belmonte, et al., 2016). The PV performance of planar and mesoscopic PSCs was compared. A difference in

the open-circuit voltage, V_{OC}, for the two configurations was observed: 0.97 V and 1.1 V for planar and mesoscopic PSCs, respectively. The latter seems to be caused by a difference in the electronic characteristics of the compact and mesoporous scaffolds.

A detailed study of the degradation dynamics of the PV parameters under exposure to light and moisture revealed that the incorporation of a LT mp layer into the planar PSCs almost doubles the half-life time of the devices. A larger decrease in the photocurrent of planar PSCs with respect to that of mesoscopic PSCs indicates that degradation is related to an increased recombination rate. Comparison of the perovskite film degradation and PV performance of PSCs prepared using different scaffolds demonstrated that the electronic properties of the ETL play an important role in the stability of the devices. Furthermore, detailed analysis of the optical and compositional analysis of the perovskite absorbing layer show that in the presence of a mp-TiO_2, the PV performance is preserved despite deterioration of the perovskite material.

Impedance spectroscopy analysis revealed a mechanism of charge accumulation at high light intensities, which is more pronounced in mesoscopic PSCs. The high and low frequency resistive components were shown to be dominated by two different recombination mechanisms, which to our knowledge was not observed in previous IS analysis. It appears that Shockley-Read-Hall recombination dominates at low light intensity (< 10 mW cm^{-2}), which strongly suggests that photogenerated charge recombines within the bulk of the absorbing material at such irradiance values. On the other hand, an ideality factor n_{ID} between 0.6 and 1.0 was observed for high light intensities, which has been related to a recombination mechanism at the interfaces (Wolfgang Tress et al., 2018). From the analysis of the capacitive element it was shown that charge accumulation is occurring at the interfaces and that this is

more pronounced in planar devices. These results along with an inductive feature indicating charge stabilization in mesoscopic devices are clear evidence of a different electrostatic environment at the mp-TiO_2/perovskite interface. The observed difference was related to the slower degradation dynamics in mesoscopic PSCs. A model accounting for a mechanism of enhanced charge extraction was proposed. The main idea is that charge stabilization in mesoscopic PSCs and a more favorable band alignment gives place to better performance even if degradation of the perovskite material has occurred.

Development of high-efficiency PSCs is of utter importance for the study of the working principles. Thus, a complementary study of the optimization process for the fabrication of PSCs under controlled atmosphere has been developed. The hybrid lead halide perovskite material has been observed to be extremely sensitive to solvent composition of its surroundings (Pathak et al., 2015; Sheikh et al., 2015). In this work, three specific processes were identified as source of changes in the atmosphere composition: i) spin coating conditions, ii) annealing process and iii) anti-solvent treatment. Through morphological and composition analysis of the different films in the solar devices, mesoscopic PSCs where successfully fabricated in the Nanomaterias laboratory at Cinvestav-Mérida with a highest PCE of 15.5%.

Degradation of PSCs has been observed to be strongly related to poor electron and hole extraction efficiencies and to ionic mobility towards the interfaces. Insertion of carbon allotropes in PSCs is now widely studied due to their potential application in highly conductive and functionalized layers (Acik & Darling, 2016; Bouclé & Herlin-Boime, 2016; Fang et al., 2017; Hu et al., 2017; Meng et al., 2019). In this work, preliminary results on the incorporation of fullerites and functionalized graphene oxide (GO) in PSCs are presented.

In the case of fullerites PV performance of the devices is lower upon insertion, which is possibly related to the ability of the very fine NPs to generate shunts. On the other hand, it was demonstrated that the insertion of an interlayer of GO with good coverage can be achieved through spray pyrolysis of alcohol-based dispersions under ambient conditions.

8.2 Outlook

The results presented in this thesis have helped to increase the understanding of the impact of the interfaces on the performance of PSCs. The study on the degradation dynamics shows very clearly that the stability of PSCs is improved when a crystalline mesoporous layer is inserted. Thus, the incorporation of such material through the low temperature process developed in this work is of high potential for the fabrication of low cost and stable PSCs. The importance of adequate electronic properties of the electron transport layer (ETL) for both performance and stability is highlighted; although this had been assessed before by other authors, nonetheless the contribution of this work is the deduction of the beneficial electrostatic interactions at the ETL/perovskite interface for slowing down the degradation dynamics.

Further research is needed on the relation of charge accumulation and the charge extraction mechanism. It appears that charge accumulation is critical to generating a mechanism of enhanced electron injection through splitting of the quasi Fermi levels in mesoscopic PSCs. It has been hypothesized that the accumulated charge is of ionic nature, supported by the hysteretic behavior observed. However, the nature of such charge along with the electron injection mechanism needs to be studied more directly.

The careful assessment of the electrical properties could be applied to studying changes in the charge transport dynamics under different bias conditions at different stages of degradation. It is likely that degradation and built-in electrostatic field will be linked, thus it would be interesting to monitor the device at different operating points. Furthermore, the present analysis could be complemented very well with time-resolved spectroscopies to investigate the rapid dynamics of electron injection, which appears to be critical to controlling the stability of PSCs.

The methodology for the insertion of the graphene-derived materials developed in this work could be applied to a wide range of different carbon allotropes and further study their effect on the ionic and electrical conductivity of the perovskite material. This might be done through electrochemistry characterization of this systems.

References

Abdi-Jalebi, M., Dar, M. I., Sadhanala, A., Senanayak, S. P., Giordano, F., Zakeeruddin, S. M., … Friend, R. H. (2016). Impact of a Mesoporous Titania–Perovskite Interface on the Performance of Hybrid Organic–Inorganic Perovskite Solar Cells. *The Journal of Physical Chemistry Letters*, *7*(16), 3264–3269. https://doi.org/10.1021/acs.jpclett.6b01617

Acik, M., & Darling, S. B. (2016). Graphene in perovskite solar cells: Device design, characterization and implementation. *Journal of Materials Chemistry A*, *4*(17), 6185–6235. https://doi.org/10.1039/c5ta09911k

Adachi, H., & Wasa, K. (2012). Thin Films and Nanomaterials. In *Handbook of Sputter Deposition Technology: Fundamentals and Applications for Functional Thin Films, Nano-Materials and MEMS: Second Edition* (pp. 3–39). Elsevier Inc. https://doi.org/10.1016/B978-1-4377-3483-6.00001-2

Agresti, A., Pescetelli, S., Palma, A. L., Del Rio Castillo, A. E., Konios, D., Kakavelakis, G., … Di Carlo, A. (2017). Graphene Interface Engineering for Perovskite Solar Modules: 12.6% Power Conversion Efficiency over 50 cm2 Active Area. *ACS Energy Letters*, *2*(1), 279–287. https://doi.org/10.1021/acsenergylett.6b00672

Ahn, N., Kwak, K., Jang, M. S., Yoon, H., Lee, B. Y., Lee, J.-K., … Choi, M. (2016). Trapped charge-driven degradation of perovskite solar cells. *Nature Communications*, *7*, 13422. https://doi.org/10.1038/ncomms13422

Almora, O., Cho, K. T., Aghazada, S., Zimmermann, I., Matt, G. J., Brabec, C. J., … Garcia-Belmonte, G. (2018). Discerning recombination mechanisms and ideality factors through impedance analysis of high-efficiency perovskite solar cells. *Nano Energy*, *48*, 63–72. https://doi.org/10.1016/j.nanoen.2018.03.042

Almora, O., Guerrero, A., & Garcia-Belmonte, G. (2016). Ionic charging by local imbalance at interfaces in hybrid lead halide perovskites. *Applied Physics Letters*, *108*(4), 043903. https://doi.org/10.1063/1.4941033

Almora, O., Zarazua, I., Mas-Marza, E., Mora-Sero, I., Bisquert, J., & Garcia-Belmonte, G. (2015). Capacitive Dark Currents, Hysteresis, and Electrode Polarization in Lead Halide Perovskite Solar Cells. *The Journal of Physical Chemistry Letters*, *6*(9), 1645–1652. https://doi.org/10.1021/acs.jpclett.5b00480

Almosni, S., Delamarre, A., Jehl, Z., Suchet, D., Cojocaru, L., Giteau, M., … Guillemoles, J. F. (2018, December 31). Material challenges for solar cells in the twenty-first century: directions in emerging technologies. *Science and Technology of Advanced Materials*. Taylor and Francis Ltd. https://doi.org/10.1080/14686996.2018.1433439

Aranda, C., Cristobal, C., Shooshtari, L., Li, C., Huettner, S., & Guerrero, A. (2017). Formation criteria of high efficiency perovskite solar cells under ambient conditions. *Sustainable Energy and Fuels*, *1*(3), 540–547. https://doi.org/10.1039/c6se00077k

Aristidou, N., Sanchez-Molina, I., Chotchuangchutchaval, T., Brown, M., Martinez, L., Rath, T., & Haque, S. A. (2015). The Role of Oxygen in the Degradation of

Methylammonium Lead Trihalide Perovskite Photoactive Layers. *Angewandte Chemie International Edition*, *54*(28), 8208–8212. https://doi.org/10.1002/anie.201503153

Arora, N., Dar, M. I., Abdi-Jalebi, M., Giordano, F., Pellet, N., Jacopin, G., … Grätzel, M. (2016). Intrinsic and Extrinsic Stability of Formamidinium Lead Bromide Perovskite Solar Cells Yielding High Photovoltage. *Nano Letters*, *16*(11), 7155–7162. https://doi.org/10.1021/acs.nanolett.6b03455

Asghar, M. I., Zhang, J., Wang, H., & Lund, P. D. (2017). Device stability of perovskite solar cells – A review. *Renewable and Sustainable Energy Reviews*. Elsevier Ltd. https://doi.org/10.1016/j.rser.2017.04.003

Azmi, R., Lee, C.-L., Jung, I. H., & Jang, S.-Y. (2018). Simultaneous Improvement in Efficiency and Stability of Low-Temperature-Processed Perovskite Solar Cells by Interfacial Control. *Advanced Energy Materials*, *8*(14), 1702934. https://doi.org/10.1002/aenm.201702934

Azpiroz, J. M., Mosconi, E., Bisquert, J., & De Angelis, F. (2015). Defect migration in methylammonium lead iodide and its role in perovskite solar cell operation. *Energy & Environmental Science*, *8*(7), 2118–2127. https://doi.org/10.1039/C5EE01265A

Back, H., Kim, G., Kim, J., Kong, J., Kim, T. K., Kang, H., … Lee, K. (2016). Achieving long-term stable perovskite solar cells: Via ion neutralization. *Energy and Environmental Science*, *9*(4), 1258–1263. https://doi.org/10.1039/c6ee00612d

Bag, M., Renna, L. A., Adhikari, R. Y., Karak, S., Liu, F., Lahti, P. M., … Venkataraman, D. (2015). Kinetics of Ion Transport in Perovskite Active Layers and Its Implications for Active Layer Stability. *Journal of the American Chemical Society*, *137*(40), 13130–13137. https://doi.org/10.1021/jacs.5b08535

Bastos, J. P., Paetzold, U. W., Gehlhaar, R., Qiu, W., Cheyns, D., Surana, S., … Poortmans, J. (2018). Light-Induced Degradation of Perovskite Solar Cells: The Influence of 4-Tert-Butyl Pyridine and Gold. *Advanced Energy Materials*, *8*(23), 1800554. https://doi.org/10.1002/aenm.201800554

Berhe, T. A., Su, W. N., Chen, C. H., Pan, C. J., Cheng, J. H., Chen, H. M., … Hwang, B. J. (2016, February 1). Organometal halide perovskite solar cells: Degradation and stability. *Energy and Environmental Science*. Royal Society of Chemistry. https://doi.org/10.1039/c5ee02733k

Bhagyaraj, S. M., Oluwafemi, S. O., Kalarikkal, N., & Thomas, S. (n.d.). *Synthesis of Inorganic Nanomaterials : Advances and Key Technologies.*

Bi, D., El-Zohry, A. M., Hagfeldt, A., & Boschloo, G. (2015). Unraveling the Effect of PbI $_2$ Concentration on Charge Recombination Kinetics in Perovskite Solar Cells. *ACS Photonics*, *2*(5), 589–594. https://doi.org/10.1021/ph500255t

Bouclé, J., & Herlin-Boime, N. (2016). The benefits of graphene for hybrid perovskite solar cells. *Synthetic Metals*, *222*, 3–16. https://doi.org/10.1016/j.synthmet.2016.03.030

Brug, G. J., van den Eeden, A. L. G., Sluyters-Rehbach, M., & Sluyters, J. H. (1984). The analysis of electrode impedances complicated by the presence of a constant phase

element. *Journal of Electroanalytical Chemistry and Interfacial Electrochemistry*, *176*(1–2), 275–295. https://doi.org/10.1016/S0022-0728(84)80324-1

Bryant, D., Aristidou, N., Pont, S., Sanchez-Molina, I., Chotchunangatchaval, T., Wheeler, S., … Haque, S. A. (2016). Light and oxygen induced degradation limits the operational stability of methylammonium lead triiodide perovskite solar cells. *Energy Environ. Sci.*, *9*(5), 1655–1660. https://doi.org/10.1039/C6EE00409A

Burschka, J., Pellet, N., Moon, S. J., Humphry-Baker, R., Gao, P., Nazeeruddin, M. K., & Grätzel, M. (2013). Sequential deposition as a route to high-performance perovskite-sensitized solar cells. *Nature*, *499*(7458), 316–319. https://doi.org/10.1038/nature12340

Calado, P., Telford, A. M., Bryant, D., Li, X., Nelson, J., O'Regan, B. C., & Barnes, P. R. F. (2016). Evidence for ion migration in hybrid perovskite solar cells with minimal hysteresis. *Nature Communications*, *7*, 1–10. https://doi.org/10.1038/ncomms13831

Carnie, M. J., Charbonneau, C., Davies, M., Mabbett, I., Watson, T., & Worsley, D. (2013). TiO2 film morphology, electron transport and electron lifetime in ultra-fast sintered Dye-sensitized solar cells. In *Materials Research Society Symposium Proceedings* (Vol. 1493, pp. 121–126). https://doi.org/10.1557/opl.2012

Carrillo, J., Guerrero, A., Rahimnejad, S., Almora, O., Zarazua, I., Mas-Marza, E., … Garcia-Belmonte, G. (2016). Ionic Reactivity at Contacts and Aging of Methylammonium Lead Triiodide Perovskite Solar Cells. *Advanced Energy Materials*, *6*(9), 1502246. https://doi.org/10.1002/aenm.201502246

Castro-Chong, A., Qiu, W., Bastos, J., Tchamba Yimga, N., García-Rodríguez, R., Idígoras, J., … Oskam, G. (2020). Impact of the implementation of a mesoscopic TiO2 film from a low-temperature method on the performance and degradation of hybrid perovskite solar cells. *Solar Energy*, *201*, 836–845. https://doi.org/10.1016/j.solener.2020.03.041

Castro, E., Murillo, J., Fernandez-Delgado, O., & Echegoyen, L. (2018). Progress in fullerene-based hybrid perovskite solar cells. *J. Mater. Chem. C*, *6*, 2635. https://doi.org/10.1039/c7tc04302c

Charbonneau, C., Cameron, P. J., Pockett, A., Lewis, A., Troughton, J. R., Jewell, E., … Watson, T. M. (2016). Solution processing of TiO2 compact layers for 3rd generation photovoltaics. *Ceramics International*, *42*(10), 11989–11997. https://doi.org/10.1016/j.ceramint.2016.04.125

Chen, B., Yang, M., Zheng, X., Wu, C., Li, W., Yan, Y., … Priya, S. (2015). Impact of Capacitive Effect and Ion Migration on the Hysteretic Behavior of Perovskite Solar Cells. *The Journal of Physical Chemistry Letters*, *6*(23), 4693–4700. https://doi.org/10.1021/acs.jpclett.5b02229

Chen, J.-Y., Chueh, C.-C., Zhu, Z., Chen, W.-C., & Jen, A. K.-Y. (2017). Low-temperature electrodeposited crystalline SnO2 as an efficient electron transporting layer for conventional perovskite solar cells. *SOLAR ENERGY MATERIALS AND SOLAR CELLS*, *164*, 47–55. https://doi.org/10.1016/j.solmat.2017.02.008

Chen, J., Song, J., Huang, F., Li, H., Liu, S., Wang, M., & Shen, Y. (2017). The Role of Synthesis Parameters on Crystallization and Grain Size in Hybrid Halide Perovskite Solar Cells. *Journal of Physical Chemistry C*, *121*(32), 17053–17061. https://doi.org/10.1021/acs.jpcc.7b03279

Chen, M., Guan, R., & Yang, S. (2019). Hybrids of Fullerenes and 2D Nanomaterials. *Advanced Science*, *6*(1), 1800941. https://doi.org/10.1002/advs.201800941

Cohen, B. El, & Etgar, L. (2016). Parameters that control and influence the organo-metal halide perovskite crystallization and morphology. *Frontiers of Optoelectronics*, *9*(1), 44–52. https://doi.org/10.1007/s12200-016-0630-3

Contreras-Bernal, L., Ramos-Terrón, S., Riquelme, A., Boix, P. P., Idígoras, J., Mora-Seró, I., & Anta, J. A. (2019). Impedance analysis of perovskite solar cells: A case study. *Journal of Materials Chemistry A*, *7*(19), 12191–12200. https://doi.org/10.1039/c9ta02808k

Contreras-Bernal, L., Salado, M., Todinova, A., Calio, L., Ahmad, S., Idígoras, J., & Anta, J. A. (2017). Origin and Whereabouts of Recombination in Perovskite Solar Cells. *The Journal of Physical Chemistry C*, *121*(18), 9705–9713. https://doi.org/10.1021/acs.jpcc.7b01206

Contreras, L., Idígoras, J., Todinova, A., Salado, M., Kazim, S., Ahmad, S., & Anta, J. A. (2016). Specific cation interactions as the cause of slow dynamics and hysteresis in dye and perovskite solar cells: a small-perturbation study. *Physical Chemistry Chemical Physics*, *18*(45), 31033–31042. https://doi.org/10.1039/C6CP05851E

Correa-Baena, J.-P., Turren-Cruz, S.-H., Tress, W., Hagfeldt, A., Aranda, C., Shooshtari, L., … Guerrero, A. (2017). Changes from Bulk to Surface Recombination Mechanisms between Pristine and Cycled Perovskite Solar Cells. *ACS Energy Letters*, *2*(3), 681–688. https://doi.org/10.1021/acsenergylett.7b00059

Davies, M. L., Carnie, M., Holliman, P. J., Connell, A., Douglas, P., Watson, T., … Worsley, D. (2014a). Compositions, colours and efficiencies of organic–inorganic lead iodide/bromide perovskites for solar cells. *Energy Materials: Materials Science and Engineering for Energy Systems*, *9*(4), 482–485. https://doi.org/10.1179/1433075X14Y.0000000252

Davies, M. L., Carnie, M., Holliman, P. J., Connell, A., Douglas, P., Watson, T., … Worsley, D. (2014b). Compositions, colours and efficiencies of organic–inorganic lead iodide/bromide perovskites for solar cells. *Energy Materials: Materials Science and Engineering for Energy Systems*, *9*(4), 482–485. https://doi.org/10.1179/1433075X14Y.0000000252

De Wolf, S., Holovsky, J., Moon, S. J., Löper, P., Niesen, B., Ledinsky, M., … Ballif, C. (2014). Organometallic halide perovskites: Sharp optical absorption edge and its relation to photovoltaic performance. *Journal of Physical Chemistry Letters*, *5*(6), 1035–1039. https://doi.org/10.1021/jz500279b

Ding, C., Zhang, Y., Liu, F., Kitabatake, Y., Hayase, S., Toyoda, T., … Shen, Q. (2018). Effect of the conduction band offset on interfacial recombination behavior of the

planar perovskite solar cells. *Nano Energy*, *53*, 17–26. https://doi.org/10.1016/j.nanoen.2018.08.031

Ding, J., Zhao, Y., Du, S., Sun, Y., Cui, H., Zhan, X., … Jing, L. (2017). Controlled growth of MAPbBr3 single crystal: understanding the growth morphologies of vicinal hillocks on (100) facet to form perfect cubes. *Journal of Materials Science*, *52*(13), 7907–7916. https://doi.org/10.1007/s10853-017-0995-8

Du, T., Burgess, C. H., Kim, J., Zhang, J., Durrant, J. R., & Mclachlan, M. A. (2017). Formation, location and beneficial role of PbI 2 in lead halide perovskite solar cells. *Sustainable Energy and Fuels*, (1), 119–126. https://doi.org/10.1039/c6se00029k

Eames, C., Frost, J. M., Barnes, P. R. F., O'Regan, B. C., Walsh, A., & Islam, M. S. (2015). Ionic transport in hybrid lead iodide perovskite solar cells. *Nature Communications*, *6*(1), 7497. https://doi.org/10.1038/ncomms8497

Eda, B. G., & Chhowalla, M. (2010). Chemically Derived Graphene Oxide : Towards Large-Area Thin-Film Electronics and Optoelectronics, 2392–2415. https://doi.org/10.1002/adma.200903689

El-Mellouhi, F., Rashkeev, S. N., Marzouk, A., Kabalan, L., Belaidi, A., Merzougui, B., … Alharbi, F. H. (2019). Intrinsic stability enhancement and ionic migration reduction by fluorinated cations incorporated in hybrid lead halide perovskites. *Journal of Materials Chemistry C*, *7*(18), 5299–5306. https://doi.org/10.1039/c8tc06308g

El Kamel, F., Gonon, P., Jomni, F., & Yangui, B. (2008). Observation of negative capacitances in metal-insulator-metal devices based on a-BaTiO3:H. *Applied Physics Letters*, *93*(4), 042904. https://doi.org/10.1063/1.2966352

Eperon, G. E., Burlakov, V. M., Docampo, P., Goriely, A., & Snaith, H. J. (2014). Morphological control for high performance, solution-processed planar heterojunction perovskite solar cells. *Advanced Functional Materials*, *24*(1), 151–157. https://doi.org/10.1002/adfm.201302090

European Photovoltaic Industry Association Solar Generation. (2011).

Fabregat-Santiago, F., Bisquert, J., Garcia-Belmonte, G., Boschloo, G., & Hagfeldt, A. (2005). Influence of electrolyte in transport and recombination in dye-sensitized solar cells studied by impedance spectroscopy. In *Solar Energy Materials and Solar Cells* (Vol. 87, pp. 117–131). Elsevier. https://doi.org/10.1016/j.solmat.2004.07.017

Fabregat-Santiago, F., Garcia-Belmonte, G., Mora-Seró, I., & Bisquert, J. (2011, May 28). Characterization of nanostructured hybrid and organic solar cells by impedance spectroscopy. *Physical Chemistry Chemical Physics*. https://doi.org/10.1039/c0cp02249g

Fang, Y., Bi, C., Wang, D., & Huang, J. (2017). The Functions of Fullerenes in Hybrid Perovskite Solar Cells, *2*, 782–794. https://doi.org/10.1021/acsenergylett.6b00657

Fedeli, P., Gazza, F., Calestani, D., Ferro, P., Besagni, T., Zappettini, A., … Mosca, R. (2015). Influence of the Synthetic Procedures on the Structural and Optical Properties of Mixed-Halide (Br, I) Perovskite Films. *Journal of Physical Chemistry C*, *119*(37),

21304–21313. https://doi.org/10.1021/acs.jpcc.5b03923

Filip, M. R., Eperon, G. E., Snaith, H. J., & Giustino, F. (2014). Steric engineering of metal-halide perovskites with tunable optical band gaps. *Nature Communications*, *5*, 5757. https://doi.org/10.1038/ncomms6757

Gagliardi, A., & Abate, A. (2018). Mesoporous Electron-Selective Contacts Enhance the Tolerance to Interfacial Ion Accumulation in Perovskite Solar Cells. *ACS Energy Lett*, *3*, 163–169. https://doi.org/10.1021/acsenergylett.7b01101

Galkowski, K., Mitioglu, A., Miyata, A., Plochocka, P., Portugall, O., Eperon, G. E., … Nicholas, R. J. (2016). Determination of the exciton binding energy and effective masses for methylammonium and formamidinium lead tri-halide perovskite semiconductors. *Energy and Environmental Science*, *9*(3), 962–970. https://doi.org/10.1039/c5ee03435c

Gardner, K. L., Tait, J. G., Merckx, T., Qiu, W., Paetzold, U. W., Kootstra, L., … Poortmans, J. (2016). Nonhazardous Solvent Systems for Processing Perovskite Photovoltaics. *Advanced Energy Materials*, *6*(14), 1600386. https://doi.org/10.1002/aenm.201600386

Ghahremanirad, E., Bou, A., Olyaee, S., & Bisquert, J. (2017). Inductive Loop in the Impedance Response of Perovskite Solar Cells Explained by Surface Polarization Model. *J. Phys. Chem. Lett.*, *8(7)*, 1402–1406. https://doi.org/10.1021/acs.jpclett.7b00415

Gouda, L., Rietwyk, K. J., Hu, J., Kama, A., Ginsburg, A., Priel, M., … Zaban, A. (2017). High-Resolution Study of TiO2 Contact Layer Thickness on the Performance of over 800 Perovskite Solar Cells. *ACS Energy Letters*, *2*(10), 2356–2361. https://doi.org/10.1021/acsenergylett.7b00718

Green, M. A. (2002). Third generation photovoltaics: Solar cells for 2020 and beyond. *Physica E: Low-Dimensional Systems and Nanostructures*, *14*(1–2), 65–70. https://doi.org/10.1016/S1386-9477(02)00361-2

Green, M. A., Hishikawa, Y., Dunlop, E. D., Levi, D. H., Hohl-Ebinger, J., & Ho-Baillie, A. W. Y. (2018). Solar cell efficiency tables (version 51). *Progress in Photovoltaics: Research and Applications*, *26*(1), 3–12. https://doi.org/10.1002/pip.2978

Guerrero, A., Garcia-Belmonte, G., Mora-Sero, I., Bisquert, J., Kang, Y. S., Jacobsson, T. J., … Hagfeldt, A. (2016). Properties of Contact and Bulk Impedances in Hybrid Lead Halide Perovskite Solar Cells Including Inductive Loop Elements. *The Journal of Physical Chemistry C*, *120*(15), 8023–8032. https://doi.org/10.1021/acs.jpcc.6b01728

Guerrero, A., You, J., Aranda, C., Kang, Y. S., Garcia-Belmonte, G., Zhou, H., … Yang, Y. (2016). Interfacial degradation of planar lead halide perovskite solar cells. *ACS Nano*, *10*(1), 218–224. https://doi.org/10.1021/acsnano.5b03687

Han, L., Koide, N., Chiba, Y., Islam, A., Komiya, R., Fuke, N., … Yamanaka, R. (2005). Improvement of efficiency of dye-sensitized solar cells by reduction of internal resistance. *Applied Physics Letters*, *86*(21), 1–3. https://doi.org/10.1063/1.1925773

Heo, J. H., Song, D. H., & Im, S. H. (2014). Planar CH3NH3PbBr3 hybrid solar cells with 10.4% power conversion efficiency, fabricated by controlled crystallization in the spin-coating process. *Advanced Materials*, *26*(48), 8179–8183. https://doi.org/10.1002/adma.201403140

Holliman, P. J., Connell, A., Davies, M., Carnie, M., Bryant, D., & Jones, E. W. (2019). Low temperature sintering of aqueous TiO2 colloids for flexible, co-sensitized dye-sensitized solar cells. *Materials Letters*, *236*, 289–291. https://doi.org/10.1016/j.matlet.2018.10.118

Hu, R., Chu, L., Zhang, J., Li, X., & Huang, W. (2017). Carbon materials for enhancing charge transport in the advancements of perovskite solar cells. *JOURNAL OF POWER SOURCES*, *361*, 259–275. https://doi.org/10.1016/j.jpowsour.2017.06.051

Im, J.-H., Lee, C.-R., Lee, J.-W., Park, S.-W., & Park, N.-G. (2011). 6.5% Efficient Perovskite Quantum-Dot-Sensitized Solar Cell. *Nanoscale*, *3*(10), 4088. https://doi.org/10.1039/c1nr10867k

Im, J. H., Kim, H. S., & Park, N. G. (2014). Morphology-photovoltaic property correlation in perovskite solar cells: One-step versus two-step deposition of CH3NH3PbI 3. *APL Materials*, *2*(8). https://doi.org/10.1063/1.4891275

Ito, S., Murakami, T. N., Comte, P., Liska, P., Grätzel, C., Nazeeruddin, M. K., & Grätzel, M. (2008). Fabrication of thin film dye sensitized solar cells with solar to electric power conversion efficiency over 10%. *Thin Solid Films*, *516*(14), 4613–4619. https://doi.org/10.1016/j.tsf.2007.05.090

Jacobs, D. A., Wu, Y., Shen, H., Barugkin, C., Beck, F. J., White, T. P., … Catchpole, K. R. (2017). Hysteresis phenomena in perovskite solar cells: The many and varied effects of ionic accumulation. *Physical Chemistry Chemical Physics*, *19*(4), 3094–3103. https://doi.org/10.1039/c6cp06989d

Jacobsson, T. J., Correa-Baena, J.-P., Halvani Anaraki, E., Philippe, B., Stranks, S. D., Bouduban, M. E. F., … Hagfeldt, A. (2016). Unreacted PbI2 as a Double-Edged Sword for Enhancing the Performance of Perovskite Solar Cells. *Journal of the American Chemical Society*, *138*(32), 10331–10343. https://doi.org/10.1021/jacs.6b06320

Jeon, N. J., Noh, J. H., Kim, Y. C., Yang, W. S., Ryu, S., & Seok, S. Il. (2014). Solvent engineering for high-performance inorganic-organic hybrid perovskite solar cells. *Nature Materials*, *13*(9), 897–903. https://doi.org/10.1038/nmat4014

Jesper Jacobsson, T., Correa-Baena, J.-P., Pazoki, M., Saliba, M., Schenk, K., Grätzel, M., & Hagfeldt, A. (2016). Exploration of the compositional space for mixed lead halogen perovskites for high efficiency solar cells. *Energy Environ. Sci.*, *9*(5), 1706–1724. https://doi.org/10.1039/C6EE00030D

Jiang, C., Lim, S. L., Goh, W. P., Wei, F. X., & Zhang, J. (2015). Improvement of CH3NH3PbI3 Formation for Efficient and Better Reproducible Mesoscopic Perovskite Solar Cells. *ACS Applied Materials and Interfaces*, *7*(44), 24726–24732. https://doi.org/10.1021/acsami.5b07446

Jiang, Q., Zhang, L., Wang, H., Yang, X., Meng, J., Liu, H., … You, J. (2016). Enhanced electron extraction using SnO2 for high-efficiency planar-structure HC(NH2)2PbI3-based perovskite solar cells. *Nature Energy*, *2*(1), 16177. https://doi.org/10.1038/nenergy.2016.177

Jošt, M., Bertram, T., Koushik, D., Marquez, J. A., Verheijen, M. A., Heinemann, M. D., … Albrecht, S. (2019). Highly efficient monolithic perovskite/CIGSe tandem solar cells on rough bottom cell surfaces. In *2019 IEEE 46th Photovoltaic Specialists Conference (PVSC)* (pp. 738–742). https://doi.org/10.1109/PVSC40753.2019.8980493

Ju, Y., Li, L., Wu, Z., & Jiang, Y. (2011). Effect of oxygen partial pressure on the optical property of amorphous titanium oxide thin films. In *Energy Procedia* (Vol. 12, pp. 450–455). Elsevier Ltd. https://doi.org/10.1016/j.egypro.2011.10.060

Juarez-Perez, E. J., Sanchez, R. S., Badia, L., Garcia-Belmonte, G., Kang, Y. S., Mora-Sero, I., & Bisquert, J. (2014). Photoinduced Giant Dielectric Constant in Lead Halide Perovskite Solar Cells. *The Journal of Physical Chemistry Letters*, *5*(13), 2390–2394. https://doi.org/10.1021/jz5011169

Kaniyoor, A., & Ramaprabhu, S. (2012). A Raman spectroscopic investigation of graphite oxide derived graphene. *AIP Advances*, *2*(3), 032183. https://doi.org/10.1063/1.4756995

Kara, K., Kara, D. A., Kirbiyik, C., Ersoz, M., Usluer, O., Briseno, A. L., & Kus, M. (2016). Solvent washing with toluene enhances efficiency and increases reproducibility in perovskite solar cells. *RSC Advances*, *6*(32), 26606–26611. https://doi.org/10.1039/c5ra27122c

Kato, Y., Ono, L. K., Lee, M. V., Wang, S., Raga, S. R., & Qi, Y. (2015). Silver Iodide Formation in Methyl Ammonium Lead Iodide Perovskite Solar Cells with Silver Top Electrodes. *Advanced Materials Interfaces*, *2*(13), 1500195. https://doi.org/10.1002/admi.201500195

Kim, H.-S., Jang, I.-H., Ahn, N., Choi, M., Guerrero, A., Bisquert, J., & Park, N.-G. (2015). Control of *I – V* Hysteresis in $CH_3NH_3PbI_3$ Perovskite Solar Cell. *The Journal of Physical Chemistry Letters*, *6*(22), 4633–4639. https://doi.org/10.1021/acs.jpclett.5b02273

Kim, H. S., & Park, N. G. (2014). Parameters affecting I-V hysteresis of CH3NH3PbI3 Perovskite solar cells: Effects of perovskite crystal size and mesoporous TiO2 layer. *Journal of Physical Chemistry Letters*, *5*(17), 2927–2934. https://doi.org/10.1021/jz501392m

Kim, M., Motti, S. G., Sorrentino, R., & Petrozza, A. (2018). Enhanced solar cell stability by hygroscopic polymer passivation of metal halide perovskite thin film. *Energy and Environmental Science*, *11*(9), 2609–2619. https://doi.org/10.1039/c8ee01101j

Klotz, D., Tumen-Ulzii, G., Qin, C., Matsushima, T., & Adachi, C. (2019). Detecting and identifying reversible changes in perovskite solar cells by electrochemical impedance spectroscopy. *RSC Advances*, *9*(57), 33436–33445. https://doi.org/10.1039/c9ra07048f

Kojima, A., Teshima, K., Shirai, Y., & Miyasaka, T. (2009). Organometal Halide Perovskites as Visible- Light Sensitizers for Photovoltaic Cells. *J Am Chem Soc*, *131*(October), 6050–6051. https://doi.org/10.1021/ja809598r

Kuppusamy, R., Yasir, M., Yee, E., Willcox, M., Black, D. S. C., & Kumar, N. (2018). Guanidine functionalized anthranilamides as effective antibacterials with biofilm disruption activity. *Organic and Biomolecular Chemistry*, *16*(32), 5871–5888. https://doi.org/10.1039/c8ob01699b

Lee, D. G., Kim, M., Kim, B. J., Kim, D. H., Lee, S. M., Choi, M., … Jung, H. S. (2017). Effect of TiO 2 particle size and layer thickness on mesoscopic perovskite solar cells. *Applied Surface Science*, *477*, 131–136. https://doi.org/10.1016/j.apsusc.2017.11.124

Lee, J.-W., Kim, D.-H., Kim, H.-S., Seo, S.-W., Cho, S. M., & Park, N.-G. (2015). Formamidinium and Cesium Hybridization for Photo- and Moisture-Stable Perovskite Solar Cell. *Advanced Energy Materials*, *5*(20), 1501310. https://doi.org/10.1002/aenm.201501310

Lee, J. W., & Park, N. G. (2015). Two-step deposition method for high-efficiency perovskite solar cells. *MRS Bulletin*, *40*(8), 654–659. https://doi.org/10.1557/mrs.2015.166

Lee, M. M., Teuscher, J., Miyasaka, T., Murakami, T. N., & Snaith, H. J. (2012). Efficient hybrid solar cells based on meso-superstructured organometal halide perovskites. *Science (New York, N.Y.)*, *338*(6107), 643–647. https://doi.org/10.1126/science.1228604

Lee, S. H., Yamasue, E., Ishihara, K. N., & Okumura, H. (2010). Photocatalysis and surface doping states of N-doped TiOx films prepared by reactive sputtering with dry air. *Applied Catalysis B: Environmental*, *93*(3–4), 217–226. https://doi.org/10.1016/j.apcatb.2009.09.032

Lee, W. H., Chen, C. Y., Li, C. S., Hsiao, S. Y., Tsai, W. L., Huang, M. J., … Lin, H. W. (2017). Boosting thin-film perovskite solar cell efficiency through vacuum-deposited sub-nanometer small-molecule electron interfacial layers. *Nano Energy*, *38*, 66–71. https://doi.org/10.1016/j.nanoen.2017.05.049

Leijtens, T., Lauber, B., Eperon, G. E., Stranks, S. D., & Snaith, H. J. (2014). The importance of perovskite pore filling in organometal mixed halide sensitized TiO2-based solar cells. *Journal of Physical Chemistry Letters*, *5*(7), 1096–1102. https://doi.org/10.1021/jz500209g

Li, N., Cheng, C., Wei, H., Liu, H., Li, X., Li, W., & Wang, L. (2017). Enhanced efficiency and stability of inverted perovskite solar cells by interfacial engineering with alkyl bisphosphonic molecules. *RSC Advances*, *7*(67), 42105–42112. https://doi.org/10.1039/c7ra07514f

Li, P., Gao, Y., Sun, Z., Chang, D., Gao, G., & Dong, A. (2017). Synthesis, characterization, and bactericidal evaluation of chitosan/guanidine functionalized graphene oxide composites. *Molecules*, *22*(1). https://doi.org/10.3390/molecules22010012

Liang Lim, E., Chin Yap, C., Hafizuddin Hj Jumali, M., Asri Mat Teridi, M., & Hoong Teh, C. (2015). A Mini Review: Can Graphene Be a Novel Material for Perovskite Solar Cell Applications? https://doi.org/10.1007/s40820-017-0182-0

Listorti, A., Juarez-Perez, E. J., Frontera, C., Roiati, V., Garcia-Andrade, L., Colella, S., … Mora-Sero, I. (2015). Effect of mesostructured layer upon crystalline properties and device performance on perovskite solar cells. *Journal of Physical Chemistry Letters*, *6*(9), 1628–1637. https://doi.org/10.1021/acs.jpclett.5b00483

Liu, Z., Sofia, S. E., Laine, H. S., Woodhouse, M., Wieghold, S., Peters, I. M., & Buonassisi, T. (2020). Revisiting thin silicon for photovoltaics: A technoeconomic perspective. *Energy and Environmental Science*, *13*(1), 12–23. https://doi.org/10.1039/c9ee02452b

Lu, J., Lin, X., Jiao, X., Gengenbach, T., Scully, A. D., Jiang, L., … Cheng, Y. B. (2018). Interfacial benzenethiol modification facilitates charge transfer and improves stability of cm-sized metal halide perovskite solar cells with up to 20% efficiency. *Energy and Environmental Science*, *11*(7), 1880–1889. https://doi.org/10.1039/c8ee00754c

Mahmood, K., Sarwar, S., & Mehran, M. T. (2017). Current status of electron transport layers in perovskite solar cells: materials and properties. *RSC Adv.*, *7*(28), 17044–17062. https://doi.org/10.1039/C7RA00002B

Mahmud, M. A., Elumalai, N. K., Upama, M. B., Wang, D., Chan, K. H., Wright, M., … Uddin, A. (2017). Low temperature processed ZnO thin film as electron transport layer for efficient perovskite solar cells. *SOLAR ENERGY MATERIALS AND SOLAR CELLS*, *159*, 251–264. https://doi.org/10.1016/j.solmat.2016.09.014

Meng, F., Liu, A., Gao, L., Cao, J., Yan, Y., Wang, N., … Ma, T. (2019). Current progress in interfacial engineering of carbon-based perovskite solar cells. *JOURNAL OF MATERIALS CHEMISTRY A*, *7*(15), 8690–8699. https://doi.org/10.1039/c9ta01364d

Miyano, K., Tripathi, N., Yanagida, M., & Shirai, Y. (2016). Lead Halide Perovskite Photovoltaic as a Model p – i – n Diode. *Accounts of Chemical Research*, *49*(2), 303–310. https://doi.org/10.1021/acs.accounts.5b00436

Morton, O. (2007). *Eating the sun : how plants power the planet*. Fourth Estate.

Nelson, J. (2003). *The Physics of Solar Cells*. Imperial College Press, World Scientific Publishing Co. https://doi.org/10.1142/p276

Niu, G., Guo, X., & Wang, L. (2015). Review of recent progress in chemical stability of perovskite solar cells. *Journal of Materials Chemistry A*, *3*(17), 8970–8980. https://doi.org/10.1039/c4ta04994b

Noh, J. H., Im, S. H., Heo, J. H., Mandal, T. N., & Seok, S. Il. (2013). Chemical Management for Colorful, Efficient, and Stable Inorganic–Organic Hybrid Nanostructured Solar Cells. *Nano Letters*, *13*(4), 1764–1769. https://doi.org/10.1021/nl400349b

NREL. (2020). Efficiency Chart. Retrieved from https://www.nrel.gov/pv/assets/pdfs/best-research-cell-efficiencies.20191104.pdf

Olyaeefar, B., Ahmadi-Kandjani, S., & Asgari, A. (2017). Bulk and interface recombination in planar lead halide perovskite solar cells: A Drift-Diffusion study. *Physica E: Low-Dimensional Systems and Nanostructures*, *94*, 118–122. https://doi.org/10.1016/j.physe.2017.07.018

Park, N.-G., Grätzel, M., & Miyasaka, T. (Eds.). (2016). *Organic-Inorganic Halide Perovskite Photovoltaics*. *Springer*. Switzerland: Springer. https://doi.org/10.1007/978-3-319-35114-8_4

Patel, J. B., Milot, R. L., Wright, A. D., Herz, L. M., & Johnston, M. B. (2016). Formation Dynamics of CH3NH3PbI3 Perovskite Following Two-Step Layer Deposition. *Journal of Physical Chemistry Letters*, *7*(1), 96–102. https://doi.org/10.1021/acs.jpclett.5b02495

Pathak, S., Sepe, A., Sadhanala, A., Deschler, F., Haghighirad, A., Sakai, N., … Snaith, H. J. (2015). Atmospheric influence upon crystallization and electronic disorder and its impact on the photophysical properties of organic-inorganic perovskite solar cells. *ACS Nano*, *9*(3), 2311–2320. https://doi.org/10.1021/nn506465n

Péan, E. V., De Castro, C. S., & Davies, M. L. (2019). Shining a light on the photoluminescence behaviour of methylammonium lead iodide perovskite: investigating the competing photobrightening and photodarkening processes. *Materials Letters*, *243*, 191–194. https://doi.org/10.1016/j.matlet.2019.01.103

Perkowitz, S. (1993). *Optical Characterization of Semiconductors*. *Optical Characterization of Semiconductors*. Elsevier. https://doi.org/10.1016/c2009-0-21312-2

Perrier, G., De Bettignies, R., Berson, S., Lemaître, N., & Guillerez, S. (2012). Impedance spectrometry of optimized standard and inverted P3HT-PCBM organic solar cells. *Solar Energy Materials and Solar Cells*, *101*, 210–216. https://doi.org/10.1016/j.solmat.2012.01.013

Philipps, S., & Warmuth, W. (2019). ©Fraunhofer ISE: Photovoltaics Report, updated: 14 November 2019, (November), 1–49.

Pitarch-Tena, D., Ngo, T. T., Vallés-Pelarda, M., Pauporté, T., & Mora-Seró, I. Impedance Spectroscopy Measurements in Perovskite Solar Cells: Device Stability and Noise Reduction, 3 ACS Energy Letters § (2018). American Chemical Society. https://doi.org/10.1021/acsenergylett.8b00465

Pockett, A., Eperon, G. E., Peltola, T., Snaith, H. J., Walker, A., Peter, L. M., & Cameron, P. J. (2015). Characterization of Planar Lead Halide Perovskite Solar Cells by Impedance Spectroscopy, Open-Circuit Photovoltage Decay, and Intensity-Modulated Photovoltage/Photocurrent Spectroscopy. *J. Phys. Chem. C*, *7*(119), 3456–3465. https://doi.org/10.1021/jp510837q

Pockett, A., Eperon, G. E., Sakai, N., Snaith, H. J., Peter, L. M., & Cameron, P. J. (2017). Microseconds, milliseconds and seconds: deconvoluting the dynamic behaviour of planar perovskite solar cells †. *Phys. Chem. Chem. Phys*, *19*(8), 5959–5970.

Qarony, W., Jui, Y. A., Das, G. M., Mohsin, T., Hossain, M. I., & Islam, S. N. (2015). Optical Analysis in CH3NH3PbI3 and CH3NH3PbI2Cl Based Thin-Film Perovskite Solar Cell. *American Journal of Energy Research*, *3*(2), 19–24. https://doi.org/10.12691/ajer-3-2-1

Qiu, W., Bastos, J. P., Dasgupta, S., Merckx, T., Cardinaletti, I., Jenart, M. V. C., … Cheyns, D. (2017). Highly efficient perovskite solar cells with crosslinked PCBM interlayers. *Journal of Materials Chemistry A*, *5*(6), 2466–2472. https://doi.org/10.1039/C6TA08799J

Ramirez-Rincon, J. A., Castro-Chong, A. M., Forero-Sandoval, I. Y., Gomez-Heredia, C. L., Peralta-Dominguez, D., Fernandez-Olaya, M. G., … Alvarado-Gil, J. J. (2020). Determination of the nonradiative conversion efficiency of lead mixed-halide perovskites using optical and photothermal spectroscopy. *Applied Optics*, *59*(13), D201. https://doi.org/10.1364/ao.384726

Rizzo, A., Lamberti, F., Buonomo, M., Wrachien, N., Torto, L., Lago, N., … Cester, A. (2019). Understanding lead iodide perovskite hysteresis and degradation causes by extensive electrical characterization. *Solar Energy Materials and Solar Cells*. https://doi.org/10.1016/j.solmat.2018.09.021

Sacco, A. (2017). Electrochemical impedance spectroscopy: Fundamentals and application in dye-sensitized solar cells. *Renewable and Sustainable Energy Reviews*, *79*(August 2016), 814–829. https://doi.org/10.1016/j.rser.2017.05.159

Saliba, M., Matsui, T., Seo, J. Y., Domanski, K., Correa-Baena, J. P., Nazeeruddin, M. K., … Grätzel, M. (2016). Cesium-containing triple cation perovskite solar cells: Improved stability, reproducibility and high efficiency. *Energy and Environmental Science*, *9*(6), 1989–1997. https://doi.org/10.1039/c5ee03874j

Salim, T., Sun, S., Abe, Y., Krishna, A., Grimsdale, A. C., & Lam, Y. M. (2015). Perovskite-based solar cells: impact of morphology and device architecture on device performance. *J. Mater. Chem. A*, *3*(17), 8943–8969. https://doi.org/10.1039/C4TA05226A

Schulze, P. S. C., Bett, A. J., Winkler, K., Hinsch, A., Lee, S., Mastroianni, S., … Goldschmidt, J. C. (2017). Novel Low-Temperature Process for Perovskite Solar Cells with a Mesoporous TiO2Scaffold. *ACS Applied Materials and Interfaces*, *9*(36), 30567–30574. https://doi.org/10.1021/acsami.7b05718

Shao, Y., Xiao, Z., Bi, C., Yuan, Y., & Huang, J. (2014). Origin and elimination of photocurrent hysteresis by fullerene passivation in CH 3 NH 3 PbI 3 planar heterojunction solar cells. https://doi.org/10.1038/ncomms6784

Sheikh, A. D., Bera, A., Haque, M. A., Rakhi, R. B., Del Gobbo, S., Alshareef, H. N., & Wu, T. (2015). Atmospheric effects on the photovoltaic performance of hybrid perovskite solar cells. *Solar Energy Materials and Solar Cells*, *137*, 6–14. https://doi.org/10.1016/j.solmat.2015.01.023

Shlenskaya, N. N., Belich, N. A., Grätzel, M., Goodilin, E. A., & Tarasov, A. B. (2018). Light-induced reactivity of gold and hybrid perovskite as a new possible degradation

mechanism in perovskite solar cells. *Journal of Materials Chemistry A*, *6*(4), 1780–1786. https://doi.org/10.1039/C7TA10217H

Sierra-Castillo, A., Saucedo-Orozco, I., Bittencourt, C., Arcon, D., Cuentas-Gallegos, A. K., Calderon, H. A., & Quintana, M. (2018). Carbon based nanohybrid materials (sp2-sp3) for energy applications. *Microscopy and Microanalysis*, *24*(S1), 134–135. https://doi.org/10.1017/S1431927618001162

Smith, I. C., Hoke, E. T., Solis-Ibarra, D., McGehee, M. D., & Karunadasa, H. I. (2014). A Layered Hybrid Perovskite Solar-Cell Absorber with Enhanced Moisture Stability. *Angewandte Chemie International Edition*, *53*(42), 11232–11235. https://doi.org/10.1002/anie.201406466

Song, J., Zheng, E., Wang, X.-F., Tian, W., & Miyasaka, T. (2016). Low-temperature-processed ZnO-SnO2 nanocomposite for efficient planar perovskite solar cells. *SOLAR ENERGY MATERIALS AND SOLAR CELLS*, *144*, 623–630. https://doi.org/10.1016/j.solmat.2015.09.054

Stewart, R. J., Grieco, C., Larsen, A. V., Doucette, G. S., & Asbury, J. B. (2016). Molecular Origins of Defects in Organohalide Perovskites and Their Influence on Charge Carrier Dynamics. *Journal of Physical Chemistry C*, *120*(23), 12392–12402. https://doi.org/10.1021/acs.jpcc.6b03472

Suess, H. E., & Urey, H. C. (1956). Abundances of the elements. *Reviews of Modern Physics*, *28*(1), 53–74. https://doi.org/10.1103/RevModPhys.28.53

Tapia, J. I., Larios, E., Bittencourt, C., Yacamán, M. J., & Quintana, M. (2016). Carbon nano-allotropes produced by ultrasonication of few-layer graphene and fullerene. *Carbon*, *99*, 541–546. https://doi.org/10.1016/j.carbon.2015.12.071

Tress, W., Marinova, N., Moehl, T., Zakeeruddin, S. M., Nazeeruddin, M. K., & Grätzel, M. (2015). Understanding the rate-dependent J–V hysteresis, slow time component, and aging in $CH_3NH_3PbI_3$ perovskite solar cells: the role of a compensated electric field. *Energy & Environmental Science*, *8*(3), 995–1004. https://doi.org/10.1039/C4EE03664F

Tress, Wolfgang, Yavari, M., Domanski, K., Yadav, P., Niesen, B., Baena, J. P. C., … Graetzel, M. (2018). Interpretation and evolution of open-circuit voltage, recombination, ideality factor and subgap defect states during reversible light-soaking and irreversible degradation of perovskite solar cells. *Energy & Environmental Science*, *11*, 151–165. https://doi.org/10.1039/C7EE02415K

Ul-Hamid, A. (2018). *A Beginners' Guide to Scanning Electron Microscopy*. *A Beginners' Guide to Scanning Electron Microscopy*. Springer International Publishing. https://doi.org/10.1007/978-3-319-98482-7

Valadez-Villalobos, K., Idígoras, J., Delgado, L. P., Meneses-Rodríguez, D., Anta, J. A., & Oskam, G. (2019). Correlation between the effectiveness of the electron-selective contact and photovoltaic performance of perovskite solar cells. *Journal of Physical Chemistry Letters*, *10*(4), 877–882. https://doi.org/10.1021/acs.jpclett.8b03834

van de Lagemaat, J., Park, N.-G., & Frank, A. J. (2000). Influence of Electrical Potential Distribution, Charge Transport, and Recombination on the Photopotential and Photocurrent Conversion Efficiency of Dye-Sensitized Nanocrystalline TiO_2 Solar Cells: A Study by Electrical Impedance and Optical Modulation Techniques. *The Journal of Physical Chemistry B*, *104*(9), 2044–2052. https://doi.org/10.1021/jp993172v

Walsh, A. (2015). Principles of Chemical Bonding and Band Gap Engineering in Hybrid Organic–Inorganic Halide Perovskites. *The Journal of Physical Chemistry C*, *119*(11), 5755–5760. https://doi.org/10.1021/jp512420b

Wang, C., Zhang, C., Huang, Y., Tong, S., Wu, H., Zhang, J., … Yang, J. (2017). Degradation behavior of planar heterojunction CH3NH3PbI3 perovskite solar cells. *Synthetic Metals*, *227*, 43–51. https://doi.org/10.1016/j.synthmet.2017.02.022

Wang, D. H., Kim, J. K., Seo, J. H., Park, I., Hong, B. H., Park, J. H., & Heeger, A. J. (2013). Transferable Graphene Oxide by Stamping Nanotechnology: Electron-Transport Layer for Efficient Bulk-Heterojunction Solar Cells. *Angewandte Chemie International Edition*, *52*(10), 2874–2880. https://doi.org/10.1002/anie.201209999

Wang, D., Wright, M., Elumalai, N. K., & Uddin, A. (2016). Stability of perovskite solar cells. *Sol. Energy Mater. Sol. Cells*, *147*, 255–275. https://doi.org/10.1016/j.solmat.2015.12.025

Wang, M., Zang, Z., Yang, B., Hu, X., Sun, K., & Sun, L. (2018). Performance improvement of perovskite solar cells through enhanced hole extraction: The role of iodide concentration gradient. *Solar Energy Materials and Solar Cells*, *185*, 117–123. https://doi.org/10.1016/j.solmat.2018.05.025

Wang, Q., Moser, J.-E., & Grätzel, M. (2005). Electrochemical Impedance Spectroscopic Analysis of Dye-Sensitized Solar Cells. *The Journal of Physical Chemistry B*, *109*(31), 14945–14953. https://doi.org/10.1021/jp052768h

Wang, R., Mujahid, M., Duan, Y., Wang, Z., Xue, J., & Yang, Y. (2019). A Review of Perovskites Solar Cell Stability. *Advanced Functional Materials*, *29*(47), 1808843. https://doi.org/10.1002/adfm.201808843

Waseda, Y., Matsubara, E., Shinoda, K., Waseda, Y., Matsubara, E., & Shinoda, K. (2011). Fundamental Properties of X-rays. In *X-Ray Diffraction Crystallography* (pp. 1–20). Springer Berlin Heidelberg. https://doi.org/10.1007/978-3-642-16635-8_1

Wojciechowski, K., Saliba, M., Leijtens, T., Abate, A., & Snaith, H. J. (2014). Sub-150 °C processed meso-superstructured perovskite solar cells with enhanced efficiency. *Energy Environ. Sci.*, *7*(3), 1142–1147. https://doi.org/10.1039/C3EE43707H

Würfel, P. (2005). *Physics of solar cells : from principles to new concepts*. Wiley-VCH.

Yang, J., Fransishyn, K. M., & Kelly, T. L. (2016). Comparing the Effect of Mesoporous and Planar Metal Oxides on the Stability of Methylammonium Lead Iodide Thin Films. *Chemistry of Materials*, *28*(20), 7344–7352. https://doi.org/10.1021/acs.chemmater.6b02744

Yang, W. S., Noh, J. H., Jeon, N. J., Kim, Y. C., Ryu, S., Seo, J., & Seok, S. Il. (2015). High-performance photovoltaic perovskite layers fabricated through intramolecular exchange. *Science (New York, N.Y.)*, *348*(6240), 1234–1237. https://doi.org/10.1126/science.aaa9272

Yang, W. S., Park, B., Jung, E. H., & Jeon, N. J. (2017). Iodide management in formamidinium-lead-halide – based perovskite layers for efficient solar cells. *Science (New York, N.Y.)*, *356*(6345), 1376–1379. https://doi.org/10.1126/science.aan2301

Ye, T., Lim, S. L., Li, X., Petrović, M., Wang, X., Jiang, C., … Ramakrishna, S. (2018). Pinhole-free mixed perovskite film for bending durable mixed perovskite solar cells. *Solar Energy Materials and Solar Cells*, *175*, 111–117. https://doi.org/10.1016/j.solmat.2017.10.031

Yin, W. J., Yang, J. H., Kang, J., Yan, Y., & Wei, S. H. (2015). Halide perovskite materials for solar cells: A theoretical review. *Journal of Materials Chemistry A*, *3*(17), 8926–8942. https://doi.org/10.1039/c4ta05033a

You, J., Hong, Z., Yang, Y. Y. M., Chen, Q., Cai, M., Song, T.-B., … Zhou, H. (2014). Low-temperature solution-processed perovskite solar cells with high efficiency and flexibility. *ACS Nano*, *8*(2), 1674–1680. https://doi.org/10.1021/nn406020d

Yu, H., Lu, H., Xie, F., Zhou, S., & Zhao, N. (2016). Native Defect-Induced Hysteresis Behavior in Organolead Iodide Perovskite Solar Cells. *Advanced Functional Materials*, *26*(9), 1411–1419. https://doi.org/10.1002/adfm.201504997

Zarazua, I., Bisquert, J., & Garcia-Belmonte, G. (2016). Light-Induced Space-Charge Accumulation Zone as Photovoltaic Mechanism in Perovskite Solar Cells. *The Journal of Physical Chemistry Letters*, *7*(3), 525–528. https://doi.org/10.1021/acs.jpclett.5b02810

Zarazua, I., Han, G., Boix, P. P., Mhaisalkar, S., Fabregat-Santiago, F., Mora-Seró, I., … Garcia-Belmonte, G. (2016). Surface Recombination and Collection Efficiency in Perovskite Solar Cells from Impedance Analysis. *The Journal of Physical Chemistry Letters*, *7*(24), 5105–5113. https://doi.org/10.1021/acs.jpclett.6b02193

Zardetto, V., De Angelis, G., Vesce, L., Caratto, V., Mazzuca, C., Gasiorowski, J., … Brown, T. M. (2013). Formulations and processing of nanocrystalline TiO2films for the different requirements of plastic, metal and glass dye solar cell applications. *Nanotechnology*, *24*(25). https://doi.org/10.1088/0957-4484/24/25/255401

Zhou, Y., Vasiliev, A. L., Wu, W., Yang, M., Pang, S., Zhu, K., & Padture, N. P. (2015). Crystal morphologies of organolead trihalide in mesoscopic/planar perovskite solar cells. *Journal of Physical Chemistry Letters*, *6*(12), 2292–2297. https://doi.org/10.1021/acs.jpclett.5b00981

Zohar, A., Kedem, N., Levine, I., Zohar, D., Vilan, A., Ehre, D., … Cahen, D. (2016). Impedance Spectroscopic Indication for Solid State Electrochemical Reaction in (CH 3 NH 3)PbI 3 Films. *J. Phys. Chem. Lett*, *7*(1), 191–197. https://doi.org/10.1021/acs.jpclett.5b02618